Conventional and Alternative Jet Fuels for Diesel Combustion: Surrogate Development and Insights into the Effect of Fuel Properties on Ignition

by

Doohyun Kim

A dissertation submitted in partial fulfillment
of the requirements for the degree of
Doctor of Philosophy
(Mechanical Engineering)
in the University of Michigan
2016

Doctoral Committee:

Professor Angela Violi, Co-Chair
Assistant Research Scientist Jason B. Martz, Co-Chair
Professor Dennis Assanis, Stony Brook University
Assistant Professor Mirko Gamba
Peter J. Schihl, US Army RDECOM-TARDEC

Acknowledgments

First, I would like to thank Professor Angela Violi for guiding me throughout the doctoral program. She has been a great research mentor, giving me tremendous amount of encouragement and motivation for the work I have been doing. I would also like to thank Dr. Jason Martz for his support, guidance, and friendship. We had discussions over the research on a daily basis and without his encouragements and challenging comments, I would not have completed my doctoral degree.

I would like to thank Provost Dennis Assanis for giving me the opportunity to conduct research in his group and for supporting me during my master's and doctoral program before he moved to Stony Brook University. His leadership and enthusiasm have been invaluable for my graduate studies. I am also grateful to Professor Mirko Gamba for serving as a committee member. I would like to thank Dr. Pete Schihl for supporting this interesting project and providing feedbacks and outside perspective.

During my graduate studies in Walter E. Lay Automotive Laboratories since Fall 2008, I met so many great people. I am deeply grateful to everyone. I would like to thank John Hoard for his support and guidance throughout my master's program. I would also like to thank Kyoung Hyun Kwak for being such a great friend. I would like to thank friends in AL2032, Rob, Laura, and Prasad and all the fellow students and post docs in

Prof. Stefanopoulou's group and Prof. Boehman's group who I worked with. I wish to thank Autolab staffs, William, Kathie, and Melissa. I would also like to thank all the friends I met from the Korean graduate basketball team, who made my days in Ann Arbor really enjoyable.

I would like to thank my parents, Dong Jin Kim and Jung Soo Kim, and my sister Sohyun. Every time I doubt myself, they believed in me and made me move forward. Their endless love and support mean everything to me. I'd also like to thank all my family back in Korea, in particular, my grandmother. I wish to thank my wife's family in Chicago and Ann Arbor for their love and support. Finally, I truly thank my wife Julie. She has been my best friend and soulmate since we first met 19 years ago. She has endured tough times with me and sacrificed so much. She also has been the best mother to our wonderful children, Andrew Eunjun and Joseph Eunho.

Funding for this work was provided by the Automotive Research Center (ARC), A U.S. Army Center of Excellence in the modeling and simulation of ground vehicles at the University of Michigan, with funding from government contract DoD-DoA W56HZV-04-2-0001 through the U.S. Army Tank Automotive Research, Development, and Engineering Center.

Table of Contents

List of Figures

List of Tables

Abstract

The use of kerosene-based jet fuels for all military applications has been mandated by U.S. military's single fuel forward concept. Recently, interest in non-petroleum-derived alternative jet fuels has also been increasing as a way to diversify the source of jet fuels. However, wide variations in physical and chemical properties within various types of jet fuels have shown significant impact on the operation of diesel engine. Surrogate fuels are needed for CFD simulations with detailed kinetic modeling to represent the combustion behavior of the real fuels, which are very complex mixtures. However, currently existing jet fuel surrogates for CFD simulation are not developed to capture the liquid fuel physical properties that influence the spray characteristics and ignition delay times during the diesel combustion process. This work address the need for comprehensive jet fuel surrogates that successfully emulate physical and chemical properties of conventional and alternative jet fuels. The developed surrogate fuels are then utilized within CFD simulation to obtain insights on how the fuel properties affect the fundamental processes of diesel ignition.

For the optimization-based surrogate formulation methodology, it is essential to identify the target properties for the surrogate fuel to match. In the first part of the dissertation, a sensitivity analysis was conducted with CFD simulations of pure n-

dodecane spray in a constant volume chamber to identify temperature dependent liquid physical properties that are of significance to the diesel ignition process. Out of six physical properties that were tested, density, viscosity, volatility, and specific heat showed major impact on liquid penetration length and ignition delay time.

In order to formulate surrogate mixtures that emulate multiple target properties including those found through the sensitivity analysis, a surrogate optimizer was developed. The optimizer uses models and correlations to estimate mixture properties and finds the mixture composition that best matches the properties of the targeted fuels. Using a six component surrogate palette (n-dodecane, n-decane, iso-cetane, iso-octane, decalin, and toluene), the surrogate optimizer generated surrogate mixtures for Jet-A POSF-4658, a petroleum-derived conventional jet fuel, IPK POSF-5642, a coal-derived synthetic jet fuel, and S-8 POSF-4734, a natural-gas-derived synthetic jet fuel. Kinetic modeling of the developed surrogate fuels were enabled by a detailed chemical mechanism. Utilizing the developed surrogates and the kinetic mechanism, a numerical experiment was conducted with CFD simulations to evaluate the relative importance of physical and chemical properties to the ignition process of the fuel spray for two fuels, Jet-A and S-8. This study indicates that the fuel's chemical properties are much more important to the duration of the ignition delay period than the physical properties, which emphasizes the chemical aspect of the diesel ignition phenomena.

Chapter 1

Introduction

1.1 Jet Fuel in Diesel Engine

The U.S. military's single fuel forward concept [1] mandates the use of kerosene-based jet fuels for battlefield deployed aircraft and ground vehicles for the simplification of supply chain logistics. As a result, military diesel engines must be capable of operating with jet fuels. Of these fuels, the primary military jet fuel is JP-8, which meets the fuel specifications identical to a civilian aviation fuel Jet A-1 with a military-specific additive package [2]. Gas turbines and jet engines are the main consumers of JP-8, and combustion within these devices is only marginally affected by the auto-ignition characteristics of fuel, which is measured by the Cetane Number (CN) for diesel applications. The resulting lack of a JP-8 CN specification can result in CN ranging from 36 ~ 50 for petroleum-derived JP-8's [3].

Recently, interest in alternative or synthetic jet fuels has been increasing in the military and civilian sectors as a way to diversify the source of jet fuels to resolve energy security issues. A number of different Synthetic Paraffinic Kerosenes (SPKs), produced through the Fischer-Tropsch process or by vegetable oil hydroprocessing have been

tested as alternative jet fuels [4]. While SPKs are produced to have molecular size distributions similar to petroleum-derived jet fuels, significant property discrepancies exist between the fuels which may negatively affect diesel engine operation. SPKs are predominantly paraffinic in nature, which leads to significantly lower liquid density for SPKs compared to petroleum-derived jet fuels. In turn, these liquid fuel density variations can influence injection related parameters, such as injection velocity, which can impact the rate of fuel air mixing and the diesel ignition process [5]. Also, marginal to non-existent aromatic content of SPKs is reported to cause leaks in fuel system, as some elastomers used for sealing shrink when wetted with non-aromatic fuels [6]. Another significant problem is the extreme variation in ignition quality observed for the different SPKs. In particular, the CN of SPKs under consideration by the U.S. military can range from 15 to 59 [7], which is far greater variation compared to petroleum-derived jet fuels. Such CN variation impacts diesel engine ignition and combustion phasing, leading to difficulties with cold starting and fuel economy [8]. Due to such a significant difference in density, aromatic content, and the ignition quality, blends of conventional and alternative fuels are currently being used for diesel engines to mitigate those problems [8].

Early engine tests with jet fuels focused on its cumulative effects on performance and emissions, and investigated the overall impact of replacing baseline diesel fuel with jet fuels [9–12]. More recently, the ignition behavior of various types of conventional and alternative jet fuels within diesel engines has been reported in [8,13–19]. While engine experiments enable some global understanding of this behavior through heat release analysis, detailed understanding of how these physical and chemical phenomena of the fuel variation affect the ignition delay cannot be determined from the engine experiments.

Combustion simulations with Computational Fluid Dynamics (CFD) and detailed kinetic modeling can complement metal engine experiments and provide insight into spray and gas phase combustion behaviors.

1.2 Surrogate Fuel Background

Current mainstream transportation fuels, such as jet fuel, diesel, or gasoline, are fractional distillates of crude oil. These real fuels are very complex mixtures of various types of hydrocarbons (linear alkanes, cyclic alkanes, aromatics, etc.) and are composed of hundreds to thousands of hydrocarbon species. Figure 1.1 shows the gas chromatograms of JP-8, diesel fuel, and gasoline fuel [20], where the complex nature of these real fuels is demonstrated by having numerous peaks in a wide range of retention time; the gas chromatogram of a single-component liquid produces only a single peak.

There are a few challenges when it comes to detailed kinetic modeling of these real transportation fuels. First, since these fuels are very complex mixtures, it is nearly impossible to identify all of the hydrocarbon species and their compositions. Also, kinetic data and mechanism are currently limited to only a few hydrocarbon molecules. Moreover, even if all fuel species are identified and their kinetic mechanisms are available, simulations of the combustion process would be prohibitively long when all species are included.

In order to overcome such challenges, surrogate fuels of these real fuels have been developed and utilized to model the diesel combustion processes. The surrogate fuel is formulated with a handful of well-characterized pure components to emulate the combustion behavior of the targeted real fuel. Recent progress in surrogate development

for common transportation fuels is extensively reviewed in [21–26]. One of the surrogate examples is pure n-heptane, which has been used to represent the ignition quality of conventional diesel fuel; other characteristics, such as liquid density, volatility, or aromatic content, are poorly represented with a single component fuel such as n-heptane. More comprehensive surrogate mixtures capable of emulating physical properties and combustion characteristics can be formulated using more surrogate components, but at the same time, the number of surrogate components must be limited, based in part upon a limited number of species available within leading kinetic mechanisms.

Surrogate fuels can be formulated through experimental trial and error to find the model mixture that matches certain properties or combustion behavior of the target fuel. While this methodology has been widely used, it is ineffective in finding the mixture that emulates multiple target properties. More recently, optimization-based formulation methodologies have had success in formulating surrogate mixtures that successfully match multiple combustion-related target fuel properties [27–31]. This approach incorporates mathematical optimization using models and correlations to estimate the model mixture properties to find the surrogate composition that best matches the target fuel properties.

One of the keys to successful surrogate formulation with the optimization-based approach is defining target properties relevant to the targeted device and processes. Since combustion physics and thermodynamic regimes differ from device to device, fuel properties influencing the combustion process are not necessarily the same. For instance, combustion in conventional spark-ignited gasoline engines is entirely in the gas phase and the liquid fuel properties do not have significant effects on the engine’s combustion

characteristics. On the other hand, for a diesel engine with direct fuel injection, the liquid fuel physical properties determine the spray characteristics by influencing the various physical processes within the liquid phase. Thus, it is very important in the surrogate development process to understand which fuel properties have major impact on the combustion physics of the targeted device, and to emulate those properties accordingly.

1.3 Ignition Delay in Diesel Engines

The diesel combustion process used within Direct Injection (DI) Compression Ignition (CI) engines is composed of several phases, including the ignition delay period, the premixed combustion phase, the mixing-controlled combustion or diffusion burning phase, and the late combustion phase, as illustrated in Figure 1.2 [32]. The ignition delay period, which is defined as the time between the start of injection (SOI) and the start of combustion (SOC), is quite important for diesel engine calibration. The onset of combustion in diesel engines is controlled through the fuel injection timing, and the ignition delay period changes drastically depending on the operating conditions and the properties of the fuel. Since optimal combustion phasing is critical for achieving high efficiency, understanding the ignition delay phenomena is essential for the engine control scheme.

It is well known that the ignition delay period is governed by complex fuel dependent physical and chemical phenomena, which prepare the injected fuel for combustion [32,33]. Figure 1.3 conceptually illustrates some of the major physical and chemical phenomena during the ignition delay period of diesel engine. Initially, the liquid fuel is injected and starts to break down, generating small liquid droplets

(breakup/atomization). These liquid droplets are decelerated (drag) and deformed (distortion) by the ambient charge; the droplets also collide and merge (collision/coalescence). At the same time, liquid fuel droplets are heated up by hotter ambient charge and eventually vaporized (evaporation). Air entrained into the fuel jet is mixed with the vaporized fuel to within combustible limits (fuel/air mixing). These are the physical processes required for fuel ignition, which are influenced by temperature dependent liquid physical properties of the fuel, in addition to injection parameters (injection pressure, orifice diameter, etc.) and geometric factors (combustion chamber/piston bowl design, etc.).

As soon as the liquid fuel is vaporized and the gas phase fuel meets oxygen, oxidation chemistry begins to prepare the fuel-air charge for ignition, which is enhanced by the high temperature and pressure within the combustion chamber. Decomposition of the fuel molecules into smaller hydrocarbons and active radicals initiates the spontaneous ignition of the properly mixed air/fuel charge, leading to the premixed combustion phase. These processes are influenced by the fuel's chemical properties such as ignitability (Cetane Number for diesel application), the energy content (Lower Heating Value), and the hydrogen/carbon ratio (local fuel/air stoichiometry).

Thus, the ignition phenomena within diesel engines have both physical and chemical aspects that are affected by the physical and chemical properties of the fuel. This indicates that diesel combustion surrogates must consider the emulation of both the physical and chemical properties of the target fuel.

1.3.1 Cetane Number and Derived Cetane Number

The auto-ignition quality of fuels for use in diesel combustion is often represented by Cetane Number (CN). A high CN indicates a highly reactive fuel, which results in short ignition delay times. Traditionally, CN has been measured by using a variable compression ratio Cooperative Fuel Research (CFR) engine with a standardized operating method (ASTM D613). This method attempts to find the blending ratio of the two reference fuels, n-hexadecane (n-cetane) and 2,2,4,4,6,8,8-heptamethylnonane (iso-cetane), that gives an identical ignition delay time to the sample fuel. The CN is determined based on this blending ratio.

Recently, alternative methods for measuring fuel ignition quality have been developed. A standardized procedure (ASTM D6890) using an Ignition Quality Tester (IQT), which is a bench-top constant volume spray chamber, is one of the most widely used methods. The test fuel is directly injected to a heated, pressurized (818 K, 2.137 MPa) IQT combustion chamber and ignited. Then the measured ignition delay time is converted to CN by a correlation. The Derived Cetane Number (DCN) obtained from this approach has shown good agreement with CN for mid-range CN fuels [34]. Similar constant volume spray chambers are also available, including the Fuel Ignition Tester (FIT) with ASTM D7170 and Cetane Ignition Delay (CID) with ASTM D7668. When compared to the CFR method, these alternative methods require much smaller amounts of sample fuel and much shorter test times. Also, better reproducibility is reported for these methods compared to the CN measured with the CFR method [34].

Throughout this dissertation, DCN refers to the measurement from IQT.

1.4 Review of Previous Jet Fuel Surrogates

One of the earliest studies on developing fuel surrogates for petroleum-derived jet fuels is found in Wood et al. [35], where 14 surrogate components were used to replicate the distillation curve and hydrocarbon class composition of a military jet fuel JP-4. Since then, several surrogate mixtures with mated chemical mechanism were proposed. Guéret et al. [36] proposed a surrogate mixture of n-undecane/n-propylcyclohexane/1,2,4-trimethylbenzene along with a quasi-global kinetic mechanism to capture the combustion behavior of Jet A-1 in Jet-Stirred Reactor (JSR). Patterson et al. [37] studied a mixture of n-decane and toluene with a kinetic mechanism and showed that computation results were in good agreement with experimental premixed flame data and JSR data of kerosene. Dagaut et al. [38] showed that of all the candidate mixtures they tested, a three component mixture of n-decane/n-propylbenzene/n-propylcyclohexane produced the best agreement with the JSR and flame data of Jet-A 1. Violi et al. [39] formulated surrogates targeting the volatility and sooting tendency of JP-8. When Vasu et al. [40] evaluated the ignition delay predictions from some of the existing surrogates, Violi surrogate #3 (n-dodecane/ iso-octane/methylcyclohexane/benzene/toluene) coupled with the Ranzi mechanism [41] gave the closest agreement with their measured ignition delay times from shock tube experiments at temperatures above 1000K. Honnet et al. [42] reported a two component kerosene surrogate (n-decane/1,2,4-trimethylbenzene) and its chemical mechanism, which was formulated to match the critical kerosene extinction conditions and auto-ignition. Dooley et al. [29] formulated a surrogate mixture composed of n-dodecane/iso-octane/1,3,5-trimethylbenzene/n-propylbenzene which reproduced the DCN, hydrogen carbon ratio (H/C), molecular weight (MW), and Threshold Sooting Index (TSI)

of a representative Jet-A POSF-4658, while ignition delay modeling studies of this surrogate were conducted in [43]. This surrogate mixture by Dooley et al. was extensively tested in various combustion devices, including a shock tube, rapid compression machine, counter flow diffusion flame, pre-mixed flame, and wick-fed laminar diffusion flame. Compositions of these previous surrogates are summarized in Table 1.1. More recently, surrogate mixtures for alternative jet fuels (SPKs) were proposed. Surrogates for natural-gas-derived SPKs and their kinetic mechanisms are found in Mzé-Ahmed et al. [44], Naik et al. [31], and Dooley et al. [45]. Additionally, Allen et al. [46] proposed surrogates for SPK produced through the hydroprocessing of vegetable oils.

While all the surrogates mentioned above were targeted to mimic gas phase combustion characteristics and agreed reasonably well with experimental data, little or no consideration were given to temperature dependent physical properties of the liquid fuel. Huber and coworkers formulated surrogates for petroleum-derived Jet-A POSF-4658 [30], natural-gas-derived [47] and coal-derived SPKs [48] considering various temperature-dependent physical properties. However, since these surrogates were not intended for use in combustion modeling studies, most of the molecules used in these surrogates lack chemical mechanisms, making their use in reacting CFD problematic. Hence there is a need for jet fuel surrogates for CFD applications that are capable of capturing both physical and chemical properties of jet fuels.

In addition, existing jet fuel surrogates have been developed to represent a certain type of jet fuel. Noting that a wide range of jet fuels are expected to be used in the future and their properties vary significantly, developing a new surrogate formulation

methodology using a common surrogate palette that is capable of emulating properties of various types jet fuels is necessary. By having a common palette, one chemical mechanism can be shared amongst any surrogates formulated using the species in the palette.

1.5 Objectives and Document Organization

The first objective of this thesis is to develop a surrogate formulation methodology using a common palette that is able to emulate both physical and chemical properties of various conventional and alternative jet fuels. Then, using the developed surrogates, the complex diesel ignition processes will be explored with CFD simulation to improve fundamental understanding on how liquid fuel physical and chemical properties influence the ignition behavior, which will provide critical knowledge for designing engines and its operating strategies.

The research questions that will be addressed throughout this thesis are:

- Which temperature dependent physical properties of liquid fuel have significant effects on the spray characteristics and ignition delay time of reacting sprays? Which liquid fuel physical properties should be emulated by diesel combustion surrogates?
- How these properties affect the ignition process of reacting sprays?
- Can a surrogate palette with a reasonable number of surrogate components emulate physical and chemical properties of various types of jet fuels?
- Which has more dominant impact on the diesel ignition process, liquid fuel physical properties or chemical properties?

The document is organized as follows.

Chapter 2 investigates the effect of liquid physical properties on spray characteristics and ignition behavior using CFD simulation. Through this numerical study, fuel physical properties that should be emulated by the surrogate fuel are identified. Also, a detailed analysis on how these liquid physical properties influence the spray ignition process is carried out.

Chapter 3 outlines the surrogate optimization framework including the development of the surrogate optimizer and the surrogate palette. The physical properties that were identified as being important to diesel ignition in Chapter 2 are included as the surrogate target properties. New surrogate fuels for conventional and alternative jet fuels formulated by the surrogate optimizer are also reported here.

Chapter 4 presents the kinetic modeling results of the newly developed surrogates in Chapter 3 using a detailed kinetic mechanism. Also, the skeletal version of the detailed chemical mechanism is generated.

In Chapter 5, the CFD simulations of reacting sprays using the fuel surrogates from Chapter 3 and the skeletal mechanism from Chapter 4 are conducted to examine the relative importance of physical and chemical aspects of the spray ignition process.

Finally, Chapter 6 presents summaries, conclusions, and recommendations for future work.

1.6 Relevant Publications

The topics in this dissertation have been reported in the following publications.

1. **Doohyun Kim**, Jason Martz, and Angela Violi, “A surrogate for emulating the physical and chemical properties of jet fuel.” The 8th U.S. National Combustion Meeting, Paper # 070IC-0269
2. **Doohyun Kim**, Jason Martz, and Angela Violi, “A surrogate for emulating the physical and chemical properties of conventional jet fuel.” Combustion and Flame 161.6 (2014): 1489-1498.
3. **Doohyun Kim,** Jason Martz, Andrew Abdul-Nour, Xin Yu, Marcis Jansons, and Angela Violi, “An inclusive six-component surrogate for emulating the physical and chemical characteristics of conventional and alternative jet fuels and their blends.” Submitted to 36th International Symposium on Combustion.
4. **Doohyun Kim,** Jason Martz, and Angela Violi, “Effects of fuel physical properties on direct injection spray and ignition behavior”. Submitted to Fuel.

In addition, experimental validations of the surrogates conducted by companion projects are/will be available in the following publications.

1. Xin Yu, Xi Luo, Marcis Jansons, **Doohyun Kim**, Jason Martz, and Angela Violi, “A Fuel Surrogate Validation Approach Using a JP-8 Fueled Optically Accessible Compression Ignition Engine.”, SAE International Journal of Fuels and Lubricants 8.2015-01-0906 (2015): 119-134.
2. Dongil Kang, Vickey Kalaskar, **Doohyun Kim**, Jason Martz, Angela Violi, and Andre Boehman, “Experimental Study of Autoignition Characteristics of Jet-A Surrogates and their Validation in a Motored Engine and a Constant Volume Combustion Chamber.”, publication in preparation.

Tables

Table 1.1. Compositions of previous jet fuel surrogates.

Reference	Guéret [36] Vol %	Patterson [37] Mol %	Dagaut [38] Mol %	Violi [39] Vol %	Honnet [42] Wt %	Dooley [29] Mol %
n-undecane	79					
n-dodecane				73.5		40.41
n-decane		89	74		80	
iso-octane				5.5		29.48
methylcyclohexane				10		
n-propylcyclohexane	10		11			
benzene				1		
toluene		11		10		
1,2,4-trimethylbenzene	11				20	
1,3,5-trimethylbenzene						7.28
n-propylbenzene			15			22.83

Figures

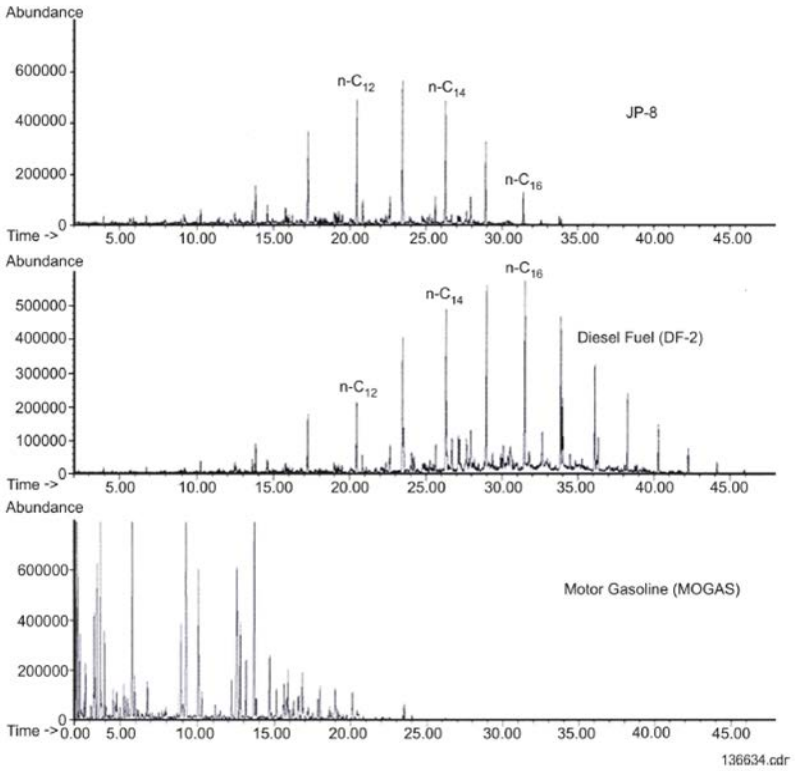

Figure 1.1. Gas chromatograms of JP-8, diesel fuel, and motor gasoline [20].

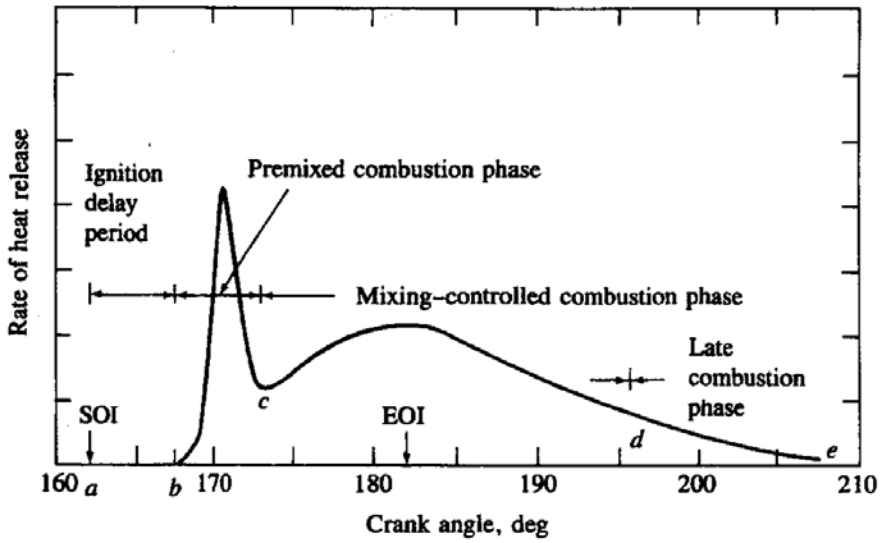

Figure 1.2. Typical diesel engine heat release rate profile from Heywood [32] illustrating different combustion phases.

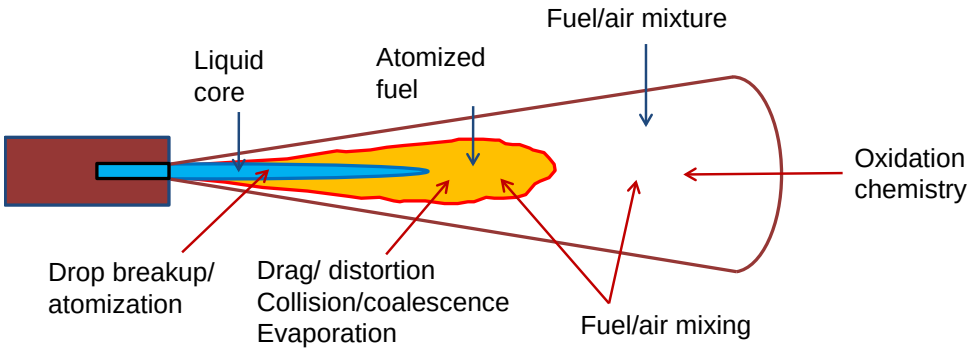

Figure 1.3. Conceptual schematics of physical and chemical processes during ignition delay period in direct-injected diesel engine.

Chapter 2

Effects of Fuel Physical Properties on Spray Ignition Behavior

2.1 Background

For modern compression ignited diesel engines, which employ direct fuel injection, the physical properties of liquid fuel influence the spray, mixture development and ultimately the ignition and combustion process [49]. To date, most studies into the importance of liquid fuel physical properties to compression ignited combustion behavior have been experimental. Studies by Naber and Siebers [50] and Siebers [51,52] investigated the effect of various parameters on liquid penetration and observed that lower fuel volatility resulted in longer liquid length. Higgins et al. [53] tested nine different fuels and proposed a liquid penetration correlation as a function of fuel density and the energy required to vaporize the liquid fuel. Genzale et al. [54] compared diesel and biodiesel sprays under conditions relevant to late-cycle post-injection and showed ~15 % longer liquid penetration lengths for biodiesel. Kook and Pickett [55] tested a variety of jet fuels and showed that while the variations in vapor penetration lengths of the different fuels were within the experimental uncertainties, liquid penetration length was affected by liquid density and volatility. Wu et al. [56] observed that the viscosity of

oxygenated fuels influenced spray atomization behavior. Other experimental comparisons have been made to assess the sensitivity of engine performance, emissions, and spray characteristics to the properties of alternative diesel fuels, such as dimethyl ether (DME), biodiesel, and jet fuels, which are significantly different from those of petroleum derived diesel fuel [14,57–60].

While these experiments provided valuable insights, it is difficult to isolate the effect of each property by comparing experimental results using different fuels where several fuel physical properties are varying simultaneously. Computational studies can be used to isolate these effects and their influence on the complex processes occurring during spray combustion. Only a limited number of numerical investigations have examined liquid fuel property effects, including the work of Som et al. [61], which quantified the differences between the injection and spray characteristics of biodiesel and diesel fuel. Pei et al. [62] conducted a sensitivity analysis with a diesel engine simulation to assess the relative effects of various physical properties including density, heat of vaporization, vapor pressure, and viscosity. While parameters other than fuel properties (such as select model constants and injector-related parameters) were shown to be the most sensitive variables, the liquid fuel density was shown to affect ignition delay, combustion phasing, and emissions. CFD simulations by Ra et al. [63] predicted that density, vapor pressure, and surface tension had the largest effect on cylinder pressure and combustion phasing. However, these studies focused on engine performance parameter sensitivity rather than on understanding how physical property variations affect spray formation and ignition behaviors.

This chapter investigates the effects of temperature-dependent liquid fuel physical properties (such as density and viscosity) on spray penetration, the evolution of local thermodynamic states within the jet, and the ignition delay period of compression ignited combustion. These effects are predicted using a validated CFD simulation of a free fuel jet. Through such efforts, the surrogate optimization processes can be better informed during the development of future surrogate fuels.

2.2 Model Configuration

Spray characteristics were predicted under diesel-relevant conditions with the CFD package CONVERGE [64]. The Reynolds Averaged Navier Stokes (RANS) equations with the RNG k-ε model were utilized to model the turbulence in the gas-phase flow field. Automatic mesh refinement and fixed embedding near the nozzle were used to increase the solution's spatial resolution with a minimum increase in computational expense [64].

The two-phase processes within the spray were modeled with the Lagrangian-Droplet and Eulerian-Fluid approach. The dynamics of the fuel spray droplet were described with a number of phenomenological and physical models. The blob injection method of Reitz and Diwakar [65] was employed. The Kelvin-Helmholtz – Rayleigh-Taylor (KH-RT) model, without the use of an ad hoc breakup length definition, was used to predict the breakup and atomization of the injected fuel parcels [64]. Liquid droplet collision and coalescence was modeled with the No Time Counter collision model [66] in conjunction with the Post collision outcome model [67]. The dynamic drop drag model of Liu et al. [68] was utilized to account for the change of the drag coefficient due to droplet

deformation. A standard droplet turbulent dispersion model [69] was included, while droplet evaporation was predicted with the Frossling correlation [69]. Based on the work of Senecal et al. [70] that showed asymptotic convergence of the spray characteristics with grid refinement, the minimum grid size in the adaptive mesh refinement algorithm and the total number of injected parcels were set to 0.25 mm and 512,000, respectively; the base mesh size was 2 mm.

Pure n-dodecane, which is often used as an n-alkane representative within jet fuel and diesel fuel surrogates [21,25], was used as the fuel in the current work. Temperature-dependent liquid n-dodecane physical properties were taken from the DIPPR database [71]. A recently published reduced mechanism with 255 species and 2289 reactions was used to model n-dodecane oxidation [72]. The mechanism was validated against several experimental data sets reported in [72], including ignition delay times from shock tube and rapid compression machine studies, species time histories obtained from shock tube experiments, concentration profiles from a pressurized flow reactor, and laminar flame speed. Specifically, the ignition delay times calculated with the mechanism were shown to follow the experimental measurements over a wide range of temperatures (750 K ~ 1400 K), pressures (12 atm ~ 46 atm) and equivalence ratios (Φ = 0.5 ~ 1).

2.3 Model Validation

The model was validated by comparison with experimental data from a constant-volume combustion vessel at Sandia National Laboratories [73–75] that utilized the Spray A injector (serial number 210677). The computational mesh was a 108 mm cubic chamber, which was identical to the geometry of Sandia's combustion vessel.

Liquid/vapor penetration lengths and vaporized fuel mass fraction distributions from two non-reacting spray experiments (ambient conditions of 900 K 6.1 MPa 22.8 kg/m^3 and 1100 K 5.0 MPa 15.2 kg/m^3) were used, along with ignition location and ignition delay times from three reacting spray experiments at ambient density of 22.8 kg/m^3 (750 K 4.9 MPa, 900 K 6.1 MPa, and 1200 K 7.9 MPa). The ambient temperatures and pressures of the validation cases are relevant to the ignition conditions within diesel engines. More details of the n-dodecane spray experiments are summarized in Table 2.1. The injector specifications, the rate of injection profile and all of the simulation boundary conditions were taken from the experiments. In the CFD simulations, the liquid penetration length was defined as the axial distance from the nozzle exit to the region that encompassed the 95th percentile of the total liquid fuel mass at a given time, while the vapor penetration length was defined as the maximum axial distance from the nozzle exit to where the fuel mass fraction is 0.1 %. The ignition delay in the simulations was defined as the time between start of the injection and the maximum rise rate of peak temperature [62]. A model constant in the KH-RT breakup model (B_1) was set at 8.5 for all simulations.

Figure 2.1 shows good agreement between the predicted and experimental liquid and vapor penetration lengths as a function of time for non-reacting spray simulations. The uncertainties associated with the experimental measurements were less than 1 mm for the bulk of this data [73]. While improvements are necessary in the initial liquid length predictions, the model is able to predict stabilized liquid penetration lengths and overall vapor penetration trends. The root mean squared errors of the stabilized liquid penetration and vapor penetration lengths were 0.4 mm and 2.8 mm for the 900 K 22.8 kg/m^3 case, and 0.8 mm and 2.9 mm for the 1100 K 15.2 kg/m^3 case.

The steady-state radial and axial distributions of the vapor fuel mass fraction are compared in Figure 2.2, again for the non-reacting cases. The simulation results were taken at 1.4 ms after the start of injection, when the jet was steady. As shown in Figure 2.2, the model was capable of capturing the general radial and axial fuel vapor distribution trends. At 25 mm downstream from the injector tip, the predicted radial mass fractions for the two test cases were largely within the experimental uncertainties. For the axial distributions at the jet centerline, the fuel vapor mass fraction for the 900 K, 22.8 kg/m^3 case was within the experimental uncertainties from ~20 mm to ~30 mm, however the fuel vapor mass fraction was under-predicted for larger axial distances. The calculated axial vapor fuel mass fraction was in better agreement with the experiments for the 1100 K, 15.2 kg/m^3 case.

For the reacting spray simulations, the n-dodecane reaction mechanism [72] was included without changing any of the spray model parameters used in the non-reacting set up. All of the ambient conditions were taken from the experiments, with the exception of the ambient temperature of 750 K 22.8 kg/m^3 case, which needed to be increased by 30 K for agreement with the experimental ignition delay time. Figure 2.3 shows the ignition delays from the simulation and the experiments. Although ignition delay times were slightly over-predicted, the model was capable of capturing the ignition delay trend over a wide range of temperatures. To validate the spatial ignition location, Figure 2.4 compares high temperature chemiluminescence images from the experiments to the local temperatures from simulation. As can be seen for all three cases, the model was capable of qualitatively predicting the spatial location of high temperature chemiluminescence, with the highest temperature regions near the start of the ignition.

These comparisons show that the model successfully captures the experimental liquid and vapor penetration lengths, the spatial fuel vapor distribution at steady state for non-reacting spray, along with the ignition delay time and ignition location for reacting sprays. This modeling set up is used as the baseline for the following simulations where the physical properties of the liquid fuel are perturbed.

2.4 Liquid Physical Property Perturbation Methodology

A sensitivity analysis was conducted with reacting spray simulations at two ambient conditions (900 K, 22.8 kg/m^3, and 750 K, 22.8 kg/m^3) to identify the liquid fuel properties that are of significance to the liquid spray penetration length and ignition delay. The vapor penetration length was not analyzed in detail here, given that the change in vapor penetration due to fuel liquid physical property perturbation was very small in the simulations, which is consistent with the experimental observations in Kook and Pickett [55], where the variation in vapor penetration length for fuels with different liquid properties was shown to be smaller than the experimental uncertainties.

Six liquid physical properties appearing in the spray models of the current work were examined, including density, vapor pressure, viscosity, surface tension, heat of vaporization, and specific heat capacity. Beginning with the baseline n-dodecane properties, the individual fuel properties were perturbed one at a time by multipliers which were determined to cover the minimum and maximum property values of the various hydrocarbons used in recent diesel and jet fuel surrogate studies [27–29]. n-heptane, n-decane, iso-octane and iso-cetane were considered for linear alkanes; methylcyclohexane and decalin for cycloalkanes; and toluene, 1,3,5-trimethylbenzene

and n-propylbenzene for aromatics. The reason for implementing this method rather than the more conventional approach of using consistent relative changes of each property was that the properties considered in this study have a drastically different range of magnitudes among the various species. For example, decalin has the highest density among the above pure components, which is about 20% greater than that of n-dodecane. However, n-heptane has highest vapor pressure, which is 10 ~ 20 times greater than that of n-dodecane, depending on temperature. Due to this significant difference among the properties, perturbing the properties with a common multiplier does not represent the real property variations within the surrogate components. Therefore, multiplier perturbations of varying relative differences were performed with this approach and are summarized in Table 2.2.

The modeling parameters were maintained from the baseline case for all of the perturbation simulations, with the exception of the injected fuel mass flow rate and the injection velocity for the density perturbation study. The relationship among the mass flow rate ($\dot{m}_{fuel}$), the fuel injection velocity (U_{fuel}), the pressure drop across orifice (P_{fuel} - P_{amb}), the momentum flow rate of the liquid fuel through the orifice ($\dot{M}_{fuel}$), and liquid fuel density (ρ_{fuel}) can be expressed using mass conservation and Bernoulli's equation, as shown in [50,73]:

$$\dot{m}_{fuel} = C_d \cdot A_{orifice} \cdot \sqrt{2 \cdot \left(P_{fuel} - P_{amb}\right) \cdot \rho_{fuel}} \qquad \text{(Eq. 1)}$$

$$U_{fuel} = \sqrt{\frac{2 \cdot \left(P_{fuel} - P_{amb}\right)}{\rho_{fuel}}} \qquad \text{(Eq. 2)}$$

$$\begin{aligned} \dot{M}_{fuel} &= \dot{m}_{fuel} \cdot U_{fuel} \\ &= 2 \cdot C_d \cdot C_v \cdot A_{orifice} \cdot \left(P_{fuel} - P_{amb}\right) \end{aligned} \qquad \text{(Eq. 3)}$$

where C_d is the discharge coefficient, C_v is the velocity coefficient, and $A_{orifice}$ is the orifice exit area. As seen in Equation 1 and 2, the mass injection rate ($\dot{m}_{fuel}$) and the injection velocity (U_{fuel}), which are the key injection related parameters, are coupled by the pressure drop across the orifice and the liquid fuel density. Thus, it is impossible to keep all of the injection parameters constant when the liquid density is perturbed, and only one of the parameters can be chosen to be the same as the baseline case.

To be consistent with spray experiments [53–55] where constant injection pressure is applied regardless of the liquid fuel density, the density perturbation in this study was made while maintaining the pressure drop across orifice (P_{fuel} - P_{amb}). As a result, the fuel mass flow rate was proportional to $\rho_{fuel}^{0.5}$, and the injection velocity was proportional to $\rho_{fuel}^{-0.5}$ for the density perturbation cases, as indicated by Equations 1 and 2. Also, a constant pressure drop resulted in constant jet momentum flow rate (Equation 3). This relationship has been experimentally validated by Genzale et al. [54] for sprays of regular diesel and higher density biodiesel at a constant injection pressure.

2.5 Results – Liquid Penetration Length

Figure 2.5 summarizes the relative change in the liquid penetration length for the physical property perturbations. While perturbations of density, vapor pressure, viscosity, and specific heat resulted in ± 4 ~ 10 % changes in liquid penetration for the 900 K case and ± 5 ~ 18 % changes for the 750 K case, surface tension and heat of vaporization perturbations caused a at most a ± 2 % change in liquid penetration length. Although all six physical properties considered in this study are included in one or more spray submodels (breakup model, evaporation model, etc.) as model parameters, this

observation indicates that the impact of surface tension and heat of vaporization on the predicted liquid penetration length is considerably smaller than the other four properties under the conditions studied. When the sensitivity factor, which is defined as the % change in liquid penetration length over the % change in physical property, is plotted as shown in Figure 2.6, liquid penetration length was most sensitive to density and specific heat for both conditions. Details on how these property perturbations affect liquid penetration are discussed in the following sections.

2.5.1 Viscosity and Surface Tension Effects

It has been shown that greater liquid fuel viscosity and surface tension slow the droplet breakup and atomization process [76,77] which in turn contribute to longer liquid penetration lengths. From a modeling standpoint, both viscosity and surface tension play a significant role in spray breakup, as they determine the Reynolds and Weber numbers, which are key model parameters. The results in Figure 2.5 replicated the expected experimental trends – the liquid penetration length gets longer as viscosity and surface tension increase. However, the variation in surface tension over the relatively large range of hydrocarbon molecules considered in this study did not have a significant effect on liquid penetration length. The magnitudes of the surface tension and viscosity sensitivity factors shown in Figure 2.6 were not significantly different, which also confirms that the substantial difference in liquid penetration length shown in Figure 2.5 is caused by much larger variations in viscosity. The more significant effect of viscosity is consistent with previous experimental analysis [77], where viscosity, and not surface tension, was the

dominating factor to changes in the Sauter Mean Diameter (SMD) of various liquid fuel sprays.

2.5.2 Specific Heat and Heat of Vaporization Effects

Another physical factor influencing liquid penetration length is the total thermal energy required to heat up and vaporize liquid fuel, as experimentally shown in Siebers [52] and Higgins et al. [53]. The correlation from these experiments implies that higher fuel specific heat and latent heat of vaporization result in longer liquid lengths. An energy balance for a single liquid droplet with a uniform temperature that vaporizes when heated by the ambient can be used to understand the importance of these properties:

$$A_d q_d = C_{p,liq} m_d \frac{dT_d}{dt} - \frac{dm_d}{dt} h_{vap} \qquad \text{(Eq. 4)}$$

where A_d is the droplet surface area, q_d is the heat flux from the ambient to the droplet, T_d is the droplet temperature, $C_{p,liq}$ is the specific heat of the fuel at T_d, m_d is the droplet mass at T_d, and h_{vap} is the heat of vaporization at T_d. Equation 4 implies that the heat transferred from the ambient to the liquid fuel is used either for increasing the liquid temperature or for causing the phase to change from liquid to vapor. Integrating Equation 4 over the lifetime of the evaporating liquid droplet provides Q_{total}, the total heat transfer needed from the ambient to vaporize the liquid droplet:

$$\int_{t_{init}}^{t_{end}} A_d q_d dt = \int_{T_{d,init}}^{T_{d,end}} C_{p,liq} m_d dT_d - \int_{m_{d,init}}^{m_d=0} h_{vap} dm_d$$

$$Q_{total} = \int_{T_{d,init}}^{T_{d,end}} \left(C_{p,liq} m_d - h_{vap} \frac{dm_d}{dT_d} \right) dT_d \qquad \text{(Eq. 5)}$$

where t_{init}, $T_{d,init}$ and $m_{d,init}$ are the initial time, temperature, and mass of the droplet, and t_{end} and $T_{d,end}$ are the final time and droplet temperature when the droplet mass reaches zero. Note $C_{p,liq}$, m_d, and h_{vap} are all functions of the droplet temperature. Since dm_d/dT_d is negative for a vaporizing droplet, it is clear from Equation 5 that higher specific heat and heat of vaporization will result in a greater amount of heat transfer from the ambient to vaporize the liquid fuel. As seen in Figure 2.5, the simulation results were consistent with this analysis and the experimental observations, where greater specific heat and heat of vaporization resulted in longer liquid penetration lengths.

However, contrary to the specific heat cases, varying the heat of vaporization caused only a very small change in liquid length. Not only was the relative change in liquid penetration length small, but the sensitivity factor for the heat of vaporization was significantly smaller than the specific heat, as shown in Figure 2.6. This is mainly due to the ambient pressures of the test conditions, which were much higher than the critical pressure of liquid n-dodecane. Note that while the vapor pressure of n-dodecane increases exponentially until it reaches its critical pressure of 1.8 MPa at 658 K, the ambient pressures were ~6 MPa for the 900 K case and ~5 MPa for the 750 K case, which are relevant to the TDC conditions in compression ignition engines [52]. Under such high pressures, the evaporation model used in the current study [69] predicts that the bulk of evaporation occurs at liquid temperatures close to the critical temperature where the vapor pressure is the highest, because the ratio between the vapor pressure of the liquid fuel and the ambient pressure (p_{vap}/p_{amb}) is the key model parameter driving the evaporation process. In other words, when the droplet temperature is not close to the critical temperature, p_{vap}/p_{amb} is too small and causes a negligibly small amount of

evaporation to occur. Figure 2.7 illustrates the fraction of evaporating mass within each liquid temperature bin (10 K) relative to the total evaporating mass at a given time (0.2 ms) for the 900 K 22.8 kg/m^3 case, and clearly shows that the bulk of the phase change occurred at droplet temperatures over 600 K, which is in proximity to the critical temperature. $C_{p,liq}$ increases with liquid temperature, however h_{vap} decreases and eventually becomes zero at the critical temperature, as shown in Figure 2.8 for n-dodecane. Thus, when the liquid temperature approaches the critical temperature, the heat transfer needed for vaporization (Q_{total}) in Equation 5 is dominated by $C_{p,liq}$, with a much smaller contribution from h_{vap}. Therefore, in proximity to the critical temperature, the perturbation of the heat of vaporization has only a marginal effect on Q_{total}, resulting in a much smaller change in liquid penetration relative to the specific heat perturbations.

2.5.3 Density Effects

Increasing liquid fuel density has been shown to increase liquid penetration length in spray experiments [50,53–55]. The current simulation results in Figure 2.5 captured the expected trend, showing that the liquid penetration length is sensitive to liquid density variations. Also, the sensitivity factor of liquid length to fuel density was the highest among all the physical properties considered for both test conditions, as shown in Figure 2.6. This effect was a result of the entrainment rate, which is defined as the ratio of entrained ambient mass to the fueling rate, which is inversely proportional to the square root of the fuel density as analyzed in [50,54,55]. Thus, a higher liquid density requires the entrainment of additional ambient air, which demands more mixing time or a greater mixing length to complete the vaporization process.

2.5.4 Vapor Pressure Effects

Vapor pressure, a measure of liquid volatility, is a well-known fuel property that affects liquid penetration [52,53,55] by influencing the vaporization process. Higher vapor pressure enhances liquid fuel vaporization, resulting in shorter liquid penetration, which was well captured by the current model as shown in Figure 2.5 and Figure 2.6. An interesting observation is that the effect of vapor pressure was much more significant in the lower temperature case. Figure 2.5 shows that the same perturbations in vapor pressure resulted in a 4 ~ 6 % relative change in the 900 K case, but in a 13 ~ 18 % change in the 750 K case. Because of the faster heat transfer to the liquid fuel for the higher ambient temperature case, the effect of fuel volatility on liquid penetration is less pronounced in the 900 K case.

2.6 Results – Ignition Delay Time

To better understand the effect of the liquid fuel properties on the spray ignition characteristics under the simulated conditions, the calculated global heat release rates for the baseline cases are shown in Figure 2.9 (a) at 900 K 22.8 kg/m^3 and (b) at 750 K 22.8 kg/m^3. Two-stage ignition is predicted for both cases, including low temperature heat release (LTHR), negative temperature coefficient (NTC) behavior, and high temperature ignition chemistry. The LTHR phase in Figure 2.9 is defined as the period between the start of heat release and the first heat release rate peak, while the NTC period is defined as the time from the first heat release rate peak to the start of high temperature ignition, which is defined as the time when the maximum rise rate of peak temperature occurs [20].

The ignition process takes much longer for the 750 K case, primarily due to the longer duration of the LTHR and NTC phases of ignition.

Figure 2.10 shows the time evolution of the local temperatures during the ignition process for the 900 K 22.8 kg/m^3 case. In the temperature contours at 0.37 ms and 0.41 ms after the start of injection, the temperature rise is observed at the periphery of the spray where the equivalence ratio is 1~2. A similar initial temperature rise at the spray periphery was predicted in the work of Som and Aggarwal [78]. At 0.45 ms, high temperature chemistry, which leads to the ignition of the fuel spray, is about to start in the interior of the spray where the fuel/air mixture is slightly rich and local temperature is the highest. A similar ignition process was predicted for the 750 K case (not shown), with the initial heat release at the periphery of the spray and the onset of high temperature heat release in the spray interior.

The two stage ignition process within the n-dodecane spray can be better understood when the time evolution of local reactivity is determined during the ignition delay period, as shown in Figure 2.11. The local reactivity was calculated using a methodology similar to the one shown in Kodavasal et al. [79]. In this case, the local reactivity was represented by the inverse of the ignition delay time calculated from constant volume homogeneous reactor simulations initialized with the local temperature, pressure, and gas phase composition at a given instance of time in each cell of the fuel spray. These ignition delay calculations were performed using the zero dimensional chemistry solver included in the CFD package CONVERGE [64] with the same chemical mechanism as the CFD simulations. A shorter ignition delay time is indicative of higher mixture reactivity, hence the inverse of the calculated ignition delay time can be used to

gauge local reactivity and the preferential ignition sites within the spray. Figure 2.11 illustrates the local reactivity distribution during the ignition delay period for the 900 K 22.8 kg/m^3 case. During the LTHR phase (0.33 ms ~ 0.39 ms), it can be seen that the most reactive charge is located at the periphery of the spray where the temperature is greater than that of the jet interior and the equivalence ratio is near stoichiometric or slightly rich, which is in agreement with the location of the initial temperature rise observed in Figure 2.10. As time progresses (from 0.41 ms ~ 0.43 ms), ignition process enters the NTC regime and approaches high temperature ignition - the regions of peak reactivity gradually shift into the interior of the spray as a result of heat and mass transfer, where high temperature ignition eventually occurs.

Figure 2.12 summarizes the relative changes in ignition delay time with physical property perturbations for the (a) 900 K 22.8 kg/m^3 case and (b) 750 K 22.8 kg/m^3 case. For both conditions, the perturbations of specific heat and density have significant impact on the calculated ignition delay (-10 % ~ 9 % for specific heat, -7 % ~ 7 % for density); vapor pressure and the latent heat of vaporization have a small effect (-2 % ~ 1 %), while variations in viscosity and surface tension marginally affect ignition delay (less than 0.5 % at most). No meaningful deviations from the baseline cases could be observed for the viscosity and surface tension cases when local temperatures and equivalence ratio within the spray are compared, despite their effect on liquid length. On the other hand, the ignition delay time is much more sensitive to perturbations in specific heat and density than rest of the properties, which is also clearly seen in the sensitivity factors plotted in Figure 2.13. The reason for these behaviors is discussed in the following sections.

2.6.1 Specific Heat Effects

Figure 2.14 shows the calculated global heat release rates for the specific heat perturbation cases. For both test conditions, the specific heat perturbation had the largest impact on the calculated ignition delay, causing a -10 % to ~ 9 % deviation from the baseline cases. The entire ignition process from the start of low temperature heat release to the transition to high temperature chemistry was slowest for the perturbation with the greatest specific heat.

To understand this behavior's root cause, reactivity contours for n-dodecane/air mixtures were calculated for each test condition just prior to heat release in the equivalence ratio – temperature domain as shown in Figure 2.15; markers noting the Φ and T in each cell are plotted onto the contours. For both cases, it is clear that the local temperatures decrease with an increase in specific heat at a given equivalence ratio. This local temperature difference is caused by the change in the amount of heat that should be transferred from the ambient charge to the liquid fuel for its vaporization (Q_{total} in Equation 5) as a result of the liquid specific heat perturbation. With a higher specific heat, a larger increase in liquid sensible internal energy is required for a given liquid fuel temperature increase - this causes the lower local mixture temperature at a given time. These local temperature variations influence the local reactivity, where from the reactivity contour it is evident that the higher fuel specific heat case is colder and less reactive overall, resulting in a longer ignition delay.

Deviations in the ignition delay time caused by the specific heat perturbations, especially for the 750 K case, are ± ~0.2 ms, which is equivalent to ± ~2.4 crank angle degree at 2000 rpm. Such a change in ignition delay time or combustion phasing will

have an effect on engine performance. Thus, emulating the specific heat of the liquid fuel should be considered for surrogates intended for spray/compression ignited combustion.

2.6.2 Density Effects

Figure 2.16 shows the calculated global heat release rates for the density perturbation cases. Density affects the ignition delay time, showing up to a 7% deviation from the baseline case for the perturbations shown in Figure 2.12. An important observation is that the ignition delay time was retarded for the higher density 900 K case (3.6 % increase in ignition delay), while ignition was advanced with higher density for the 750 K condition (7.1 % decrease in ignition delay). Although the overall change in ignition delay time was not consistent, a common trend for each ignition event was the observation of slower progress in the first stage LTHR and faster transition to high temperature ignition during NTC period (or shorter NTC duration) with greater liquid density. One of the major reasons for these variations was the change in air/fuel mixing resulting from the density variations. In the following sections, the influence of liquid fuel density on air/fuel mixing and ignition behavior are investigated.

Liquid Density Effect on Turbulent Mixing

As discussed previously, the injection velocity (U_{fuel}) and the mass injection rate ($\dot{m}_{fuel}$) were changed as a result of the density perturbation while maintaining the injection momentum flow rate ($\dot{m}_{fuel}U_{fuel}$) and injection pressure. Since fuel injection is the driving force for turbulent mixing within the initially quiescent spray chamber, the change in fuel injection related parameters such as U_{fuel} and $\dot{m}_{fuel}$ impacts turbulent mixing rates. The

changes in mixing rates for the density perturbation cases are evident in the turbulent transport coefficients used within the RANS turbulence model of the current CFD simulations. Here, the turbulent diffusion of heat and mass are governed by the turbulent thermal diffusivity (K_t) and turbulent mass diffusivity (D_t) obtained from turbulent viscosity (μ_t) and turbulent Prandtl (Pr) and Schmidt (Sc) numbers:

$$K_t = K + c_p \frac{\mu_t}{\mathrm{Pr}_t} \quad \text{(Eq. 6)}$$

$$D_t = \frac{\mu_t}{\rho Sc_t} \quad \text{(Eq. 7)}$$

where K is the molecular thermal conductivity, c_p is the gaseous specific heat, ρ is the gaseous density, Pr_t is the turbulent Prandtl number, and Sc_t is the turbulent Schmidt number. Figure 2.17 compares the turbulent viscosities of the density perturbations for the 900 K case at 0.25 ms and clearly shows that μ_t is inversely proportional to the liquid fuel density. Since the turbulent thermal and mass diffusivities are determined by the turbulent viscosity as shown in Equation 6 and 7, the turbulent transport of heat and species should be slower for the higher fuel density case as a result of lower turbulent viscosity.

Similarities are observed when the mixing perturbation cases are simulated and compared against the density perturbation cases. The turbulent thermal and mass transport rates of the baseline case are adjusted by changing the turbulent Pr_t and Sc_t numbers. As indicated by Equation 6 and 7, higher Pr and Sc numbers reduce the rate of turbulent thermal and mass transport. Figure 2.18 compares the turbulent mass diffusivities of (a) the density perturbation cases and (b) the mixing perturbation cases. As shown in Figure 2.18 (a) and (b), these mixing perturbations and the liquid density

perturbations have a similar effect on the turbulent mass diffusivities, indicating that the different effects have a similar impact on mixing rates.

Although the momentum flow rate of the fuel injection was kept constant for these density perturbations, notable change in turbulent mixing was still observed as shown in Figure 2.17, which implies that an injection parameter other than $\dot{m}_{fuel}U_{fuel}$ caused such a deviation. To identify which injection parameter change caused this difference, three other density perturbations were performed (identical density perturbation range) with different parameters kept constant, which were the mass injection rate ($\dot{m}_{fuel}$), the injection velocity (U_{fuel}), and the kinetic energy flow rate from the fuel injection event ($\dot{m}_{fuel}U_{fuel}^2$). The relationship between these parameters and the liquid density depends on the density perturbation method as summarized in Table 2.3. For example, when the liquid density is perturbed while maintaining the kinetic energy flow rate from the fuel injection event of the baseline case, the momentum flowrate ($\dot{m}_{fuel} \cdot U_{fuel}$), the mass injection rate ($\dot{m}_{fuel}$), and the injection velocity (U_{fuel}) were proportional to $\rho^{1/3}$, $\rho^{2/3}$, and $\rho^{-1/3}$, respectively.

Figure 2.19 compares the local turbulent viscosities of four different density perturbations for the 900 K case at 0.25 ms after fuel injection. Of all the density perturbation methods investigated, the case that maintained the injection velocity of the baseline case (Figure 2.19 (c)) showed the smallest deviation from the baseline case in turbulent viscosity. Also, the level of deviations for all four methods correlates with the change in injection velocity as a result of density perturbation. Based upon the relationship shown in Table 2.3, the change in the injection velocity from the baseline case is in the order of the case with constant injection mass ($U_{fuel} \approx \rho^{-1}$), constant

momentum ($U_{fuel} \approx \rho^{-0.5}$), constant kinetic energy ($U_{fuel} \approx \rho^{-1/3}$), and finally constant injection velocity ($U_{fuel} \approx constant$), which is in the same order to the deviations in the turbulent viscosity as shown in Figure 2.19. In Figure 2.20, the turbulent viscosities of the density perturbation with constant velocity shown in Figure 2.19 (c) are compared in spatial image, which also confirms the similar level of turbulent viscosities. As a result, the global heat release rates of the density perturbations with constant injection velocity, especially during the first stage LTHR period, were the closest to the baseline case among the tested density perturbation methods as shown in Figure 2.21. Note the global heat release rates during LTHR phase (0.25 ms ~ 0.4 ms for the 900 K case in Figure 2.21 (a), 1 ms ~ 1.4 ms for the 750 K case in Figure 2.21 (b)) were virtually identical to the baseline cases. Also, the timing of the first peak of the heat release rate (or the end of the LTHR) did not shift as much as the density perturbations with constant injection momentum (Figure 2.16). The difference in the magnitude of heat release rate at the end of LTHR and during NTC period in Figure 2.21 may be attributed to the difference in the injected fuel mass, which was proportional to the liquid density. Such an effect is more obvious in the 750 K case in Figure 2.21 (b), where higher heat release rate due to increased injected fuel mass resulted in earlier onset of high temperature chemistry leading to shorter NTC duration.

From this analysis, it can be concluded that the major reason for the change in turbulent mixing rate as a result of liquid density perturbations with constant momentum flow rate (density perturbations in Figure 2.16) was the change in the injection velocity. Higher density reduces the injection velocity ($U_{fuel} \approx \rho^{-0.5}$), which results in slower turbulent mixing rates. This conclusion is consistent with analytic turbulent jet theories

[80]. For a free turbulent jet, theoretical analysis with the turbulent mixing length approach indicates that turbulent thermal and mass transport are proportional to the radial gradient of the mean velocity. Since the turbulence model used in this study (RNG k-ε model) incorporates the same approach, the generation of the turbulent kinetic energy and, consequently, the intensity of turbulent mixing depend on the radial gradient of the mean velocity. Thus, higher liquid density with slower injection velocity results in smaller radial velocity gradient, which leads to slower turbulent mixing.

Density Perturbation Effects on Mixing and LTHR

To see the effects of turbulent mixing on LTHR progress, the temperature-equivalence ratio distributions just before the start of heat release are shown in Figure 2.22 for the density perturbation with constant injection momentum. Unlike the specific heat perturbations, which showed three distinct bands clustered in the T and Φ domain of Figure 2.15, there were no such large deviations in the T - Φ distributions of the density perturbations, as the bands approximately overlapped. Thus, the reactivity of the spray before LTHR cannot be compared solely based upon the T - Φ distribution.

Alternatively, using the method shown in [79], the mass distributions in the local reactivity dimension can be used to distinguish the differences in overall charge reactivity. Taking the local pressure, temperature and composition from the sprays in Figure 2.22, the local reactivity of the density perturbation with constant injection momentum was calculated with the same method used for Figure 2.11. Figure 2.23 illustrates the mass distribution in the local reactivity space before the start of LTHR. The 900 K case as shown in Figure 2.23 (a) indicates that the spray with higher liquid fuel density has less

mass in the most reactive regime relative to the baseline case. This trend is more obvious for the 750 K case in Figure 2.23 (b), where the mixing effect is more pronounced due to the much longer ignition delay period. This reactivity distribution indicates that while the T - Φ distributions were overlapped to the baseline case as in Figure 2.15, the cell markers are for higher density case are less densely populated at the region where reactivity is the highest (Φ of 1~1.5 for the 900 K case, Φ of ~1 for the 750 K case). Thus, the slower turbulent mixing for the higher density case prepares the charge more slowly, creating a smaller mass of high reactivity mixture, which results in the slower LTHR reaction rates at a given time during the LTHR regime within Figure 2.16. Such an effect of the turbulent mixing rate on reactivity distribution before the start of LTHR is also observed in Figure 2.24, where the reactivity distributions of the density perturbations with constant injection velocity are shown. Since the change in turbulent mixing was the smallest when the injection velocity was kept constant as shown in Figure 2.19, the deviations in reactivity distribution was much smaller than the density perturbation with injection momentum constant as shown in Figure 2.23, in particular in the highest reactivity region. The tendency of higher density case to have more mass of mixture in lower reactivity region may be attributed to more injected fuel mass for higher density case. Above analysis confirms that the change in turbulent mixing was the key factor for the change in the progress of LTHR.

Density Perturbation Effects on Mixing and NTC duration

Despite the slower LTHR progress, the NTC duration becomes shorter for the higher density case as shown in Figure 2.16. This behavior can be better understood

through a numerical experiment where the turbulent thermal and mass diffusivities of the baseline case are artificially perturbed during the NTC period to isolate the effect of mixing on the NTC duration. Figure 2.25 compares the global heat release rate and peak temperature evolution of the 750 K case when the turbulent thermal and mass transport coefficients are perturbed at the start of the NTC period, indicated by the "perturbation start" line in the figure. The ranges of the Pr_t and Sc_t perturbations (x 0.9 ~ 1.1) reflect the change in turbulent thermal and mass diffusivity predicted for the density perturbation cases shown in Figure 2.18 (b). While the heat release rate profile is virtually unchanged until 1.8 ms in Figure 2.25 (a), it is evident that the local peak temperatures begin to diverge in Figure 2.25 (b) starting at 1.6 ms, with the slower mixing cases (higher Pr_t and Sc_t) achieving significantly higher peak temperatures and heat release rate at a given time. The T - Φ distributions during the NTC period (at 1.8 ms) are shown in Figure 2.26, where the slower mixing case (*Sc*, *Pr* x 1.1) achieves a ~ 30 K higher peak temperature than the faster mixing (*Sc*, *Pr* x 0.9) case. Since the cumulative heat release at 1.8 ms is very similar for both cases (see Figure 2.25 (a)), the local temperature difference is caused in part by the change in the rate of turbulent transport, where the slower mixing case reduces mixing rates with the colder surroundings, resulting in higher local temperature. Such an effect leads to the earlier onset of high temperature chemistry and is a prime reason for the shorter NTC durations with higher density. An identical trend was observed for the 900 K case when the turbulent mixing was perturbed during the NTC period (not shown).

As shown above, the liquid density perturbation with constant injection momentum influenced turbulent mixing rates, which have competing effects on LTHR

progress and NTC duration. Greater density makes the LTHR phase longer because it shifts the T - Φ distributions to favor lower reactivities (Figure 2.23), however the NTC duration is shorter with higher density, given that slower turbulent mixing rates allow peak temperatures to remain elevated during NTC (Figure 2.25). In addition, higher mass fueling rate of higher liquid density also results in shorter NTC duration due to increased chemical energy available from fuel. These effects are consistent for the 900 K and 750 K cases, as shown in Figure 2.27, which summarizes the deviations in LTHR peak timing (corresponding to the start of NTC) and NTC duration from the baseline case. Since the contribution of these two competing effects to the total ignition delay time measured by the onset of high temperature ignition changes drastically, the effect of fuel liquid density on ignition delay reverses when transitioning from 900 K to 750 K. As seen in Figure 2.27, the contribution from the deviations in LTHR progress is greater than that of NTC during the NTC duration for the 900 K case, while the change in NTC duration dominates the overall ignition delay change for the 750 K case. For this reason, the density effect on ignition delay could either increase or decrease the total ignition delay of the 900 K and 750 K cases.

2.7 Summary and Conclusions

CFD spray simulations were conducted to evaluate the effects of liquid fuel properties on liquid penetration length and ignition delay during compression ignited combustion. The perturbation of the liquid fuel physical properties was made to reflect the property ranges expected from hydrocarbon molecules that are frequently used in

petroleum-derived diesel and jet fuel surrogates. The following conclusions can be drawn from the current study:

1. Among the six physical properties considered in this study, density, viscosity, vapor pressure and specific heat had a significant impact on the liquid penetration length (from 4 % to ~ 18 %). The impact of surface tension and heat of vaporization on liquid penetration length were minimal.
2. Vapor penetration length was not significantly affected by any of the liquid physical property perturbations, which is consistent with experimental observations.
3. Under the simulated ambient conditions, ignition delay was very sensitive to perturbations in the liquid fuel's specific heat. -30 % ~ +20 % change in liquid specific heat resulted in -10 % to 9 % change in ignition delay time. A greater specific heat increased the energy required for fuel vaporization, resulting in lower mixture temperatures, a less reactive fuel spray and a longer ignition delay. This is an important finding since liquid specific heat has been often neglected as a target property during the development of surrogates for diesel/spray combustion.
4. Liquid density also had a significant effect on ignition delay time through its competing effects on LTHR and NTC duration. -8 % ~ + 20 % change in liquid density caused up to 7% change in ignition delay. With higher density, LTHR progress was slower, but NTC duration was also shorter. The main cause of this behavior was the change in turbulent thermal and mass transport rates due to the effect of liquid density on injection velocity. When different density perturbation methods were investigated, the density perturbation cases with constant injection velocity resulted in smallest deviations from the baseline case, in terms of the turbulent mixing rates and reactivity distribution before the start of initial heat release. This observation indicates the change in injection velocity was the primary reason for the change in turbulent mixing for the density perturbation cases. A lower mixing rate

in the higher liquid density case was slower to form a reactive mixture for the LHTR, however during the NTC period, it was beneficial for the earlier onset of high temperature chemistry by allowing higher local temperatures. In addition, increased available chemical energy by higher fueling rate also caused shorter NTC duration.

5. The relative contribution of these competing effects to the total ignition delay time changed depending on the ambient gas temperature, causing the importance of density to ignition delay to vary with ambient temperature.
6. Liquid fuel properties other than specific heat and density do not have significant impact on the ignition delay time.
7. Surrogates for spray/diesel combustion should consider emulating liquid density, specific heat, viscosity, and volatility of the target fuel to properly capture the liquid penetration and ignition delay characteristics of the target fuel.

Tables

Table 2.1. Details of experimental spray data from Sandia National Laboratories [73–75].

	Non-reacting		Reacting		
Temperature (K)	900	1100	900	1200	750
Density (kg/m^3)	22.8	15.2	22.8	22.8	22.8
Pressure (MPa)	6.1	5.0	6.1	7.9	4.9
Ignition Delay[a] (ms)	-	-	0.398	0.147	1.723
Injection Duration (ms)	1.5	1.5	1.5	1.5	2.5
Ambient Composition ($N_2/CO_2/H_2O/O_2$, molar)	0.8971/0.0652/0.0377/0		0.7515/0.0622/0.0362/0.15		
Fuel	n-dodecane, 373 K				
Injector	Spray A (Serial # 210677), Common rail, Single hole, 90 µm diameter				
Injection Pres. (MPa)	150 MPa				

[a] From the average of three optically measured ignition delays in [75]

Table 2.2. Multipliers assigned to baseline properties for their perturbations.

	Perturb Min	Perturb Max
Density	0.92	1.2
Vapor Pressure	0.41	10
Viscosity	0.4	2
Surface Tension	0.7	1.25
Heat of Vaporization	0.8	1.16
Specific Heat Capacity	0.7	1.2

Table 2.3. Effects of liquid fuel density on injection-related parameters for different density perturbation methods.

Density perturbation methods	Controlled parameter	Relationship with the liquid density			
		$\dot{m}_{fuel} \cdot U_{fuel}$	$\dot{m}_{fuel}$	U_{fuel}	$\dot{m}_{fuel} \cdot U_{fuel}^2$
Constant injection momentum	$\dot{m}_{fuel} \cdot U_{fuel}$	-	$\rho^{0.5}$	$\rho^{-0.5}$	$\rho^{-0.5}$
Constant injection mass flow rate	$\dot{m}_{fuel}$	ρ^{-1}	-	ρ^{-1}	ρ^{-2}
Constant injection velocity	U_{fuel}	ρ	ρ	-	ρ
Constant injection kinetic energy	$\dot{m}_{fuel} \cdot U_{fuel}^2$	$\rho^{1/3}$	$\rho^{2/3}$	$\rho^{-1/3}$	-

Figures

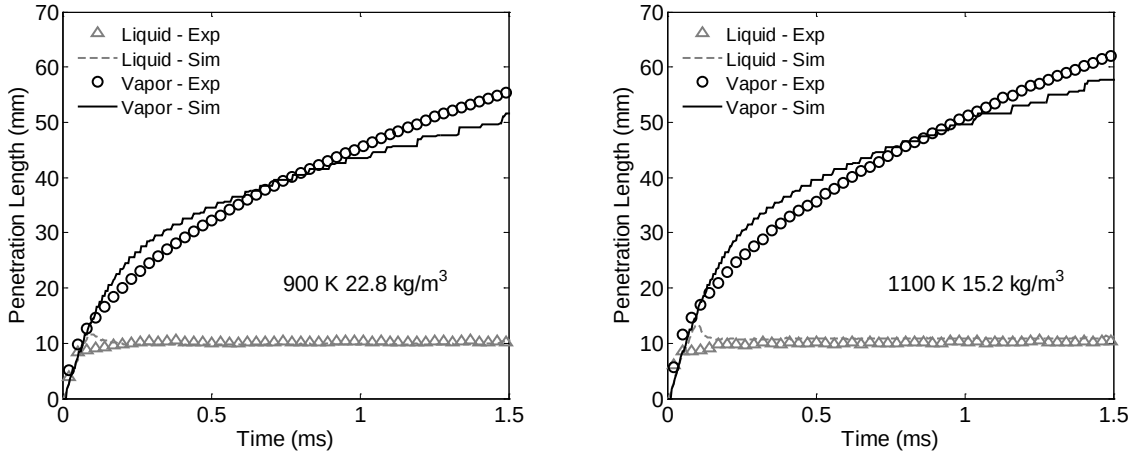

(a) (b)

Figure 2.1. Comparison of predicted and experimental liquid/vapor penetration lengths.

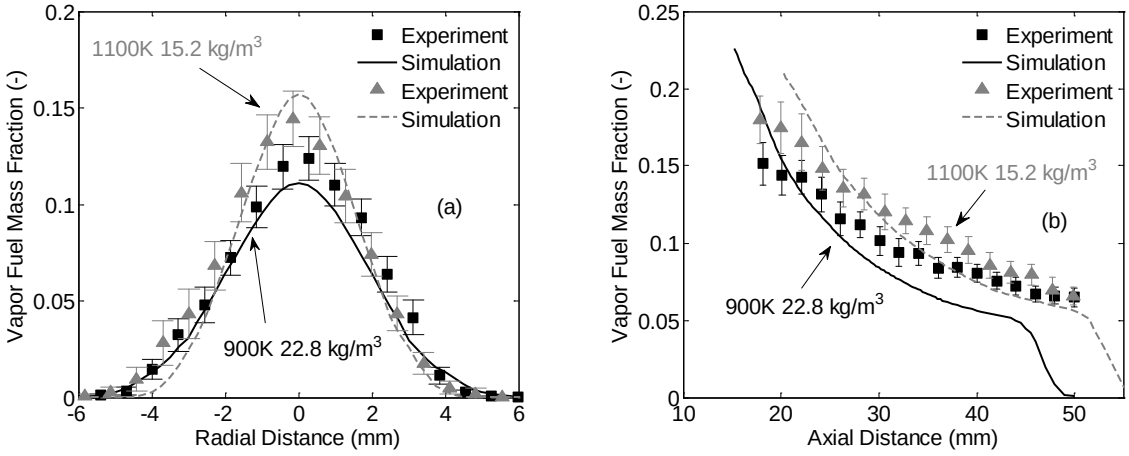

Figure 2.2. Comparison of predicted and experimental vapor fuel mass fraction [74] at (a) 25mm downstream from the injector tip and (b) at the jet centerline. The steady-state experimental data is compared against the simulation results at 1.4 ms after the start of the injection, when the jet was steady.

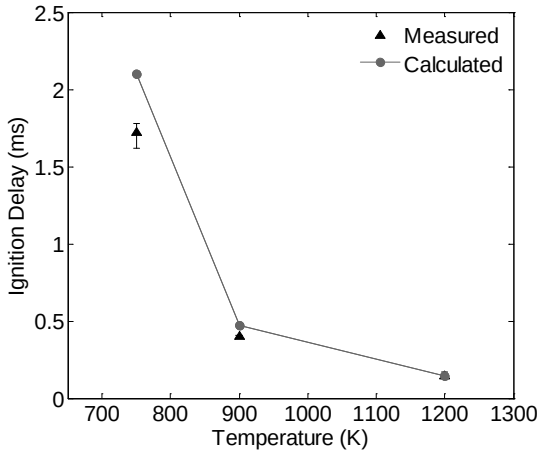

Figure 2.3. Comparison of measured and calculated ignition delays. Error bars show the minimum and maximum values from three experimental runs [75].

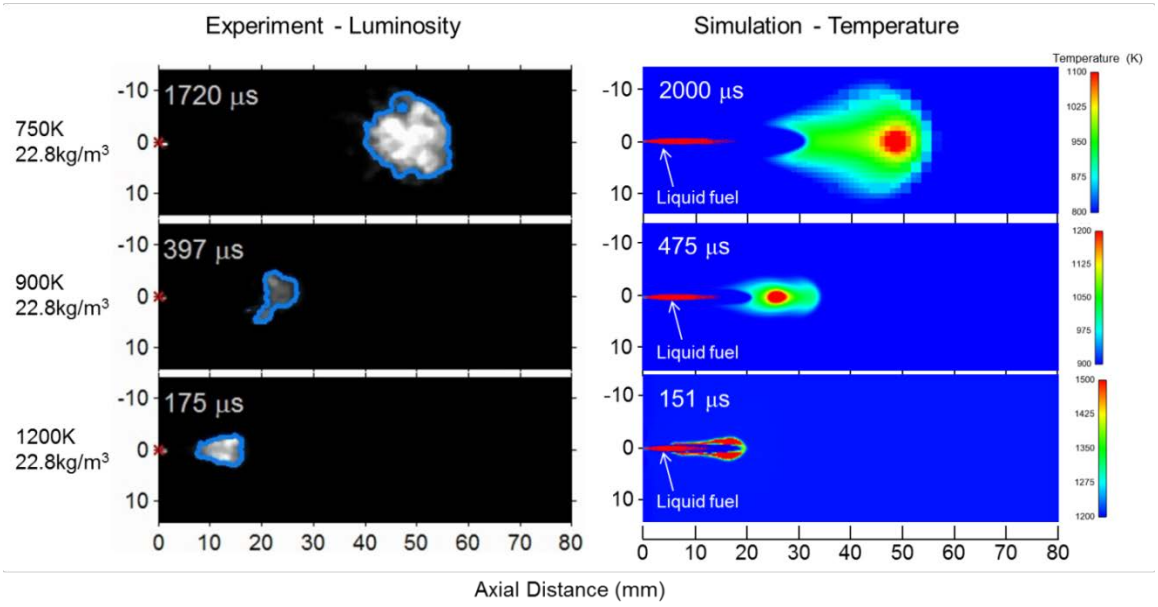

Figure 2.4. Comparison of high temperature chemiluminescence images from experiments [73] with the predicted local temperatures near the time of ignition for the reacting spray cases at a given time. Image times are noted for each case in the figure.

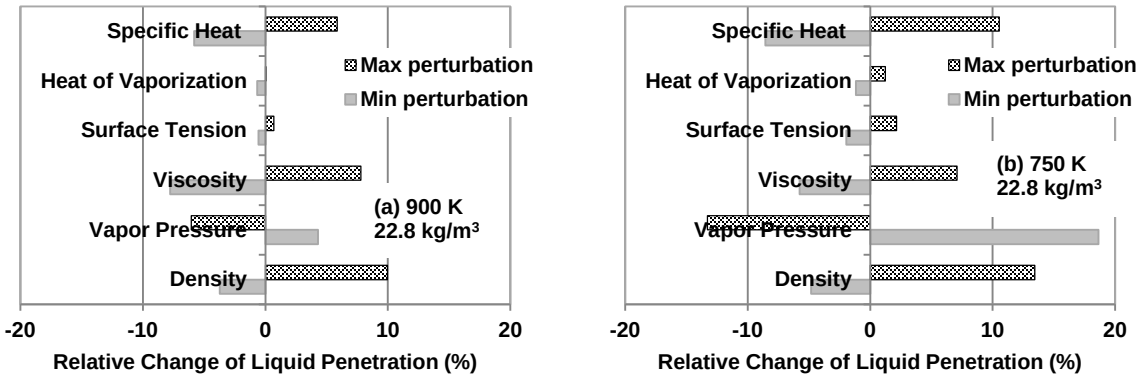

Figure 2.5. Relative change in liquid penetration length due to physical property perturbations at (a) 900 K 22.8 kg/m^3 and (b) 750 K 22.8 kg/m^3. The baseline liquid penetration length is 9.8 mm for (a) and 11.5 mm for (b).

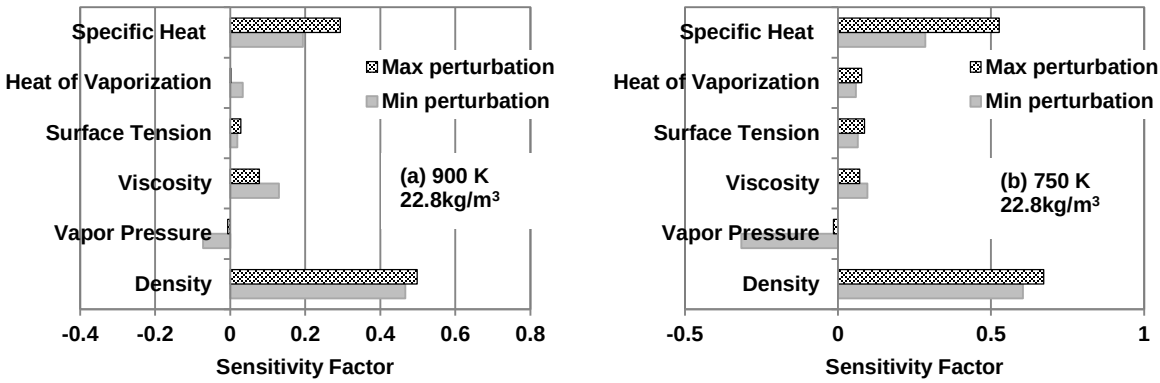

Figure 2.6. The sensitivity factor for liquid penetration length due to physical property perturbations at (a) 900 K 22.8 kg/m^3 and (b) 750 K 22.8 kg/m^3.

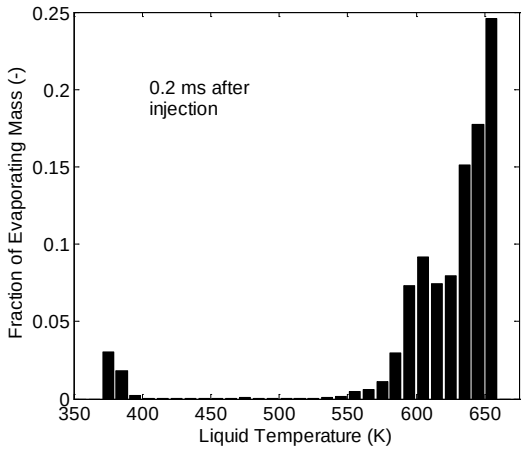

Figure 2.7. The evaporating mass fraction of each liquid droplet relative to the total evaporating mass at 0.2 ms after start of injection for the 900 K 22.8 kg/m^3 case.

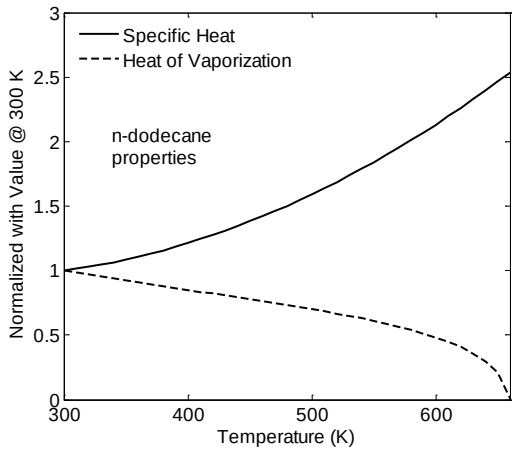

Figure 2.8. Temperature-dependent specific heat and heat of vaporization of liquid n-dodecane normalized to the 300 K value.

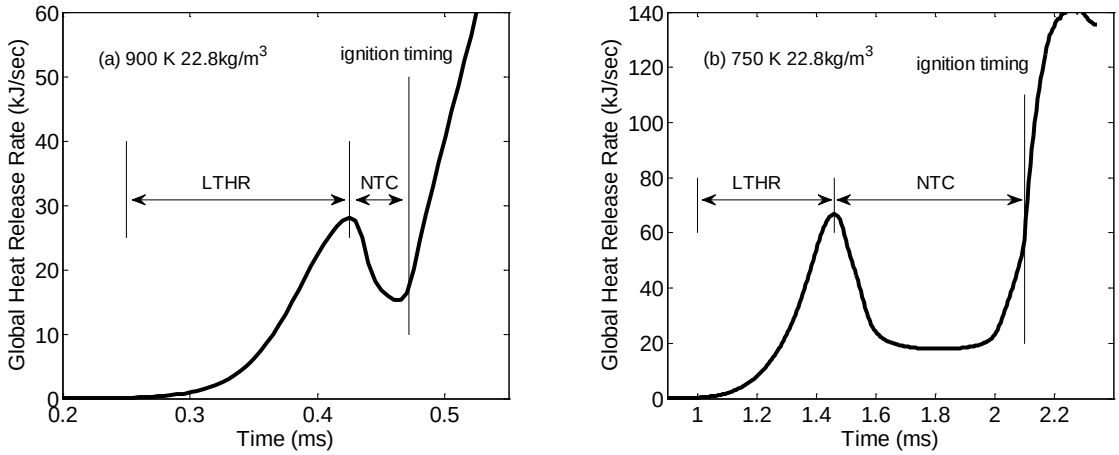

Figure 2.9. Calculated global heat release rates at (a) 900 K 22.8 kg/m^3 and (b) 750 K 22.8 kg/m^3 for the baseline cases. The ignition timing shown on the figure is defined as the time of the maximum rise rate of peak temperature. The baseline ignition delay is 0.47 ms for (a) and 2.10 ms for (b).

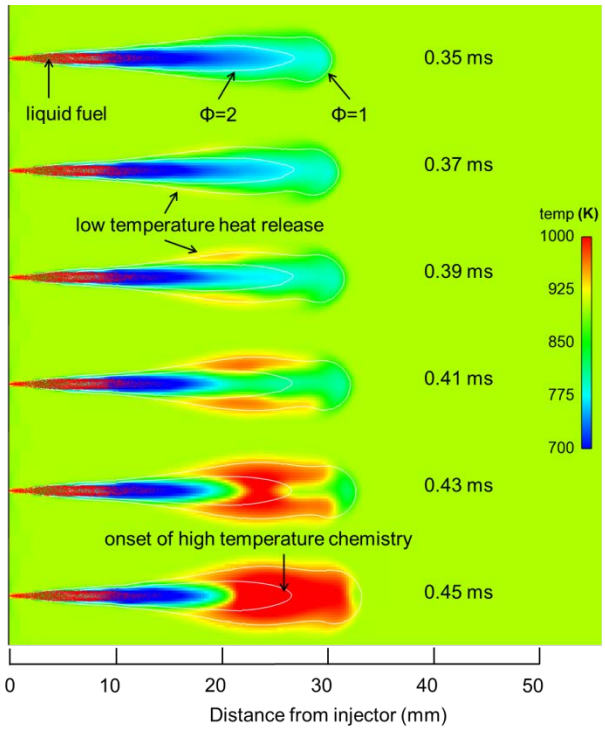

Figure 2.10. Calculated local temperatures and equivalence ratio contours at 900 K 22.8 kg/m^3 with the baseline fuel properties.

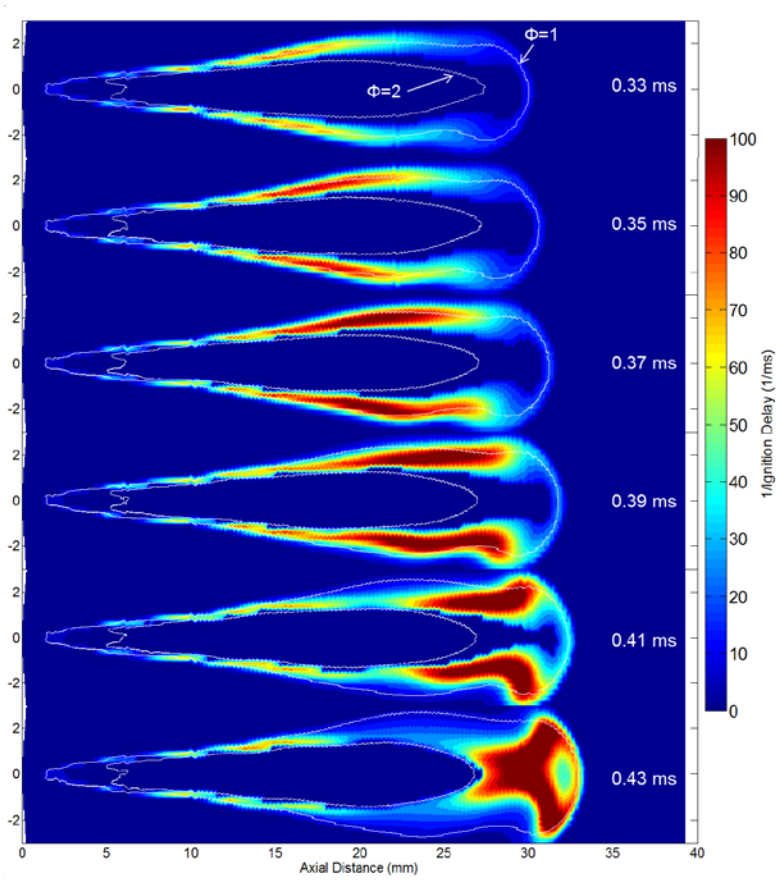

Figure 2.11. The local reactivity distributions and equivalence ratio contours during LTHR at 900 K 22.8 kg/m^3 with the baseline fuel properties.

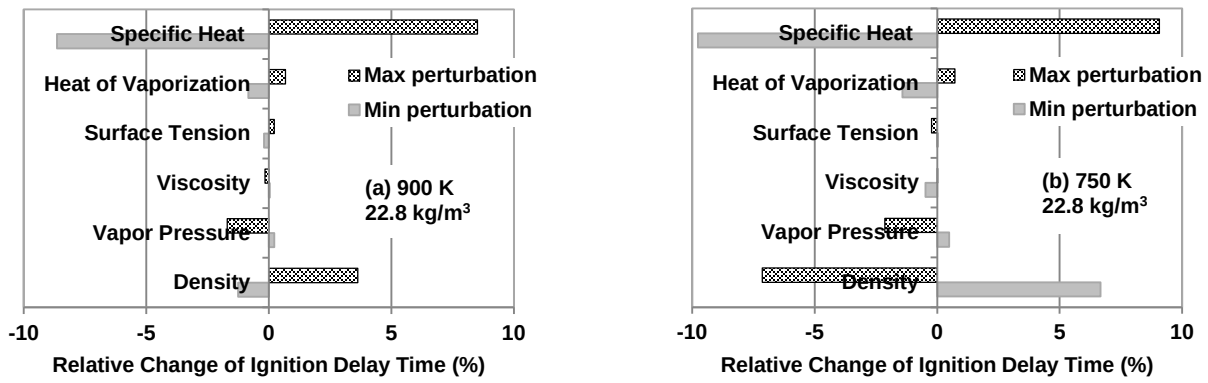

Figure 2.12. Relative change in ignition delay time due to physical property perturbations at (a) 900 K 22.8 kg/m^3 and (b) 750 K 22.8 kg/m^3. The baseline ignition delay is 0.47 ms for (a) and 2.10 ms for (b).

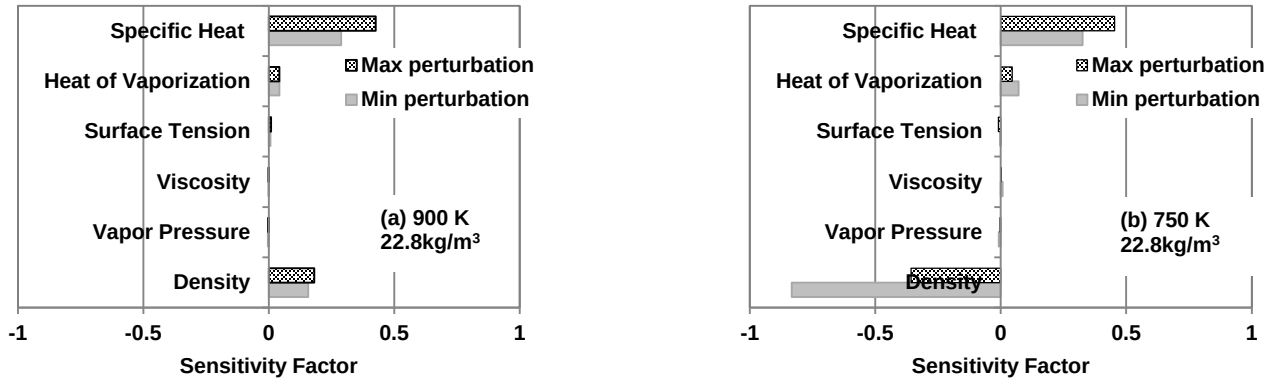

Figure 2.13. The sensitivity factor for ignition delay time due to physical property perturbations at (a) 900 K 22.8 kg/m^3 and (b) 750 K 22.8 kg/m^3.

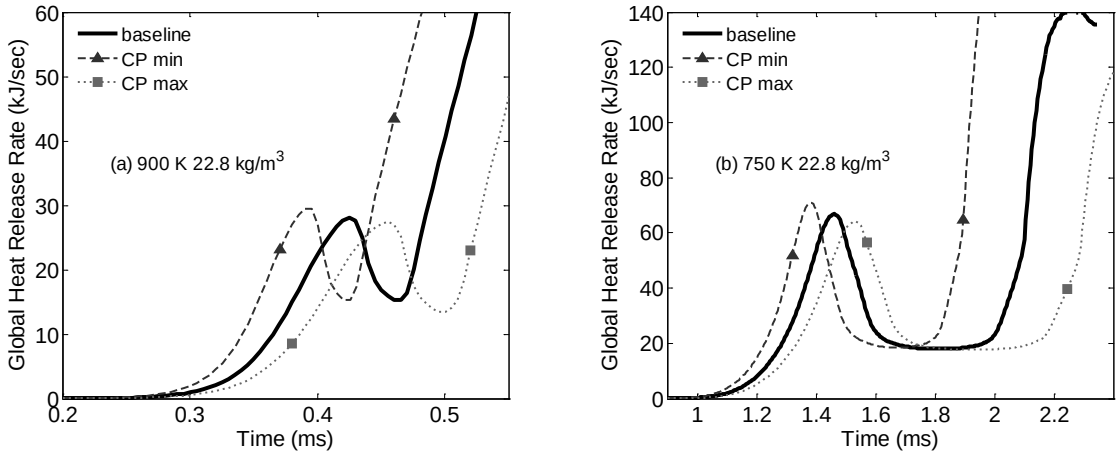

Figure 2.14. Comparisons of the calculated global heat release rates for the specific heat perturbation cases at (a) 900 K 22.8 kg/m^3 and (b) 750 K 22.8 kg/m^3.

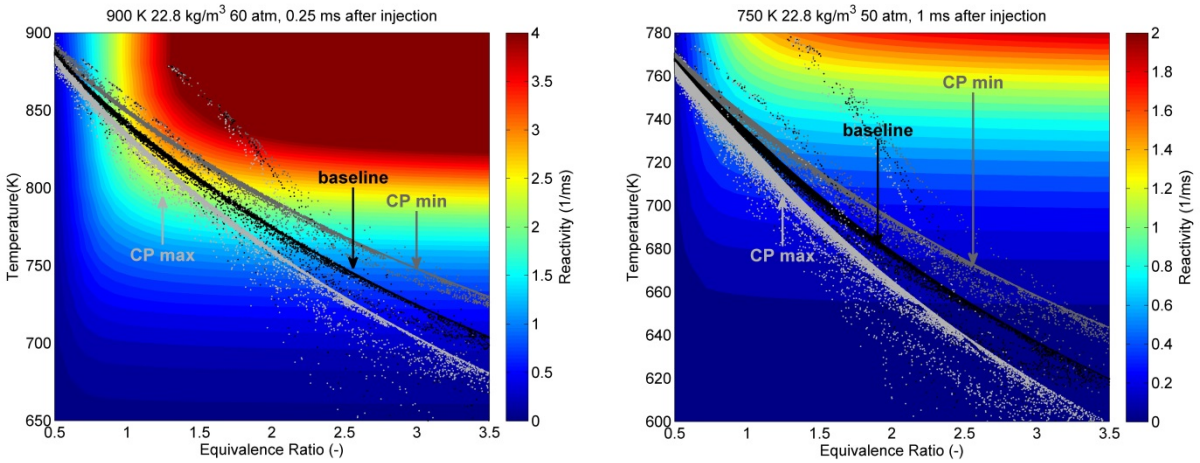

(a) (b)

Figure 2.15. The n-dodecane reactivity contour and temperature-equivalence ratio distribution within the spray before the start of LTHR for the specific heat perturbation cases. (a) 900 K 22.8 kg/m^3 at 0.25 ms after injection with the reactivity contour at 60 atm and (b) 750 K 22.8 kg/m^3 at 1 ms after injection with the reactivity contour at 50 atm.

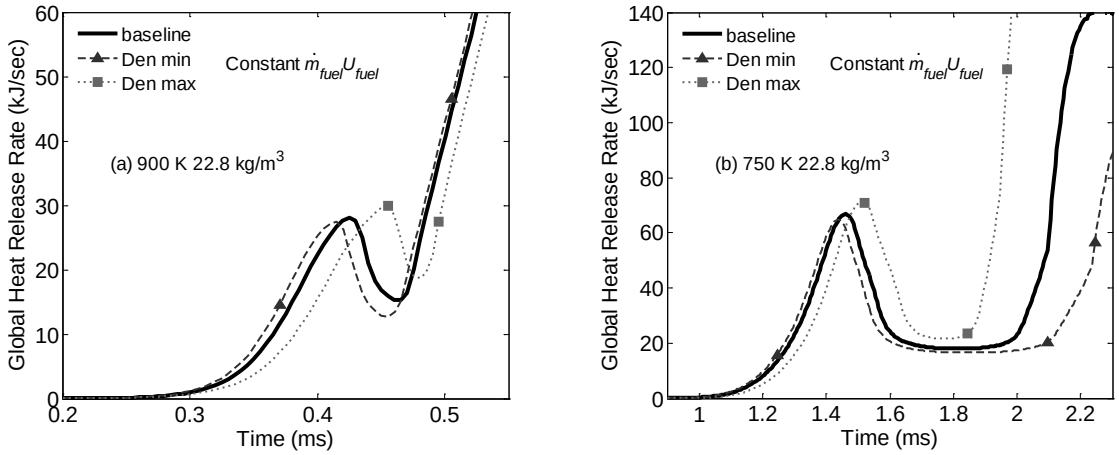

Figure 2.16. Comparisons of the calculated global heat release rates for the density perturbation with constant injection momentum at (a) 900 K 22.8 kg/m^3 and (b) 750 K 22.8 kg/m^3.

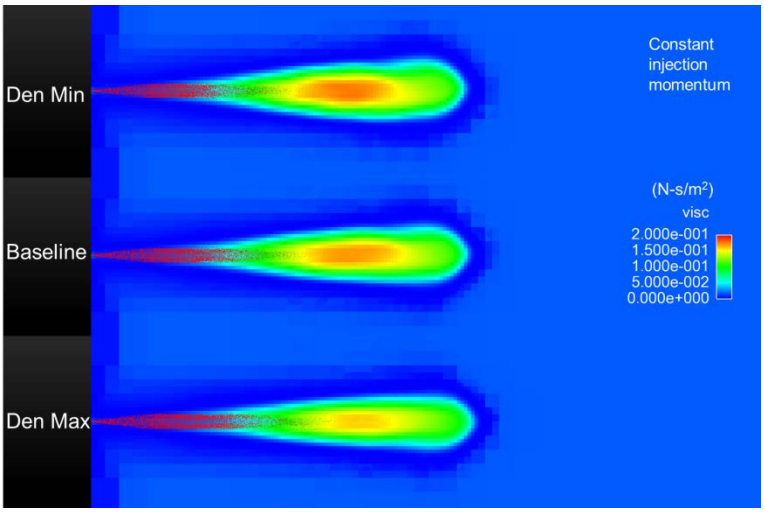

Figure 2.17. Comparisons of turbulent viscosities for the 900 K 22.8 kg/m^3 case at 0.25ms after the start of injection of the density perturbation cases.

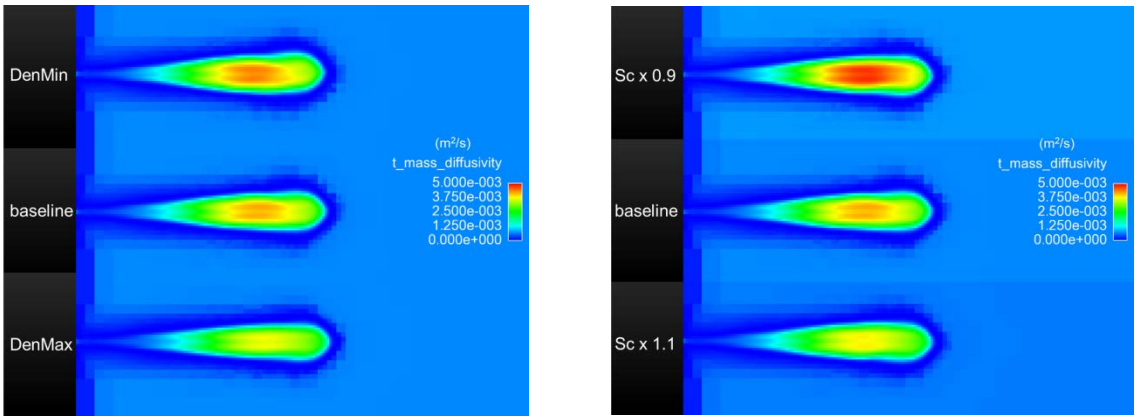

(a) (b)

Figure 2.18. Comparisons of turbulent mass diffusivity for the 900 K 22.8 kg/m^3 case at 0.25ms after the start of injection of (a) density perturbation cases with constant injection momentum, and (b) mixing perturbation cases.

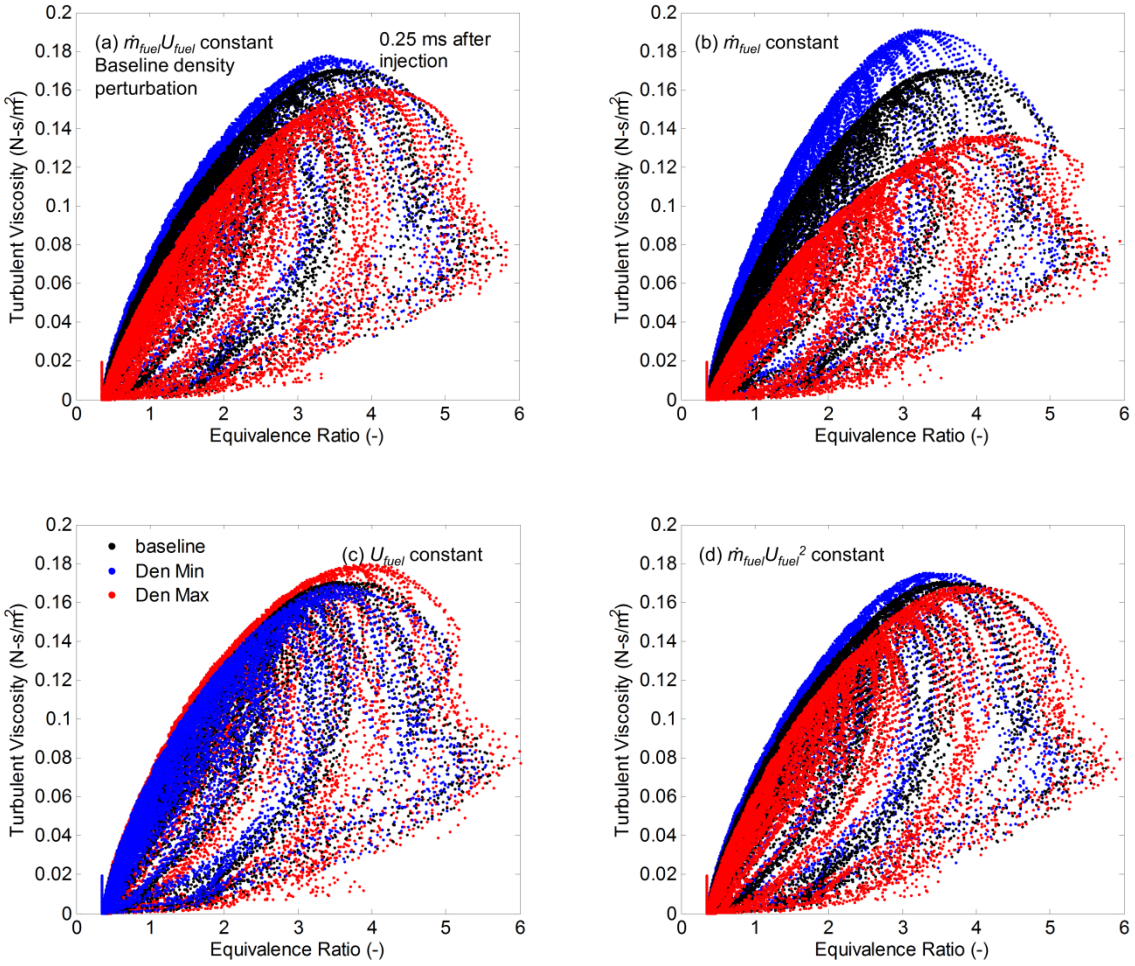

Figure 2.19. Comparisons of turbulent viscosities for the 900 K 22.8 kg/m^3 case at 0.25ms after the start of injection from different density perturbation methods. In (a) the momentum flow rate is held constant, (b) the mass injection rate is held constant, (c) the injection velocity is held constant, and (d) the kinetic energy flow rate from injection is held constant.

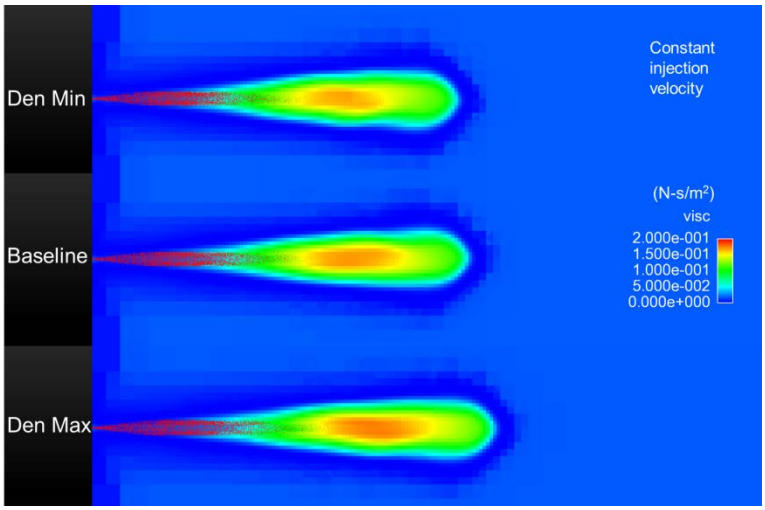

Figure 2.20. Comparisons of turbulent viscosities for the 900 K 22.8 kg/m^3 case at 0.25ms after the start of injection of the density perturbation with constant injection velocity.

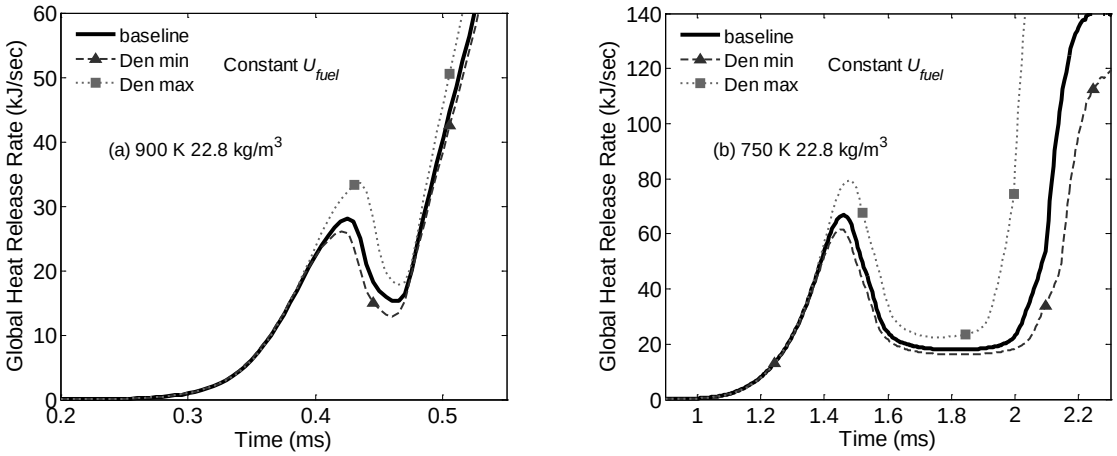

Figure 2.21. Comparisons of the calculated global heat release rates for the density perturbation with constant injection velocity at (a) 900 K 22.8 kg/m^3 and (b) 750 K 22.8 kg/m^3.

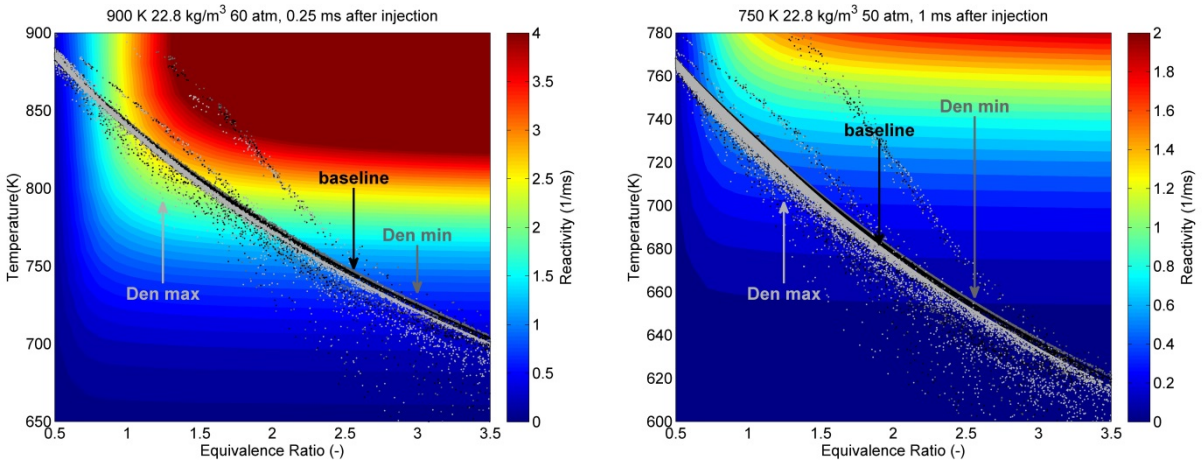

(a) (b)

Figure 2.22. The n-dodecane reactivity contour and temperature-equivalence ratio distribution within the spray before the start of LTHR for the density perturbation with constant injection momentum. (a) 900 K 22.8 kg/m^3 at 0.25 ms after injection with the reactivity contour at 60 atm and (b) 750 K 22.8 kg/m^3 at 1 ms after injection with the reactivity contour at 50 atm.

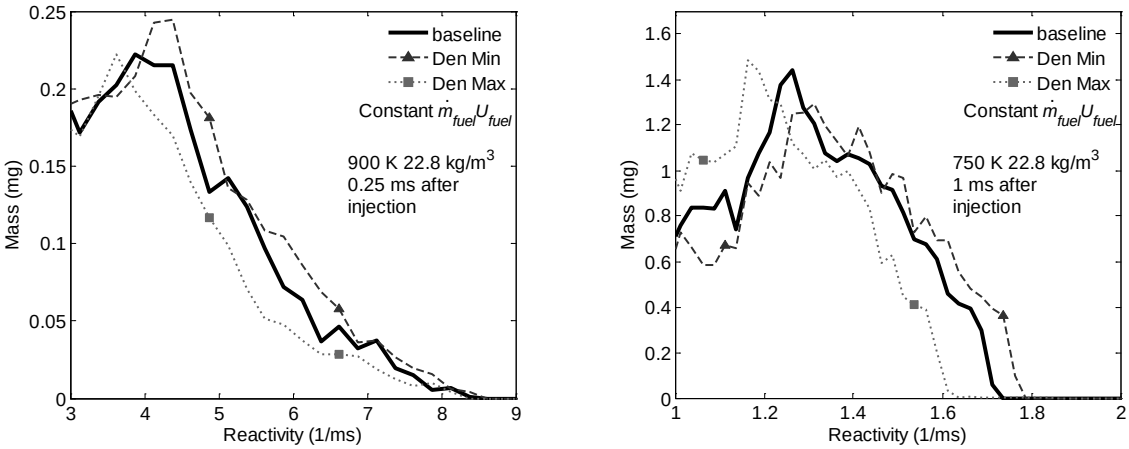

(a) (b)

Figure 2.23. Mixture mass distributions in the local reactivity domain just prior to the start of low temperature heat release for the density perturbation with constant injection momentum for (a) 900 K 22.8 kg/m^3 at 0.25 ms after injection and (b) 750 K 22.8 kg/m^3 at 1 ms after injection. The reactivity bin size is 0.25 and 0.025 1/ms for the 900 K case and the 750 K case, respectively.

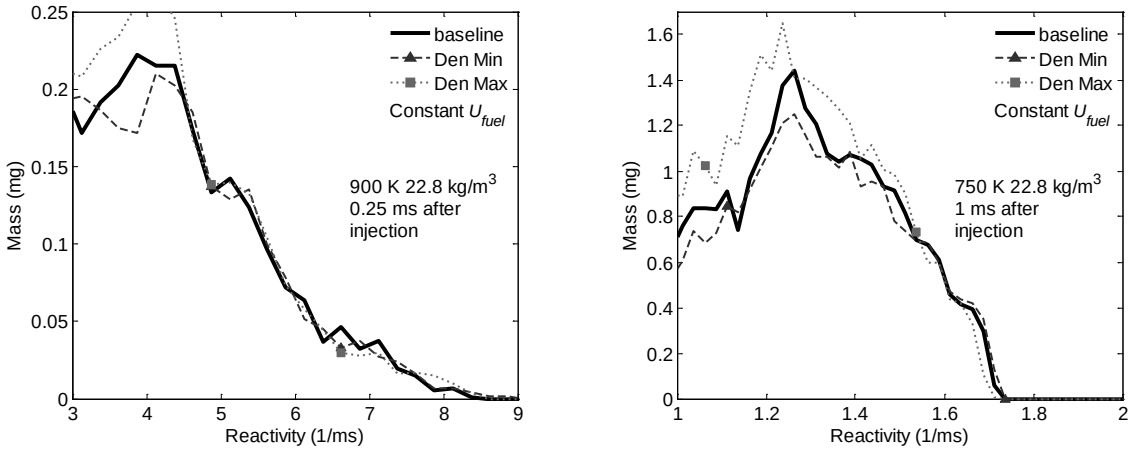

(a) (b)

Figure 2.24. Mixture mass distributions in the local reactivity domain just prior to the start of low temperature heat release for the density perturbation with constant injection velocity for (a) 900 K 22.8 kg/m^3 at 0.25 ms after injection and (b) 750 K 22.8 kg/m^3 at 1 ms after injection. The reactivity bin size is 0.25 and 0.025 1/ms for the 900 K case and the 750 K case, respectively.

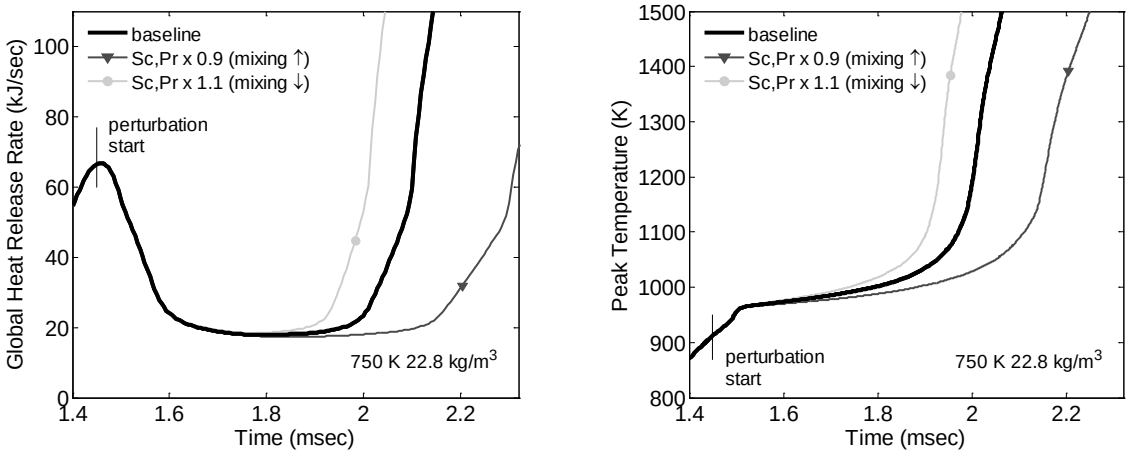

(a) (b)

Figure 2.25. (a) Global heat release rate and (b) peak temperature within the computational domain of the mixing perturbation study during the NTC period at 750 K 22.8 kg/m^3.

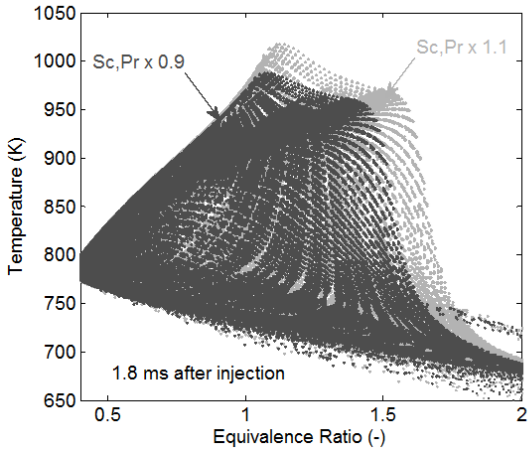

Figure 2.26. Temperature – equivalence ratio distributions at 1.8 ms after start of injection for the mixing perturbation cases in Figure 2.23.

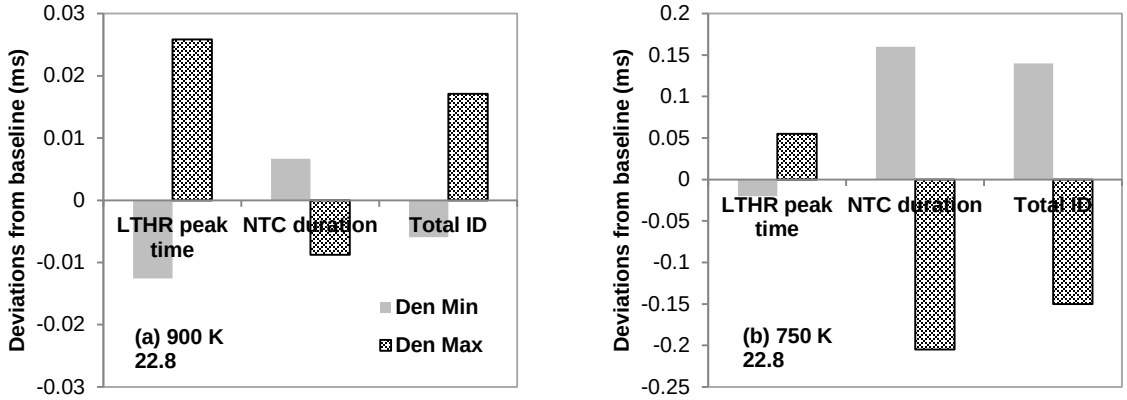

Figure 2.27. Deviations from the baseline in LTHR peak timing, NTC duration, and total ignition delay time for the density perturbation cases at (a) 900 K 22.8 kg/m^3 and (b) 750 K 22.8 kg/m^3. The deviation in total ignition delay time is the sum of the deviations in LTHR peak timing and NTC duration. The contribution from LTHR is greater for the 900 K case, but dominated by the contribution from NTC duration for the 750 K case.

Chapter 3

Surrogate Formulation for Conventional and Alternative Jet Fuels

In this chapter reports the optimization-based surrogate formulation methodology and surrogate formulation results for conventional and alternative jet fuels.

3.1 Target Fuels

Three target fuels were examined in the current work as shown in Table 3.1, including petroleum-derived Jet-A POSF-4658, Iso-Paraffinic Kerosene (IPK) POSF-5642, a coal-derived SPK with very low DCN, and S-8 POSF-4734, a natural-gas-derived SPK with very high DCN. Also, 50/50 vol% blends of Jet-A/IPK and Jet-A/S-8 were considered. The carbon number distributions are similar for the three fuels [81], but their hydrocarbon class compositions and resulting fuel properties differ significantly. While petroleum-derived Jet-A is a complex mixture of linear alkanes, cyclic alkanes, and aromatic compounds [82], IPK and S-8 are composed of entirely linear alkanes (mostly iso-alkanes) except for IPK's small cyclic alkane fraction [81]. Despite their similar and dominant iso-alkane composition, IPK and S-8 have drastically different ignition quality (DCN of 31 vs 60), which stems from the difference in the degree of iso-alkane

branching in these fuels, with IPK having less-ignitable highly-branched iso-alkane species, and S-8 with mostly high ignition quality mono- or di-methyl alkanes [47,83]. The absence of aromatics in SPK's can explain in part the property differences of these fuels compared to petroleum derived Jet-A, which contains up to ~20% aromatics by volume [82]. For instance, due to the aromatic's molecular structure with single or multiple benzene rings, these compounds generally have a lower H/C ratio and a higher liquid density than linear alkanes. These differences result in higher H/C and lower liquid density for SPK's relative to Jet-A. The current surrogate formulation effort seeks to capture the diverse range of compositional and property characteristics present within the target jet fuels.

3.2 Target Property Selection

The surrogate formulation for these target fuels focused on emulating various properties affecting the compression ignited combustion process. As concluded in Chapter 2, four temperature dependent liquid physical properties, which are density, viscosity, volatility, and specific heat, have significant impact on the spray characteristics and its ignition behavior. Also, the chemical processes which prepare the fuel-air charge for ignition depend on the chemical properties of the fuel. The ignitability of the fuel, often represented by DCN for diesel application determines the reactivity of the fuel. The MW affects the liquid/vapor phase diffusive transport of fuel species, while the LHV determines the energy that can be released through the oxidation of the fuel. Finally, the local air/fuel ratio and adiabatic flame temperature are influenced by the H/C ratio.

In order to properly address the dependency of the diesel ignition processes on various liquid fuel properties, eight properties were chosen as the target properties for the surrogates, which are DCN, LHV, H/C ratio, MW, density, viscosity, specific heat, and distillation curve as summarized in Table 3.1

3.3 Surrogate Component Palette

Since the properties of surrogate mixtures depend on the properties of the surrogate components, appropriate surrogate component selection is critical for successful property emulation for surrogate fuels. The surrogate components were selected based upon the following considerations:

1. The relevance to the hydrocarbon molecules in real jet fuels in terms of hydrocarbon class and molecular size.
2. The existence of chemical mechanism that is capable of predicting the ignition process of the neat components.
3. Previous use in other jet fuel surrogate studies or use that has been suggested in the literature [24].

Based upon these criteria, a palette of six pure components is formed which is n-dodecane/n-decane/iso-cetane/iso-octane/decalin/toluene. Note that decalin (CAS 91-17-8) used throughout this study is approximately a 60/40 vol% mixture of trans- and cis-isomers. By sharing a common palette, the oxidation of any surrogates formulated within the palette can be simulated with a common chemical mechanism, which is an important benefit considering the application of these surrogates and their blends to a range of target fuels. It should be noted that based on the composition of IPK in [81] and its low

ignition quality, it is ideal to represent the IPK's iso-alkane components with highly-branched iso-alkane molecules in the C10~C12 range, not with iso-octane (C8) and iso-cetane (C16). However, chemical mechanisms for those C10~C12 highly-branched iso-alkanes are not currently available. Thus, any progress in kinetic modeling of highly-branched iso-alkanes between iso-octane and iso-cetane will benefit future surrogate development for SPKs.

3.4 Surrogate Optimizer

An optimizer was developed and utilized to determine the surrogate composition of targeted jet fuels. The optimization process starts with an initial guess for the composition of a model mixture. Based upon the properties of the individual surrogate components, the optimizer calculates or estimates the chemical and physical properties of the model mixture using models and correlations included in the optimizer. Then, the properties of the model mixture are compared against the properties of the target fuel. The deviation between the model mixture and the target fuel defines the objective function of the optimization problem. The optimization algorithm determines the composition of the next model mixture. This process is automatically iterated until the composition of the surrogate components with the best match to the target fuel properties is found.

Table 3.2 summarizes the models that were used in the optimizer for estimating the mixture properties. Note that a model is not required for calculating the mixture MW and H/C ratio. The LHV of the mixture was calculated with a mass fraction average of the individual LHV's of each surrogate component. The density of the mixture was

estimated with the volume fraction average. The viscosity of the mixture was estimated using the Grunberg-Nissan equation [84] with the regression term Gij set to zero, which is applicable to hydrocarbon mixtures as suggested in [85] with expected errors of about 15 percent. The parachor correlation [86] was used to estimate the mixture surface tension, neglecting the vapor mixture molar density which is very small compared to the liquid mixture molar density. The uncertainty of the parachor correlation is 3 ~ 10 percent according to [85].

3.4.1 Regression Equation Development for Mixture DCN Estimation

Initially, the DCN of the model mixture was estimated by taking a linear average of the pure components' DCNs based upon their respective volume fraction. While this linear method has been widely used in other optimization-based surrogate development studies [30,31], it cannot capture non-linear blend effects influencing mixture DCN. In particular, it has been reported that the non-linear effect is significant when n-alkane is blended with low ignition quality iso-alkane; the increase in DCN resulting from n-alkane addition is much greater than the linear effect [29,87]. To properly incorporate this non-linearity into the optimization process, a non-linear regression equation correlating the mixture composition to DCN was implemented in the surrogate optimizer. For the formulation of the regression equation and the design of experiments, the simplex-lattice design of Scheffé [87,88] was utilized with a 36-term polynomial to capture the linear and non-linear blending effects among six surrogate components:

$$DCN = \sum_{i=1}^{6} \beta_i x_i + \sum_{i=1}^{5} \sum_{j=i+1}^{6} \beta_{i,j} x_i x_j + \sum_{i=1}^{5} \sum_{j=i+1}^{6} \delta_{i,j} x_i x_j (x_i - x_j) \qquad \text{(Eq. 8)}$$

where x_i is the volume fraction of the ith surrogate component and β_i, $\beta_{i,j}$, and $\delta_{i,j}$ are the coefficients of the regression equation. It includes a linear average term ($\sum_{i=1}^{6} \beta_i x_i$) along with second ($\sum_{i=1}^{5} \sum_{j=i+1}^{6} \beta_{i,j} x_i x_j$) and third order ($\sum_{i=1}^{5} \sum_{j=i+1}^{6} \delta_{i,j} x_i x_j (x_i - x_j)$) binary interaction terms.

This regression equation was fit to DCN measurements of 76 surrogate component mixtures covering a range of DCN from 13 ~ 74 obtained from new IQT experiments. The IQT experiments were performed by Professor Marcis Jansons' group at Wayne State University. The full data matrix is provided Table 3.3. These 76 data include points for the regression equation, along with the DCN of the target fuels and the final surrogate mixtures used for model confirmation. Details on the experimental setup and its standard operating procedure are found in [89]. The data matrix started from the simplex-lattice design for second order mixtures (pure components and 50/50 binary mixtures) of the 6 components. The data matrix was then expanded to include 13 additional binary mixtures (n-dodecane/iso-octane or iso-cetane or toluene) and 46 mixtures (tertiary, 4-, 5-, and 6-component mixtures) to improve the reliability of the regression model.

The polynomial regression coefficients were determined with the method of least squares and are compared against the previous linear average method in Figure 3.1. The coefficients of the regression equation are summarized Table 3.4. The regression equation fits well to the experimental data as indicated by the R^2 of 0.998 and with an

average absolute error of 1.36 % and a maximum absolute error of 1.8 DCN. Figure 3.1 also clearly shows that the regression equation predictions are much more accurate than those from the linear average method; the average and the maximum absolute error from the linear average method were 10.4 % and 11.3 DCN, respectively. This regression equation was utilized to estimate the surrogate mixture DCN during the optimization process.

3.4.2 Model for Distillation Curve Estimation

The distillation curve of the mixture was estimated by calculating the temperature of the bubble point. The procedure of mixture distillation was modeled, by assuming that a constant volume of liquid mixture leaves the liquid phase into vapor phase at each volume step, which is similar to the approach shown in Huber et al. [47]. The volume of the liquid mixture is initially set to be 100, which decreases by 1 every volume step. At the first volume step, the bubble point of the liquid mixture and the composition of resulting equilibrium vapor phase is calculated by solving liquid-vapor equilibrium equations with Raoult's law as shown in Table 3.2. Considering the amount and the composition of the vapor that left the liquid phase, the composition of the liquid phase for the next volume step is derived. This process is repeated until all the liquid has evaporated into the vapor phase. The calculated distillation curve was shifted for validation against experimental data from the Advanced Distillation Curve metrology as suggested by Huber et al. [47] to account for the time it takes for the vaporized fluid to reach the collecting vessel after evaporation at the surface of the liquid mixture. The model was validated against the experimental distillation curve of 75/25 and 50/50

mixtures of n-decane and n-tetradecane [47,90] and the measured distillation curves of surrogates in Bruno and Smith [91]. As shown in Figure 3.2, the calculated distillation curves were able to successfully capture the experimental trend from the Advanced Distillation Curve metrology. In Figure 3.3, the distillation curves of 9 surrogate mixtures in [91] were also estimated and the agreement with the measured data was very good showing the average absolute deviation from the measured data being less than 2% for all 9 surrogates. Solving the vapor-liquid equilibrium at the vaporizing surface with the rather simple Raoult's law, which neglects transport effects, is thought to be the main reason for the discrepancies between the experiments and the predictions.

3.4.3 Objective Function

The objective function of the optimization problem was defined as the weighted sum of the squared relative difference between the experimental data and the estimated values, which is expressed with the following equations.

$$ObjFunc = \sum_{i=1}^{N_{target}} w_i E_i \qquad \text{(Eq. 9)}$$

$$E_i = \frac{\sum_{j=1}^{N_{data,i}} \left(\frac{x_{i,j,calc} - x_{i,j,\exp}}{x_{i,j,\exp}} \right)^2}{N_{data,i}} \qquad \text{(Eq. 10)}$$

where i is the index for target properties, j is the index for experimental data points, $x_{i,j,calc}$ is calculated/estimated model mixture property, $x_{i,j,exp}$ is the experimental data of the target fuel, N_{target} is the number of total target properties, $N_{data,i}$ is the number of total experimental data points for the target property i, and w_i is weight for the target property i.

The weight assigned to each target property within the objective function, as shown in Table 3.1, was determined to emphasize certain properties. DCN, density, and specific heat were given higher weights, since these properties have been shown to be most influential to the spray and combustion characteristics of compression ignition engines [5,92]. The optimization problem was solved with sequential use of the genetic algorithm, a global search method, and the MATLAB function fmincon, a local search method. The genetic algorithm explores the entire search space to find the approximate location of the global minima, at which point the local search method is used to complete the optimization process.

3.5 Formulation Results and Discussions

Table 3.5 summarizes the newly formulated surrogate compositions for Jet-A, IPK, and S-8. These surrogates are each 4-component mixtures that draw from several of the 6 hydrocarbon components within the surrogate palette. In general, the surrogates successfully captured the compositional characteristics of the target fuels. The Jet-A surrogate includes a substantial amount of cyclo-alkane and aromatic compounds, similar to the targeted Jet-A POSF-4658. Also, the small cyclo-alkane content of IPK and the purely paraffinic S-8 is well emulated by the respective surrogates.

Table 3.6 shows a comparison among the temperature-independent target properties (DCN, LHV, H/C, and MW) of the surrogates and the target fuels. The three surrogates successfully emulated all of the targeted temperature-independent properties with a maximum deviation of ~ 4% from MW. Most notably, the measured DCNs of the actual surrogate mixtures agreed well with the DCNs of the target fuels, proving the

effectiveness of the new regression equation. The surrogate mixtures were also able to emulate DCN of Jet-A/SPK blends. Measured DCN of 50/50 vol% blends of Jet-A/IPK surrogates and Jet-A/S-8 surrogates were 40.1 and 52.3, which agreed well with DCN of 40.2 and 53.1 for Jet-A/IPK and Jet-A/S-8 real blends.

The current Jet-A surrogate shows notably different composition when compared to UM2, our initial Jet-A POSF-4658 surrogate [27] that includes identical surrogate components (n-dodcane/iso-cetane/decalin/toluene). For the formulation of UM2, the linear average method for mixture DCN was used, while the components' DCNs are from the literature [27]. The DCN of the actual UM2 mixture was measured at 40.6, which is significantly lower than the targeted DCN of 47.3. Besides the uncertainty from the linear average method, the uncertainty in pure component CNs reported in the literature was another reason for the large DCN deviations of UM2. In particular, the decalin CN of 46.5 [93] used in our previous optimizer [27] is originally from a measurement dating back to 1930s which used a different experimental method (Cetene number measurement) [93] from the currently used ASTM D6890 method. Our measured decalin (~60/40vol% trans/cis) DCN was 32.9, which agrees better with others' recent measurements [94,95]. Such a large error in the decalin CN resulted in much lower measured DCN for UM2 relative to the optimizer prediction. For the current study, where a DCN regression equation generated by a single IQT machine was utilized [96], the device-to-device uncertainty in the pure-component DCN's from the literature was eliminated, resulting in significantly better ignition quality emulation for the new Jet-A surrogate.

Figure 3.4 shows the temperature-dependent liquid fuel density, viscosity, and specific heat of the surrogate and target fuels. Target fuel density and viscosity were well

matched by all three surrogates, with average absolute deviations of less than 1 %. For specific heat, the Jet-A and IPK surrogates displayed 2.5 % average absolute deviations from their target fuels, while the S-8 surrogate was within 5.6 %. These variations are well within the variability of specific heat measurements of the targeted fuels [97,98], which displayed up to 20 % measurement-to-measurement variance. The densities of 50/50 vol% surrogate blends were also well-matched to the real blends: at 313 K, the surrogate blends of Jet-A/IPK and Jet-A/S-8 were 762.3 kg/m^3 and 757.0 kg/m^3, while the corresponding real blends were 766 kg/m^3 and 761 kg/m^3.

Figure 3.5 compares the calculated distillation curves of the surrogate fuels and the corresponding target fuels measured by the NIST's Advanced Distillation Curve metrology [83,99,100]. As seen in Figure 3.5 (a) and (c), the Jet-A and S-8 surrogates successfully emulate the volatility of the target fuels as well as the overall shape of the distillation curve. This indicates that not only the molecular size of the surrogate components but also that their vapor pressure distribution was appropriate for the Jet-A and S-8 surrogates. It is important for simple surrogate mixtures to have well-distributed vapor pressures among the surrogate components to avoid drastic curvature in the distillation curve [27]. On the other hand, Figure 3.5 (b) shows that the calculated distillation curve of the IPK surrogate only captures the mean volatility of the fuel and that the shape of the distillation curve is not well emulated. As previously discussed, IPK is comprised of ~ 90 % of iso-alkane molecules, which are mostly C10~C14. As there is a correlation between the molecular weight and volatility in general, the vapor pressure of iso-octane is too high and that of iso-cetane is too low to represent the volatility of the C10~C14 iso-alkanes in the target IPK. Such a large difference in volatility between iso-

octane and iso-cetane is observed when the composition of the evaporated mixture leaving the liquid phase during the distillation process is monitored as shown in Figure 3.6. The evaporating composition of the IPK surrogate until ~ 30 % distilled volume is more than 90 % iso-octane, which is significantly more volatile than other surrogate components. The majority of iso-cetane starts to vaporize only after ~ 40 % distilled volume is reached. Such a discrete distillation characteristics are not observed for the real target fuels including IPK. Thus, emulating the distillation characteristics of these iso-alkanes with iso-octane (C8) and iso-cetane (C16) in the surrogate palette is fundamentally a challenging task. A new highly-branched iso-alkane surrogate component in the range of C10~C12 is therefore required for better IPK distillation curve emulation.

3.6 Summary and Conclusions

The surrogate optimizer was developed and utilized to formulate surrogates for various types of jet fuels, including conventional petroleum-derived and SPK jet fuels. A six-component surrogate palette was proposed that is capable of capturing a wide range of property variations within conventional and alternative jet fuels. For the optimizer, a DCN regression equation was developed, which generated more accurate mixture DCN prediction compared to the previously used volume fraction average method. In addition, a distillation curve model was implemented within the optimizer to estimate the distillation characteristics of the surrogate mixture. The newly formulated surrogates for Jet-A, IPK, and S-8 successfully emulate the various chemical and physical properties known to affect liquid spray phenomena and the chemical ignition behavior within the

diesel combustion process. The successful formulation results show that the surrogate framework, which is composed of the six component surrogate palette and the surrogate optimizer, is an effective tool to develop surrogates for various types of jet fuels.

Tables

Table 3.1. Measured target properties and their weights assigned for the optimization process. DCN measurements are from IQT experiments.

Target properties	Jet-A POSF-4658	IPK POSF-5642	S-8 POSF-4734	Weight
DCN (IQT)	47.3	30.7	60.36	10
LHV (MJ/kg)	42.8 [101]	44.0 [101]	44.1 [101]	1
H/C	1.957 [101]	2.119 [101]	2.152 [101]	1
MW	142 [101]	156 [101]	168 [101]	1
Density	[98]	[97]	[102]	25
Viscosity	[98]	[97]	[103]	1
Specific heat capacity	[97]	[97]	[98]	5
Distillation curve	[100]	[83]	[99]	5

Table 3.2. Mixture property estimation methods used in the surrogate optimizer.

Target property	Estimation method	Reference
CN	**36 term regression equation** $DCN = \sum_{i=1}^{6} \beta_i x_i + \sum_{i=1}^{5} \sum_{j=i+1}^{6} \beta_{i,j} x_i x_j + \sum_{i=1}^{5} \sum_{j=i+1}^{6} \delta_{i,j} x_i x_j (x_i - x_j)$	[96]
LHV	**Mass fraction average** $LHV_{mix} = \sum y_i LHV_i$	
Density	**Volume fraction average** $\rho(T)_{mix} = \sum \upsilon(T)_i \rho(T)_i$ Where ρ(T) = liquid density	
Viscosity	**Grunberg-Nissan equation** $\ln(\eta(T)_{mix}) = \sum x_i \ln(\eta(T))_i + 0.5 \sum \sum x_i x_j G_{ij}$ Where η(T) = liquid viscosity, G_{ij} = binary interaction parameter	[84]
Distillation curve	**Bubble point calculation with Raoult's Law** $\sum x_{vapor,i} = 1 = \sum \frac{p(T)_{vap,i}}{p_{tot}} x_{liquid,i}$, $x_{vapor,i} = \frac{p(T)_{vap,i}}{p_{tot}} x_{liquid,i}$ Where $p(T)_{vap}$ = vapor pressure, p_{tot} = ambient pressure	

υ_i=volume fraction of component i, y_i=mass fraction of component i, x_i=mole fraction of component i, T=liquid temperature

Table 3.3. Data matrix that were used for DCN regression equation.

#	n-dodecane	n-decane	iso-cetane	iso-octane	decalin	toluene	DCN	
							Measured	Estimated
1	1	0	0	0	0	0	74.2	75.3
2	0	1	0	0	0	0	67.8	67.6
3	0	0	1	0	0	0	12.0	13.8
4	0	0	0	1	0	0	15.4	15.9
5	0	0	0	0	1	0	32.9	32.9
6	0.5	0.5	0	0	0	0	70.7	71.1
7	0.5	0	0.5	0	0	0	51.2	51.4
8	0.5	0	0	0.5	0	0	53.9	55.4
9	0.5	0	0	0	0.5	0	48.4	48.1
10	0.5	0	0	0	0	0.5	44.7	45.8
11	0	0.5	0.5	0	0	0	48.3	47.2
12	0	0.5	0	0.5	0	0	49.6	49.6
13	0	0.5	0	0	0.5	0	45.7	46.5
14	0	0.5	0	0	0	0.5	39.5	39.5
15	0	0	0.5	0	0.5	0	25.8	24.7
16	0	0	0	0.5	0.5	0	26.5	26.6
17	0	0	0	0	0.5	0.5	22.9	22.9
18	0.75	0	0.25	0	0	0	64.4	62.5
19	0.75	0	0	0.25	0	0	66.5	65.4
20	0.75	0	0	0	0	0.25	62.4	62.1
21	0.25	0	0.75	0	0	0	37.6	36.8
22	0.25	0	0	0.75	0	0	41.3	40.5
23	0.25	0	0	0	0	0.75	24.2	24.1
24	0.15	0	0.85	0	0	0	29.4	28.9
25	0.15	0	0	0.85	0	0	32.0	32.1
26	0.15	0	0	0	0	0.85	13.6	13.4
27	0.1	0	0.9	0	0	0	25.4	24.4
28	0.1	0	0	0.9	0	0	27.4	27.2
29	0.05	0	0.95	0	0	0	19.8	19.3
30	0.05	0	0	0.95	0	0	22.2	21.8
31	0.5	0.1	0.1	0.1	0.1	0.1	53.2	53.8
32	0.1	0.5	0.1	0.1	0.1	0.1	49.9	49.7
33	0.1	0.1	0.5	0.1	0.1	0.1	31.1	31.6
34	0.1	0.1	0.1	0.5	0.1	0.1	33.6	33.5
35	0.1	0.1	0.1	0.1	0.5	0.1	34.8	34.5
36	0.1	0.1	0.1	0.1	0.1	0.5	26.4	26.3
37	0.167	0.167	0.167	0.167	0.167	0.167	39.3	39.3
38	0.1	0.8	0.1	0	0	0	63.8	64.5

39	0.2	0.6	0.2	0	0	0	62.0	61.8
40	0.1	0	0.1	0.8	0	0	27.3	27.5
41	0.2	0	0.2	0.6	0	0	36.2	36.1
42	0.1	0	0.1	0	0.8	0	34.5	34.9
43	0.2	0	0.2	0	0.6	0	37.1	37.2
44	0.1	0	0.1	0	0	0.8	10.6	10.9
45	0.2	0	0.2	0	0	0.6	22.7	23.6
46	0.3	0	0.3	0	0	0.4	33.7	33.9
47	0.4	0	0.4	0	0	0.2	43.1	42.8
48	0.45	0	0.45	0	0	0.1	47.2	47.0
49	0.3	0.4	0.3	0	0	0	58.1	59.0
50	0.4	0.2	0.4	0	0	0	54.8	55.7
51	0.45	0.1	0.45	0	0	0	52.8	53.7
52	0.3	0	0.3	0.4	0	0	42.2	42.3
53	0.4	0	0.4	0.2	0	0	47.4	47.2
54	0.45	0	0.45	0.1	0	0	49.5	49.3
55	0.3	0	0.3	0	0.4	0	39.7	40.3
56	0.4	0	0.4	0	0.2	0	43.6	44.8
57	0.45	0	0.45	0	0.1	0	47.1	47.8
58	0.45	0.45	0	0	0.1	0	65.9	65.3
59	0.4	0.4	0	0	0.2	0	61.2	60.2
60	0.3	0.3	0	0	0.4	0	52.1	51.4
61	0.2	0.2	0	0	0.6	0	44.5	44.3
62	0.1	0.1	0	0	0.8	0	38.5	38.3
63	0.28	0	0.12	0	0	0.6	30.9	29.6
64	0.42	0	0.18	0	0	0.4	42.5	41.8
65	0.56	0	0.24	0	0	0.2	51.7	51.8
66	0.63	0	0.27	0	0	0.1	56.3	56.2
67	0.4545	0	0.1425	0	0.2673	0.1357	46.2	46.2
68	0.3888	0.0671	0.1408	0	0.2815	0.1218	45.8	45.7
69	0.1505	0	0.3222	0.3922	0.1352	0	31.6	31.3
70	0.2332	0.4599	0.2683	0.0386	0	0	58.2	58.7
71	0.2349	0.2027	0.1218	0.0169	0.3391	0.0846	43.5	44.2
72	0.4658	0.2899	0.1823	0.062	0	0	61.3	61.5
73	0.1134	0.1969	0.3658	0	0.1881	0.1357	37.5	37.6
74	0.44425	0.14495	0.15795	0.031	0.15305	0.0688	52.7	52.6
75	0.3287	0.429	0.2177	0.0245	0	0	62.2	61.4
76	0.3027	0.4097	0.2432	0.0443	0	0	59.9	59.9

Table 3.4. Coefficients of DCN regression equation.

coefficients		Value
β_1	x_1	75.31
β_2	x_2	67.59
β_3	x_3	13.82
β_4	x_4	15.90
β_5	x_5	32.86
β_6	x_6	-5.39
β_{12}	$x_1 x_2$	-1.37
β_{13}	$x_1 x_3$	27.25
β_{14}	$x_1 x_4$	39.06
β_{15}	$x_1 x_5$	-23.93
β_{16}	$x_1 x_6$	43.54
β_{23}	$x_2 x_3$	25.87
β_{24}	$x_2 x_4$	31.25
β_{25}	$x_2 x_5$	-15.04
β_{26}	$x_2 x_6$	33.58
β_{34}	$x_3 x_4$	15.20
β_{35}	$x_3 x_5$	5.25
β_{36}	$x_3 x_6$	10.36
β_{45}	$x_4 x_5$	8.74
β_{46}	$x_4 x_6$	-26.69
β_{56}	$x_5 x_6$	36.61
δ_{12}	$x_1 x_2 (x_1 - x_2)$	-37.29
δ_{13}	$x_1 x_3 (x_1 - x_3)$	-26.84
δ_{14}	$x_1 x_4 (x_1 - x_4)$	-25.34
δ_{15}	$x_1 x_5 (x_1 - x_5)$	11.91
δ_{16}	$x_1 x_6 (x_1 - x_6)$	-12.62
δ_{23}	$x_2 x_3 (x_2 - x_3)$	-50.03
δ_{24}	$x_2 x_4 (x_2 - x_4)$	29.59
δ_{25}	$x_2 x_5 (x_2 - x_5)$	-26.91
δ_{26}	$x_2 x_6 (x_2 - x_6)$	-109.79
δ_{34}	$x_3 x_4 (x_3 - x_4)$	2.36
δ_{35}	$x_3 x_5 (x_3 - x_5)$	-29.06
δ_{36}	$x_3 x_6 (x_3 - x_6)$	-17.52
δ_{45}	$x_4 x_5 (x_4 - x_5)$	-88.38
δ_{46}	$x_4 x_6 (x_4 - x_6)$	211.76
δ_{56}	$x_5 x_6 (x_5 - x_6)$	-194.83
1=n-dodecane, 2=n-decane. 3=iso-cetane, 4=iso-octane, 5=decalin, 6=toluene		

Table 3.5. Compositions of optimized surrogate fuels in volume fractions.

	UM2 [27]	Jet-A	IPK	S-8
n-dodecane	0.3577	0.4784	0.1416	0.3073
n-decane	0	0	0	0.4234
iso-cetane	0.2234	0.1129	0.3141	0.2309
iso-octane	0	0	0.4016	0.0384
decalin	0.2753	0.2821	0.1427	0
toluene	0.1436	0.1266	0	0

Table 3.6. Temperature-independent properties of the target fuels and their surrogates.

	Jet-A POSF-4658		IPK POSF-5642		S-8 POSF-4734	
	Target	Surrogate	Target	Surrogate	Target	Surrogate
DCN	47.3	47.3/47.8[a]	30.7	30.7/31.9[a]	60.4	60.5/61.1[a]
LHV (MJ/kg)	42.8	43.34	44.0	44.21	44.1	44.42
H/C	1.957	1.900	2.119	2.121	2.152	2.173
MW (g/mol)	142	146.8	156	149.6	168	163.9

[a] predicted / measured by IQT

Figures

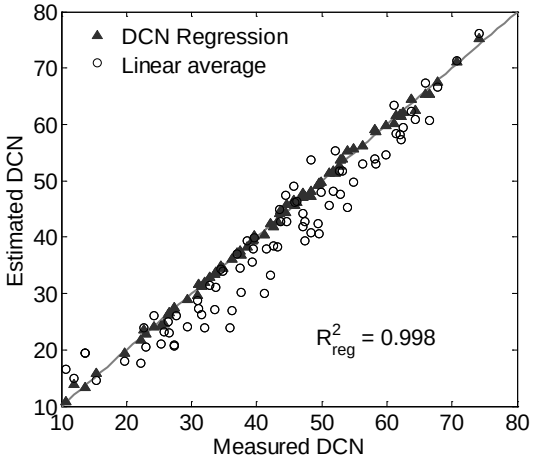

Figure 3.1. DCN estimations using the regression equation and the linear average method. R^2_{reg} is from the DCN regression fitting.

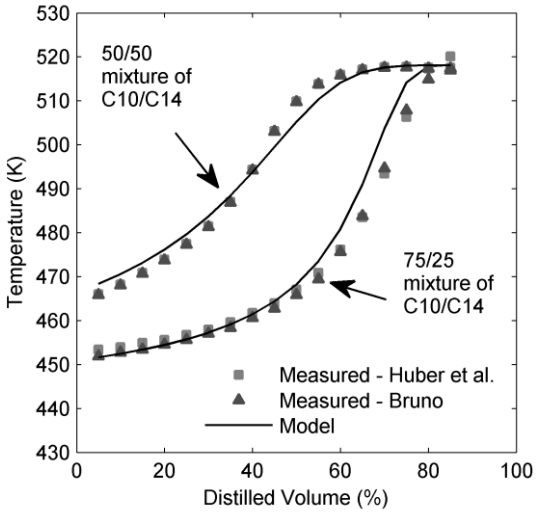

Figure 3.2. Experimental and calculated distillation curves for 75/25 and 50/50 mole fraction mixtures of n-decane and n-tetradecane. The experimental data is from Huber et al. [47] and Bruno [90].

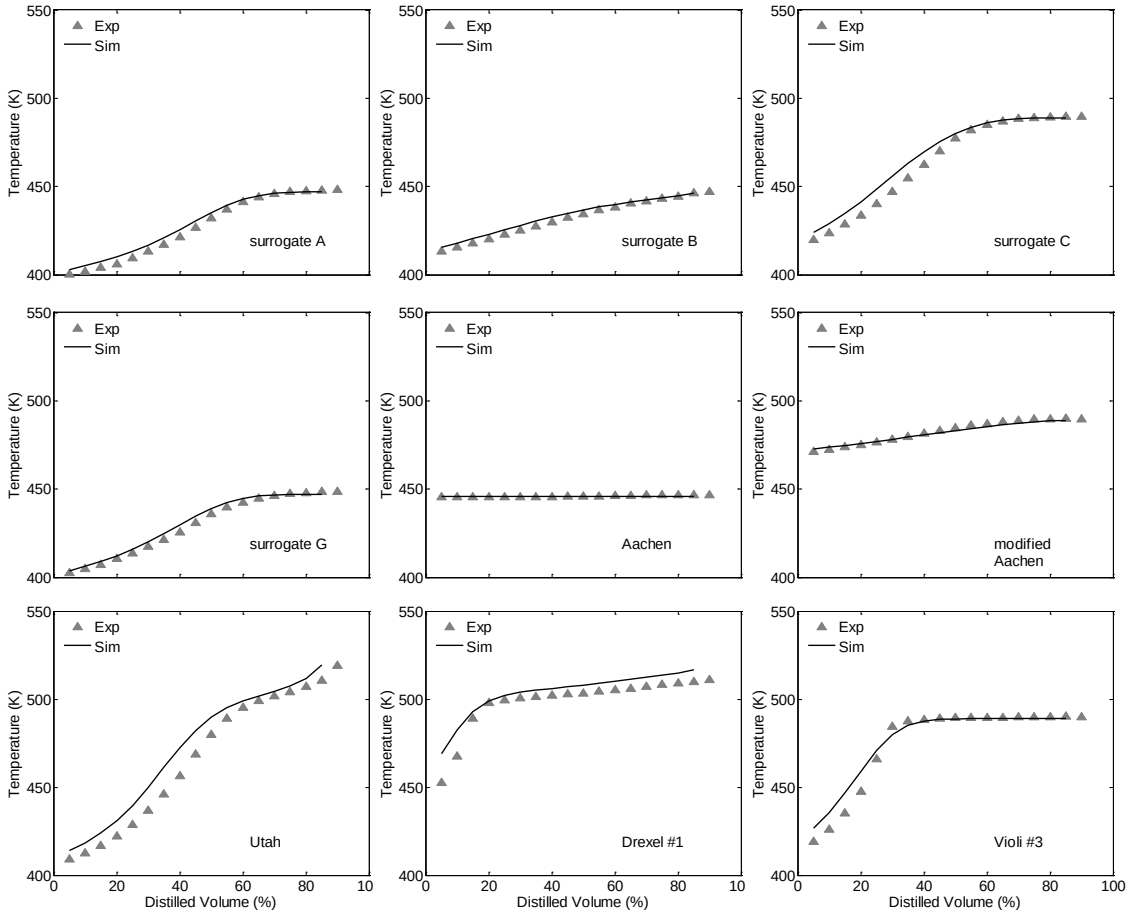

Figure 3.3. Experimental and calculated distillation curves for 9 surrogate mixtures in [91].

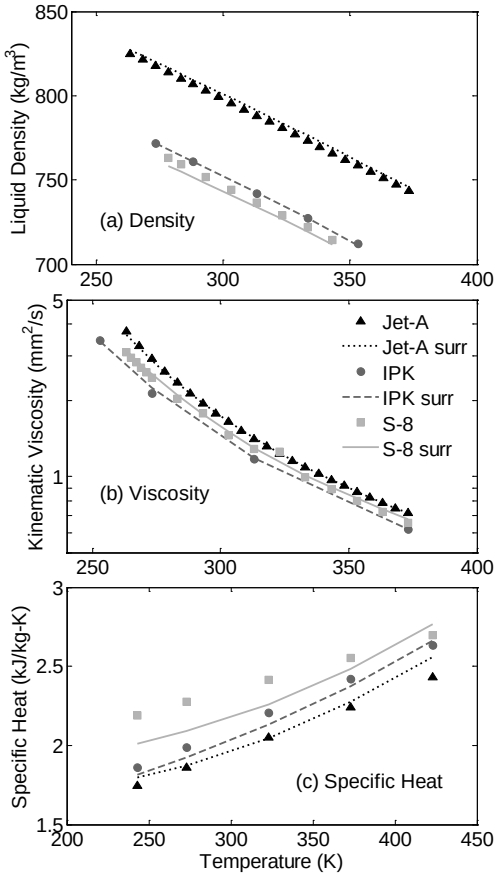

Figure 3.4. Temperature-dependent (a) density, (b) viscosity, and (c) specific heat of the surrogates compared with measured target fuel properties.

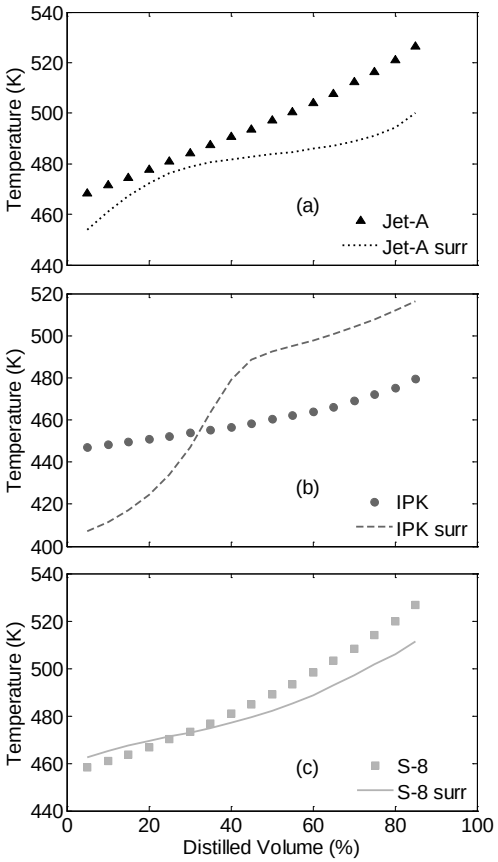

Figure 3.5. Calculated distillation curves of surrogates for (a) Jet-A, (b) IPK, and (c) S-8 compared with the measured distillation curves of the respective target fuels.

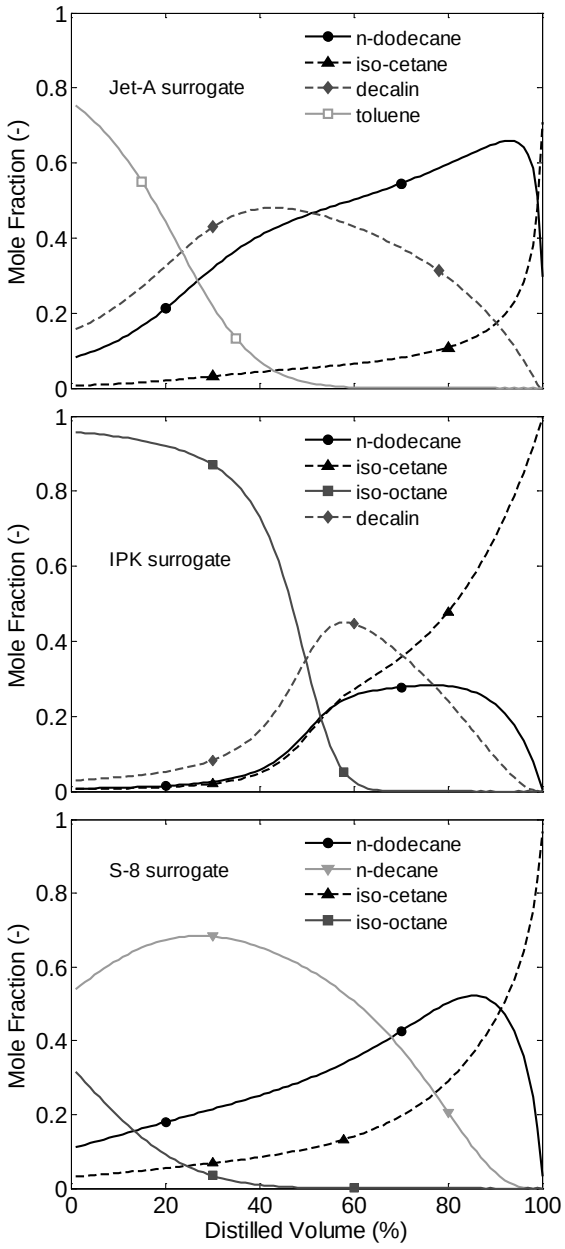

Figure 3.6. Calculated evaporating composition of Jet-A, IPK, and S-8 surrogates during the distillation process.

Chapter 4

Kinetic Modeling for the Surrogate Palette and Mechanism Reduction for CFD Applications

One of the common approaches for modeling the oxidation process of hydrocarbon fuels within CFD simulations is using a kinetic mechanism. The mechanism includes the elementary reactions and their reaction rate parameters involved in the oxidation process. In spite of their complexity and high computational expense, chemical mechanism enables more physics-based high fidelity combustion modeling when compared to simpler phenomenological models. In this chapter, the kinetic modeling of the developed surrogates using a detailed kinetic mechanism is presented. In addition, a skeletal version of the detailed mechanism is derived for the use in CFD.

4.1 Ignition Delay Calculation with a Detailed Kinetic Mechanism

Gas phase ignition delays of the developed surrogates were calculated with CHEMKIN's constant volume homogeneous reactor model [104] and a detailed chemical mechanism from the Model Fuel Consortium (MFC) [105]. This comprehensive detailed mechanism includes low and high temperature oxidation pathways for all of the

hydrocarbon species within the proposed six-component surrogate palette, containing 4236 species and 18000 reactions. The modular structure of the detailed mechanism is illustrated in Figure 4.1. The mechanism is composed of four submechanisms for each hydrocarbon class (n-alkane, iso-alkane, cycloalkanes, and aromatics), which share a common core mechanism for the kinetics of C0~C4 system. The construction of reaction pathways for n-, iso-, and cyclo-alkanes in this mechanism followed the approach originally suggested by Curran et al. [106] as illustrated in Figure 4.2. It is an updated version of the one used in [27]. The most notable change from the previous mechanism is the iso-cetane chemistry, which provides significantly improved agreement for pure iso-cetane ignition delay predictions versus shock tube measurements. The ignition delay calculations were compared to available ignition delay measurements for the target Jet-A, IPK and S-8 fuels from shock tubes [40,107] and a rapid compression machine [28]. The uncertainty in the ignition delay measurements is reported to be in the range of ±10 ~ 25% [28,40,107].

Figure 4.3 compares the calculated and experimental ignition delays of Jet-A/air mixtures. For the 20 atm cases in Figure 4.3 (a), the Jet-A surrogate with the MFC mechanism successfully captures the overall ignition delay trend of the target POSF-4658 in all of the temperature range investigated. Calculated ignition delay times for the stoichiometric mixture agree very well with the experimental measurements in the high temperature and Negative Temperature Coefficient (NTC) regime (T > 750 K), while a longer ignition delay time is predicted in the low temperature regime (T < 750 K). For the slightly rich mixture (Φ = 1.5), the agreement with the experimental data is also very good in the high temperature regime (T > 950 K), however shorter ignition delays are

predicted within the NTC regime, and longer ignition delays are predicted at low temperatures. For the stoichiometric 40 atm case shown in Figure 4.3 (b), good agreement is observed at high temperatures, but the calculated NTC ignition delay times are considerably shorter than the experiments, by up to a factor of 3.

One of the primary reasons for the shorter NTC regime ignition delays of the Jet-A surrogate at 40 atm is the MFC mechanism's n-dodecane chemistry. Figure 4.4 shows ignition delay predictions of Jet-A surrogate components, compared against shock tube measurements [108–111] at 40 atm for n-dodecane and iso-cetane, and at 50 atm for decalin and toluene. Most notably, the predicted NTC regime for n-dodecane is at higher temperatures with significantly shorter ignition delay times. Noting that the n-dodecane content is highest within the Jet-A surrogate, these mechanism shortcomings likely affect the Jet-A surrogate ignition delay predictions at high pressures. The effect of other surrogate components' chemistry, in particular for iso-cetane and toluene, is uncertain, since ignition delay measurements for those two molecules do not exist in the temperature range where NTC behavior is observed for Jet-A (700 K ~ 950 K).

Figure 4.5 compares the calculated ignition delays of the three surrogates against shock tube ignition delay measurements of three target jet fuels at 20 atm, the only pressure where shock tube ignition delay measurements [107] are currently available for IPK and S-8. Although the NTC regime for both IPK and S-8 is predicted to be within higher temperature regions, the calculated ignition delay times for both surrogates successfully capture the overall measurement trends. In the high temperature regime above 1000 K, the difference in measured ignition delay times between the three fuels is small - similar behaviors are also observed in the kinetic modeling results. In the low and

NTC temperature regime where the ignition delay times are distinguishable, the relative order of the calculated ignition delay times corresponds to the relative reactivity of the surrogates; the quantitative ignition delay agreement however needs to be improved. As the measured DCN indicates, the reactivity of the S-8 surrogate is the highest (DCN of 61.1), followed by the Jet-A surrogate (DCN of 47.8), and finally the IPK surrogate (DCN of 31.9), which align well with the relative ignition delay times from the simulation.

4.2 Skeletal Mechanism Development

For the utilization of the developed surrogates in CFD simulations, a skeletal version of the detailed MFC mechanism was generated by using Directed Relation Graph with Error Propagation and Sensitivity Analysis (DRGEPSA) [112], an automated reduction algorithm implemented in the commercial CFD package CONVERGE [113]. The original DRG algorithm [114,115] and its various derivatives including DRGEPSA [112,116,117] generates skeletal versions of detailed mechanisms for large hydrocarbons by identifying and removing unimportant species. For the current study, the DRGEPSA reduction algorithm was configured to remove species in the detailed mechanism that have a small impact on the ignition delay calculation in the homogeneous reactor setup. The ignition delay calculations monitored for the mechanism reduction were for all three surrogates (Jet-A, IPK, S-8) in the low to high temperature regime (700 K ~ 1100 K), with equivalence ratios from 1 to 2, and pressures from 20 atm to 40 atm to account for the thermodynamic conditions relevant to the ignition of direct injected diesel engine.

It was found that the preliminary skeletal mechanism generated by the reduction algorithm included some species without consumption reactions, making certain pathways ‘dead-ended’. This may be a significant problem for the completeness of the kinetic mechanism. In order to fix this issue, the consumption pathways of those ‘dead-ended’ species were restored if it could be done by recovering a few species and reactions in the parent detailed mechanism. Otherwise, the ‘dead-ended’ species and associated reactions were removed. The initial skeletal mechanism from the reduction algorithm included 12 ‘dead-ended’ species. After restoring and eliminating these pathways, the final skeletal mechanism for the six-component surrogate palette was generated, which includes 360 species and 1851 reactions.

Figure 4.6 compares the ignition delay times calculated by the skeletal mechanism against those from the detailed mechanism, while Table 4.1 summarizes the deviations from the detailed mechanism. Overall, the skeletal mechanism maintains the ignition delay characteristics of the surrogates predicted by the detailed MFC mechanism. For Jet-A, the average absolute deviation (8.0%) and the maximum deviation (+23.2%) from the parent detailed mechanism was the smallest among the three surrogate fuels over the range of conditions examined in the reduction. For IPK, the deviation was well under ±20% for temperatures above 775 K for all pressures and equivalence ratios, while up to +44% deviation is observed in the region below 775 K. The most notable discrepancy for the S-8 surrogate is within the NTC regime, where the skeletal mechanism under predicts ignition delay with a maximum deviation of -33.8%. The reduction in computational expense with the skeletal mechanism is drastic. For example, while the parent detailed mechanism took approximately 3 to 5 hours to complete a single homogeneous reactor

simulation, the 360 species mechanism required less than one minute to run the identical case.

4.3 Summary and Conclusions

Ignition delay calculations for the newly developed jet fuel surrogates were carried out using a detailed kinetic mechanism and compared against experimentally measured ignition delay times from shock tubes. Calculated ignition delays of the Jet-A surrogate at 20 atm showed very good agreements with the experimental measurement. At 40 atm, however, the calculated ignition delays of Jet-A surrogate were notably shorter than experiments in NTC regime which can be attributed to the n-dodecane chemistry in the detailed mechanism. Estimating the effects of other surrogate components' chemistry is challenging, due to the scarcity of experimental ignition delay data in high pressure condition. Since pressures higher than 40 atm are expected at the time of fuel injection in Diesel engine, more experimental ignition delay data from shock tube or rapid compression machine as well as improvements in chemical mechanism at such high pressure is necessary. For IPK and S-8 surrogates, the calculated ignition delay times captured the general experimental ignition delay trends, while the agreements with experimental data, in particular in NTC and low temperature regime, could be improved in the future.

Also, a skeletal version of the detailed mechanism was generated using an automated reduction algorithm for the utilization of the surrogates in CFD simulation. After the mechanism reduction (4236 species to 360 species), the time needed for a homogeneous reactor simulation to complete drastically decreased, from 3 ~ 5 hours to

less than a minute, which makes the use of the developed surrogates possible for reacting CFD simulation.

Tables

Table 4.1. Deviations from the detailed mechanism for the 360 species skeletal mechanism. Avg.Abs indicates the average of absolute deviations for all 100 simulated points for each fuel, while Max indicates the largest deviation among those 100 simulated points.

Jet-A POSF-4658		IPK POSF-5642		S-8 POSF-4734	
Avg.Abs.	Max	Avg.Abs	Max	Avg.Abs	Max
8.0%	+23.2%	9.8%	+43.9%	13.6%	-33.8%

Figures

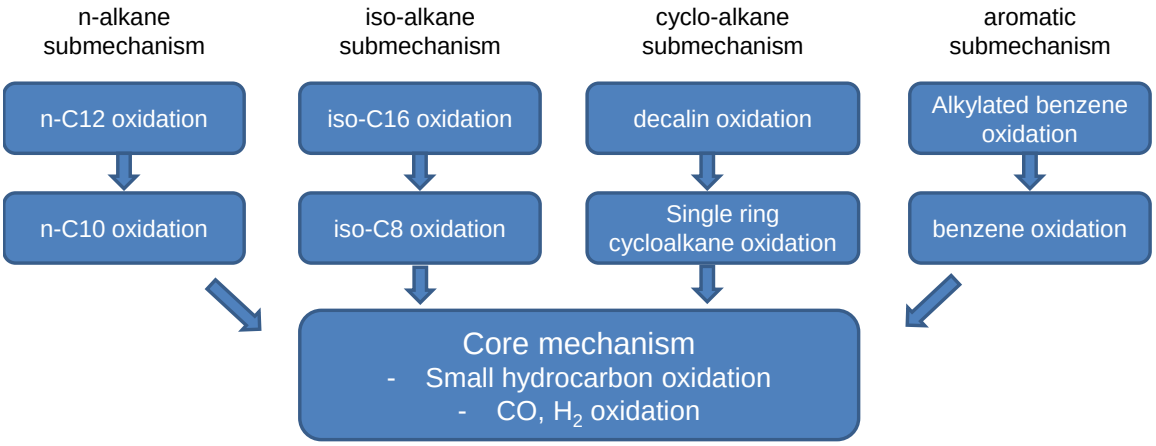

Figure 4.1. Modular structure of the detailed chemical mechanism.

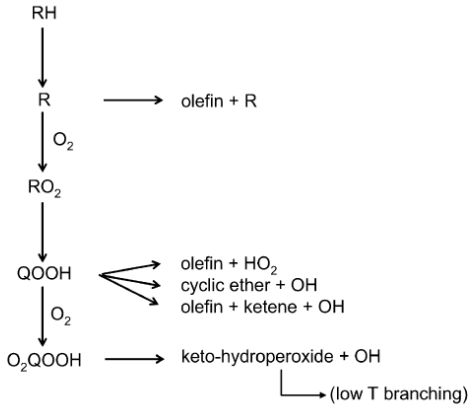

Figure 4.2. Reaction path diagram for n-, iso-, and cyclo-alkane submechanisms of the detailed mechanism [118].

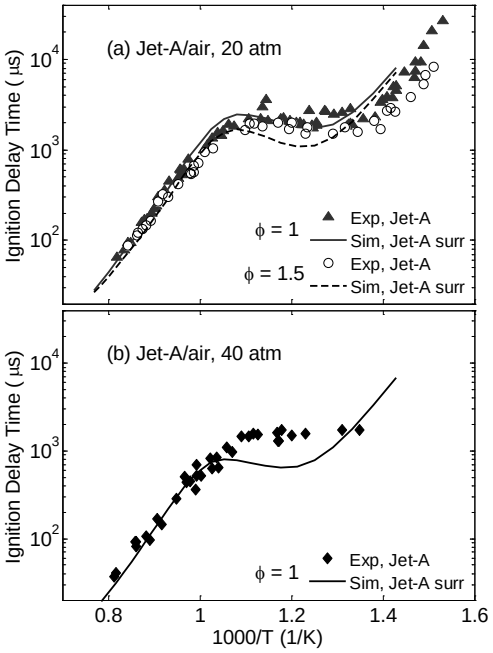

Figure 4.3. Comparisons of Jet-A/air mixture ignition delay measurements [28,40,107] with the calculated ignition delays with the Jet-A surrogates and the detailed mechanism at (a) 20 atm and (b) 40 atm.

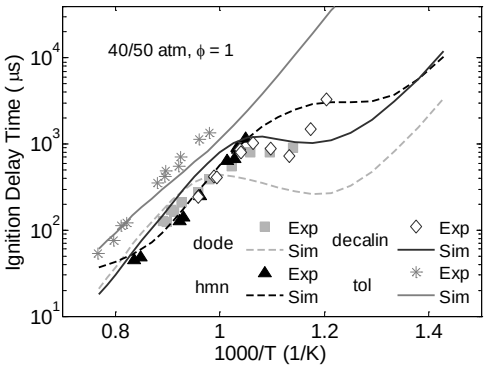

Figure 4.4. Comparison of stoichiometric fuel/air mixture ignition delay measurements for the Jet-A surrogate constituents [108–111] with calculated ignition delays using the detailed mechanism. 40 atm for n-dodecane (dode) and iso-cetane (hmn), and 50 atm for decalin and toluene (tol).

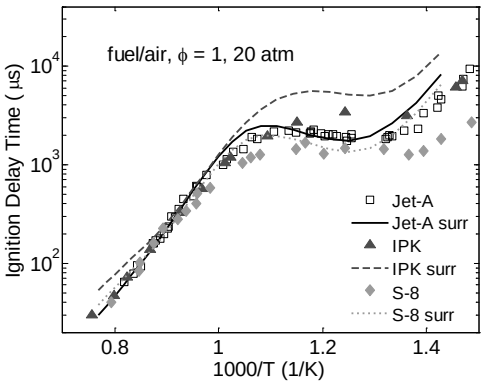

Figure 4.5. Comparison of stoichiometric fuel/air mixture ignition delay measurements at 20 atm with the calculated ignition delays with the detailed mechanism of the Jet-A, IPK, and S-8 surrogates.

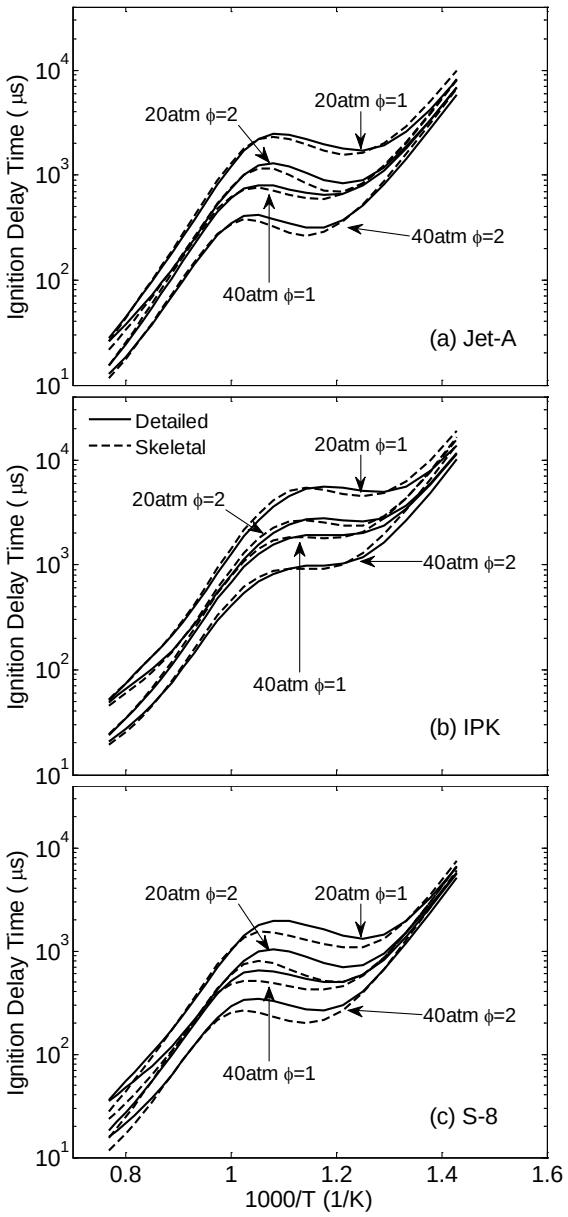

Figure 4.6. Comparisons of ignition delay predictions from the 360 species skeletal mechanism against the detailed MFC mechanism for (a) Jet-A, (b) IPK, and (c) S-8.

Chapter 5

The Relative Importance of Liquid Fuel Physical and Chemical Properties to Reacting Spray Ignition Delays

In this chapter, the developed surrogate mixtures and their skeletal mechanism are utilized within reacting spray simulations to investigate the relative importance of the physical and chemical properties to the ignition process within a reacting spray.

5.1 Background

Previously, the relative importance of physical and chemical properties to the ignition process has been experimentally investigated using spray bombs. One of the approaches was to differentiate the physical and chemical processes by comparing the pressure trace from a reacting case with fuel injection into air against a pressure trace from an inert case with fuel injection to inert nitrogen. The instance when the two pressure traces diverge is defined as the end of the physical delay period and the start of the chemical delay [119,120]. While this simple methodology attempts to isolate the closely-coupled physical and chemical processes, the physical delay time is significantly over-estimated. By their definition, the time needed for the vaporized fuel to be prepared

by oxidation chemistry to achieve noticeable heat release is regarded as physical delay. However, in principle, that period should be chemical delay. A similar study using a constant volume spray chamber with optical access called Cetane Ignition Delay (CID) has been reported [121]. Experimental studies using an Ignition Quality Tester (IQT) with isomeric fuels [92,122,123] concluded that the resulting difference in oxidation chemistry, and not physical property differences, was the dominating factor for the change in ignition delay time under the normal IQT operating condition (ambient charge of ~ 818 K at ~2.1 MPa). Bogin et al. [92] also observed that the change in liquid phase physical processes, which were perturbed by changing either the orifice diameter, injection pressure, or injected fuel mass, only caused small changes in ignition delay times (maximum 14%), while changes in the fuel auto-ignition quality resulted in a greater than 100% longer ignition delay relative to the baseline case. These temperatures may differ significantly from the start of injection temperatures in diesel engines, which have been estimated to range from approximately 850 to 1100 K [52]. The relative importance of physical and chemical processes to the ignition delay time may be therefore different from those previously investigated within IQT experiments. A series of numerical experiments under engine-relevant pressures and temperatures are therefore performed to understand the relative importance of liquid fuel chemical and physical properties to the ignition delay period.

5.2 Model Configuration

CFD simulations of reacting sprays within the Sandia National Laboratories' constant volume chamber with optical access were conducted using the CFD package

CONVERGE [124]. The models and meshing used for these simulations are identical to those within Chapter 2, and only brief descriptions are given here. The turbulence in the gas-phase flow field was modeled with RANS RNG k-ε model. The modified Kelvin-Helmholtz – Rayleigh-Taylor (KH-RT) model was used to predict the breakup and atomization of the liquid fuel. Droplet evaporation was modeled with Frossling correlation. For the 108mm cubic chamber, a computational mesh of 0.25 mm minimum grid size was used; the base mesh size of 2 mm was refined with an automatic mesh refinement algorithm; fixed embedding was used near the nozzle to increase the spatial resolution.

The 360 species skeletal mechanism developed in Chapter 4 was utilized for the simulation of chemical kinetics. The fuels simulated here (Jet-A, S-8) utilized this chemical mechanism along with select species from the six-component surrogate palette (n-dodecane/n-decane/iso-cetane/iso-octane/decalin/toluene) described previously.

Identical definitions to those in Chapter 2 were used for predicted liquid/vapor penetration lengths and ignition delay times. The liquid penetration length was defined as the axial distance from the nozzle exit to the region that encompassed the 95^{th} percentile of the total liquid fuel mass at a given time. The vapor penetration length was defined as the maximum axial distance from the nozzle exit to where the fuel mass fraction is 0.1%. The ignition delay was defined as the time between start of the injection and the maximum rise rate of peak temperature.

5.3 Model Validation

Reacting spray simulations were compared against Sandia's reacting spray experiments [55,125,126] for the validation of the CFD model and the chemical mechanism. Details of the experiments are summarized in Table 5.1. Among the three jet fuels for which the surrogates were developed in Chapter 3, experimental data from Sandia's combustion chamber exists for Jet-A POSF-4658 and S-8 POSF-4734 in [55,125] which was used for validation; no data could be found for IPK POSF-5642. Another reason for excluding IPK surrogate for current study is that as expected from Figure 4.5 where the calculated ignition delay times for IPK in homogeneous reactor model were notably longer than shock tube measurements, ignition delay time from spray simulation was excessively longer than Sandia's measurements of similar CN fuels from their spray chamber. Further modifications in chemical mechanism may be necessary in the future for the IPK surrogate.

For additional validation, spray experiments using a conventional JP-8 batch with CN of 38 [126] were also used. For the simulation of this specific JP-8, a surrogate mixture was formulated using the surrogate optimizer in Chapter 3 to match the JP-8 properties from the reference [126]. The surrogate mixture for JP-8 with 38 CN was n-dodecane/n-decane/iso-cetane/decalin/toluene = 0.1417/0.1699/0.2989/0.2487/0.1408 in volume fractions.

Figure 5.1 compares the calculated and experimental liquid/vapor penetration of JP-8 fuel sprays at the 850 K 14.8 kg/m^3 ambient condition. The JP-8 spray experiments used injectors with 0.180 mm orifice diameter. For this injector, the model constant B_1 in KH-RT spray breakup model, which varies depending on the injector, was set at 10.5. In

general, the model captured the liquid and vapor penetration length trends. Figure 5.2 shows the calculated liquid penetration length with the Jet-A surrogate and the S-8 surrogate at 900 K, 22.8 kg/m^3. Note that the orifice diameter is half the size of the injector used for JP-8 experiments (0.18 mm vs 0.09 mm). For Jet-A and S-8 simulations, the KH-RT model constant was set at 8.5, which is identical to the value used in Chapter 2, where the same injector was used. When compared to the stabilized liquid penetration lengths in experimental data in [55], which are 10.5 mm for Jet-A and 10.4 mm for S-8, the predicted liquid penetration lengths in Figure 5.2 (10.9 mm for Jet-A, 9.9 mm for S-8) are in good agreement. In particular, the model was capable of capturing the slightly shorter liquid penetration length of S-8 compared to Jet-A, which can be attributed to the successful emulation of the various liquid physical properties.

Figure 5.3 compares the predicted and experimental ignition delay times of the JP-8 sprays over a range of temperature at two ambient densities. Ignition delay predictions for both density conditions were in reasonable agreement at the highest temperature condition at 1200 K. At 1000 K, while the higher density case (30 kg/m^3) agreed reasonably well with the experimental data, the ignition delay time at 14.8 kg/m^3 was significantly over-predicted. When lower temperature cases were simulated, the JP-8 surrogate sprays were predicted to be significantly slower to ignite than experiments or even failed to achieve ignition (not shown).

Figure 5.4 shows the simulated heat release rates of Jet-A and S-8 fuel sprays at 900 K and 1000 K at 22.8 kg/m^3 ambient density. To achieve reasonable agreement with the experimental ignition delay times, the ambient temperatures were increased by 80 K for the 900 K case, and 30 K for the 1000 K case. When the ambient temperatures

corresponding to experiments were used in the simulations, the ignition delay times were considerably longer than measured values. Such slower ignition processes in CFD simulation is consistent with the observation in Figure 5.3. The calculated/measured ignition delay times were 0.925/0.70 ms for Jet-A and 0.608/0.58 ms for S-8 at 900 K as shown in Figure 5.4 (a), and 0.539/0.47 ms for Jet-A and 0.428/0.40 ms at 1000 K case in Figure 5.4 (b).

These comparisons show that the model captures the trends in experimental liquid/vapor penetration lengths for all three surrogates tested. For the ignition delay times, the CFD simulation results agree well with experimental measurements at temperatures higher than 1000 K in general, while improvements in the ignition predictions are needed at lower temperatures. The modeling set up with the Jet-A and S-8 surrogates is used as the baseline cases for the following numerical studies, which seek to identify the importance of physical and chemical processes to the ignition delay period.

5.3 Surrogate Property Modification Method

In order to investigate the relative importance of physical and chemical liquid fuel properties to spray ignition, a numerical experiment was designed to isolate the impact of liquid fuel physical and chemical properties on ignition delay using in part the baseline CFD cases as illustrated in Figure 5.5. The objective of this numerical study is to quantify the change in the ignition processes and ignition delay times as a result of assigned variations in physical and chemical processes. The baseline case for comparison was the original Jet-A surrogate (JetA_base in Figure 5.5). Then, either the physical properties or

the oxidation chemistry of the original Jet-A was swapped with that of S-8 (JetA_chem_S8_phy or JetA_phy_S8_chem in Figure 5.5).

In CONVERGE, the temperature dependent liquid physical properties of surrogate components are defined with a tabulated data file. It includes liquid viscosity, surface tension, heat of vaporization, vapor pressure, conductivity, density, and specific heat of each surrogate components as a function of temperature up to their respective critical temperatures. To achieve the variations in physical properties of the baseline Jet-A surrogate (JetA_chem_S8_phy), the Jet-A surrogate components' density, viscosity, specific heat, and vapor pressure in the tabulated data were manipulated to match those properties of S-8 as illustrated in Figure 5.6, while keeping the composition of the baseline Jet-A surrogate unchanged. Note that the four physical properties adjusted here were identified to have significant effects on the spray ignition process in Chapter 2. For example, to match the density of S-8 with the Jet-A surrogate, liquid densities of n-dodecane, iso-cetane, decalin, and toluene (Jet-A surrogate components) were multiplied by 0.924. Viscosity, specific heat, and vapor pressure were adjusted with the same manner. For the oxidation chemistry variation (JetA_phy_S8_chem), the surrogate composition was replaced with that of S-8 to obtain the gas phase chemistry of S-8, and the four physical properties of its surrogate components were modified to match those of Jet-A, as shown in Figure 5.7.

The premise of this method is that when the surrogate fuel physical properties are matched, the physical phenomena governing the spray ignition process are also closely matched regardless of the surrogate components and composition. In order to verify this premise, all the injection related parameters such as injection mass flow rate, injection

velocity, and injection pressure were monitored and the difference was negligible between JetA_base and JetA_phy_S8_chem (different surrogate components but matched physical properties). In particular, the injection velocities of JetA_base and JetA_phy_S8_chem were nearly identical as shown in Figure 5.8, which was achieved by matching density of the two surrogate mixtures – this relationship was demonstrated in Chapter 2. As a result, the turbulent mixing rates were similar for these two cases. Figure 5.9 compares the turbulent viscosities of JetA_base, JetA_phy_S8_chem, and S8_base at 1000 K 22.8 kg/m^3 at 0.3 ms after the start of the injection. For this comparison, non-reacting simulations were performed to examine the fuel property effects on turbulent mixing without the effects from heat release. Note that the turbulent viscosity (μ_t) determines the turbulent thermal and mass mixing rates for the RANS turbulence modeling used for this study as shown in the Equation 6 and 7 in Chapter 2.

$$K_t = K + c_p \frac{\mu_t}{\mathrm{Pr}_t} \quad \text{(Eq. 6)}$$

$$D_t = \frac{\mu_t}{\rho Sc_t} \quad \text{(Eq. 7)}$$

where K_t is the turbulent thermal diffusivity, D_t is turbulent mass diffusivity, K is the molecular thermal conductivity, c_p is the gaseous specific heat, Pr_t is the turbulent Prandtl number, and Sc_t is the turbulent Schmidt number. It is clearly shown in Figure 5.9 that the distribution of local turbulent viscosity of JetA_phy_S8_chem is more similar to JetA_base than to the baseline S-8 case, indicating that the turbulent thermal and mass mixing rates of JetA_phy_S8_chem is closely matched to JetA_base.

These comparisons confirm that the current method is valid to isolate the effect of either physical or chemical properties to the ignition process. This numerical study was conducted under three different ambient conditions (900 K, 1000K, 1200 K at 22.8 kg/m^3) where the model showed reasonable agreement with experimental data.

5.4 Results – Physical Property vs Oxidation Chemistry

Table 5.2 summarizes the expected changes in ignition processes when the physical properties or oxidation chemistry of S-8 are assigned to the baseline Jet-A surrogate. S-8 has faster oxidation chemistry than Jet-A as shown in experiments and zero dimensional simulations in Figure 4.3. Thus, JetA_phy_S8_chem is expected to have a shorter ignition delay than JetA_base.

As discussed in Chapter 2, liquid specific heat affects ignition delay time by influencing the local temperature. S-8 has higher liquid specific heat than Jet-A, which will result in lower local temperature throughout the ignition process and longer ignition delay period. In addition, the liquid volatility also affects the local temperature, which was not discussed in Chapter 2 due to its smaller effect than specific heat. Higher volatility of S-8 lowers the liquid temperature at which the evaporation occurs. In such case, although the specific heat curve itself does not change, the total energy needed for vaporization of the fuel (Q_{total} in Equation 5) will decrease since the final droplet temperature ($T_{d,end}$) is lower. Note $C_{p,liq}$ increase as liquid temperature increase, as shown in Figure 2.8.

$$Q_{total} = \int_{T_{d,init}}^{T_{d,end}} \left(C_{p,liq} m_d - h_{vap} \frac{dm_d}{dT_d} \right) dT_d \qquad \text{(Eq. 5)}$$

Thus, higher volatility of S-8 will increase the local temperature which will offset some of the effect coming from higher specific heat of S-8.

In addition, the turbulent mixing rates were influenced by liquid density, which showed significant impact on ignition delay time. S-8 has significantly lower density than Jet-A, which is shown to have competing effects on the total ignition delay time. As concluded in Chapter 2, lower density results in faster turbulent thermal and mass mixing rates, which advances the first stage heat release (LTHR) by enhanced initial charge preparation. On the other hand, it retards the onset of high temperature chemistry because of the enhanced mixing of the high temperature zones with cooler ones within the jet, which limits local peak temperatures.

Figure 5.10 compares the global heat release rates and ignition delay times for the physical property/oxidation chemistry variation studies, with the time axis normalized by the ignition delay time of the baseline Jet-A case. Calculated ignition delay times and the relative change from the baseline Jet-A case are summarized in Table 5.3. Under all three conditions tested, it is observed that the changes in ignition delay times are larger when the oxidation chemistry is varied (JetA_phy_S8_chem) compared to the physical property variations (JetA_chem_S8_phy). While the ignition delay times were shortened by 36.6% for the 900 K case, 23.1% for the 1000 K case, and 12.3% for the 1200 K case when the oxidation chemistry of S-8 was assigned to Jet-A, the physical properties of S-8 only caused + 12.2%, + 5.6%, and + 1.0% increase in ignition delay time at the respective ambient conditions. It can be concluded from this observation that the effect of oxidation

chemistry on the spray ignition process is more important than the effect of liquid fuel physical properties, which is in agreement with conclusions from previous experimental studies [92,122,123].

To investigate how these changes in ignition delay times occurred, a local reactivity analysis similar to the one shown in Chapter 2 is performed for the 1000 K case. The local reactivity distributions within the fuel spray were calculated at 0.07 ms after the start of the injection as marked in Figure 5.11, which is prior to start of noticeable low temperature heat release. The reactivity of each computational cell was represented by the inverse of ignition delay time calculated by the zero dimensional homogeneous reactor using the local pressure, temperature, and composition of each cell as the reactor solution's initial condition. Figure 5.12 shows the cumulative mass distribution within the local reactivity domain at 0.07 ms for the 1000 K case, which illustrates that the fuel spray with faster oxidation chemistry (JetA_phy_S8_chem) contains significantly more charge with elevated reactivity, while the physical property effects on the reactivity distribution is much smaller, considering the overlapping distributions. The increase in reactivity for the chemistry swap case (JetA_phy_S8_chem) is due to faster oxidation kinetics of S-8. Significantly larger change in the reactivity of the fuel spray from the oxidation chemistry swap proves the dominant effect of the chemical property on the spray ignition.

The local temperature – equivalence ratio distributions were also analyzed for the spray at 0.07 ms to examine the effect of S-8's specific heat and volatility on local temperature. Figure 5.13 (a) compares the temperature – equivalence ratio distributions for the physical property/oxidation chemistry variation studies at 0.07 ms after the start of

the injection when the heat release effect is negligible. It shows that all three cases have similar local temperature distribution within the spray. When the temperature – equivalence ratio distributions from non-reacting simulations are plotted at 0.2 ms as shown in Figure 5.13 (b), which shows the fuel property effects on temperature distributions within the spray without the effect from heat release, the local temperature distributions are still very similar when the spray is fully developed, although slightly lower local temperature is observed for JetA_chem_S8_phy. When compared to the large local temperature change shown in the specific heat perturbation cases from Chapter 2 in Figure 5.13 (c), the local temperature change for the JetA_chem_S8_phy case is significantly smaller and its impact on ignition delay time should be very limited. This observation indicates the effects from S-8's higher specific heat and higher volatility negate each other and resulted in only small decrease in local temperature, and, consequently, produce a very small change in local reactivity relative to the Jet-A spray.

Despite having minimal effect on LTHR in Figure 5.10, the heat release rate indicates that liquid fuel physical properties have a more prominent effect later in the ignition process, in and around high temperature ignition. As shown in Figure 5.11, the heat release rates for JetA_base and JetA_chem_S8_phy are virtually the same until 0.45 ms, but JetA_chem_S8_phy ignites later than the JetA_base. At this later phase of ignition, the enhanced mixing caused by the lower density of S-8 retards the onset of high temperature ignition chemistry as previously discussed in Chapter 2 and Table 5.2. To confirm, the temperature-equivalence ratio distributions of JetA_base and JetA_chem_S8_phy are plotted at 0.45 ms in Figure 5.14, where JetA_chem_S8_phy achieves ~ 50 K lower peak temperature than JetA_base. Since the cumulated heat

release is nearly the same for both cases at 0.45 ms, the lower local peak temperature and longer ignition delay time of JetA_chem_S8_phy is caused by S-8's higher rate of turbulent mixing due to lower liquid density.

Figure 5.15 compares the local heat release rates and the local temperatures with equivalence ratio contours (Φ = 1,2) for the 1000 K case prior to the start of the heat release (top figure), during the first stage LTHR phase (middle figure) and at the time of ignition (bottom figure) for the respective cases. For all three cases, the initial first stage LTHR are observed at the periphery of the jet (see middle figures) where the equivalence ratio is approximately 1 ~ 3, which is consistent with the local reactivity analysis in Figure 2.10 in Chapter 2. Prior to the start of the heat release (see top figures), the local temperatures in the periphery of the spray are approximately 850 K ~ 950 K. These observations implies that the relevant thermodynamic conditions for the initial first stage LTHR is fuel rich (Φ = 1~3), and 50 K ~ 150 K lower than the ambient charge temperature. At the time of ignition (bottom figures), all three cases showed that large portion of air/fuel mixture at the tip of the spray igniting at once, which is essentially premixed combustion. The equivalence ratio of the igniting charge at the tip of the spray is approximately 1 ~ 2, which agrees with the general understanding on the ignition sites being rich for the diesel/spray combustion.

5.5 Results – Temperature Dependency of Property Effects

Another conclusion that can be drawn from Figure 5.10 and Table 5.3 is that the effects of liquid fuel chemical and physical properties increase as the ambient temperatures decrease. As seen in Table 5.3, the relative ignition delay time change of

JetA_phy_S8_chem (oxidation chemistry effect) increased from 12.3% to 36.6%, and that of JetA_chem_S8_phy (physical property effect) increased from 1% to 12% as temperature goes down from 1200 K to 900 K. This is a particularly important finding, since it indicates fuel property effects on ignition delay will be more prominent during low load engine operation when the charge temperature is expected to be colder. In the opposite perspective, the negative effect of variations in DCN and physical properties on diesel engine can be minimized when the engine is operated with a strategy to have higher charge temperature at the time of injection.

5.5.1 Temperature Dependency of Oxidation Chemistry Effects

It is well known that the effect of Derived Cetane Number on gas phase ignition delay time is small in the high temperature regime, typically at temperatures above 1000 K. This can be seen in Figure 5.16 (a) [107,127] which are for fuels with a wide range of auto-ignition quality (DCN of 31 ~74). Note that the shock tube ignition delays are for fuels entirely in the gas phase, hence these ignition delay times represent only the chemical aspect of the ignition process. Meaningful differences in ignition delays are observed for temperatures lower than 1000 K. Such a trend is also captured by the calculated ignition delay times of these fuels using a zero dimensional homogeneous reactor model with a detailed chemical mechanism as shown in Figure 5.16 (b). For this reason, the effect of oxidation chemistry on the ignition process of fuel spray decreases at higher ambient temperature as shown for the JetA_phy_S8_chem case.

5.5.2 Temperature Dependency of Physical Property Effects

As discussed in the previous section, the dominant physical property effects on ignition delay time were associated with liquid density differences that influenced turbulent mixing rates and local temperatures during the later phase of the ignition delay. To investigate the reason for density's negligibly small effect at high temperature, evolution of the turbulent viscosities for the 1200 K cases is shown in Figure 5.17. When the turbulent viscosities of JetA_base and JetA_chem_S8_phy are compared, the difference between those two cases becomes significant only after 0.16 ms; during the very early phase of fuel injection, the difference in turbulent mixing rate is shown to be minimal. However, due to very fast oxidation chemistry at 1200 K ambient temperature, ignition is reached at ~ 0.19 ms for both JetA_base and JetA_chem_S8_phy, which implies that only short amount of time (~ 0.03 ms) was allowed for the deviations in turbulent mixing to influence the transition to high temperature ignition. As the ambient temperature decrease and the oxidation chemistry gets slower, there are more time for such mixing effects to be accumulated on the local temperature distribution, which results in greater change in ignition delay. Thus, the effect of variations in physical property on ignition delay time increases in lower ambient temperature.

5.6 Conclusions

CFD simulations of reacting fuel spray were performed with surrogates emulating various physical and chemical properties of JP-8, Jet-A, and S-8 fuels. Numerical

experiments were carried out to investigate the importance of liquid fuel physical and chemical properties to the ignition delay period.

1. Under the ambient conditions examined, the effect of variation in oxidation chemistry (12.3% ~ 36.6% change in ignition delay time) was significantly greater than the effect of physical properties (1.0% ~ 12.2% change in ignition delay time). It can be concluded that the chemical aspects of the ignition process dominate the physical aspects under the diesel-relevant conditions examined here.
2. The effects of physical properties on the first stage LTHR were minimal, as shown by negligibly small differences in global heat release rates between JetA_base and JetA_chem_S8_phy until the onset of high temperature ignition. It was also evident from very similar reactivity distributions before the start of heat release. This may be attributed to S-8's higher specific heat, higher volatility, and lower density compared to Jet-A have competing effects on the first stage LTHR. However, significant effects of these physical properties, in particular the turbulent mixing from the liquid density, were observed during the transition phase to high temperature ignition.
3. An analysis with the local heat release rate, temperature, and equivalence ratio showed that the thermodynamic condition relevant to the initial first stage LTHR is approximately 50 K ~ 150 K lower than the ambient charge temperature with the equivalence ratio of 1 ~ 3 under the conditions investigated in this study. The high temperature ignition was observed at the tip of the spray where the equivalence ratio is approximately 1 ~ 2.
4. Both oxidation chemistry effect and physical property effect diminished as the ambient temperature increases. In high temperature regime over 1000 K, the chemical

ignition delay time difference among fuels with different ignition quality is small. Also, since the oxidation chemistry gets faster exponentially, the time allowed for the deviations in turbulent mixing (liquid density effect) to influence the ignition process significantly decreases.

Tables

Table 5.1. Details of experimental spray data from Sandia National Laboratories.

Fuel	Jet-A POSF-4658	S-8 POSF-4734	JP-8[b]	JP-8 [b]
Cetane Number	47.3[a]	60.4[a]	38	38
Temperature (K)	900, 1000	900, 1000	850	1000, 1200
Density (kg/m^3)	22.8	22.8	14.8	14.8, 30
Pressure (MPa)	6.1, 6.7	6.1, 6.7	3.58	4.23 ~ 10.34
Orifice Diameter (mm)	0.09	0.09	0.180	0.180
Injection Pressure (MPa)	150	150	110	138
Ambient Composition	$N_2/CO_2/ H_2O/O_2$ = 0.7515/0.0622/0.0362/0.15		$N_2/CO_2/ H_2O/O_2$ = 0.6933/0.0611 /0.0356/0.21	
Reference	[55,125]		[126]	

[a] Derived Cetane Number from IQT

[b] The batch that was used in Pickett and Hoogterp [126], POSF number unknown

Table 5.2. Effects of S-8's physical properties and oxidation chemistry relative to those of Jet-A on ignition delay time.

	S-8 compared to Jet-A	Effects on ignition delay time
Oxidation chemistry	Faster	↓↓↓
Specific Heat	Higher	↑↑
Volatility	Higher	↓
Density	Lower	↓↓ (enhanced initial charge preparation) ↑↑ (slower onset of high temperature chemistry)

Table 5.3. Ignition delay times and the change in ignition delay times relative to the baseline Jet-A the physical property/oxidation chemistry variation studies.

	JetA_base	JetA_chem_S8_phy		JetA_phy_S8_chem	
	ID (ms)	ID (ms)	ID change (%)	ID (ms)	ID change (%)
900 K	0.931	1.045	+ 12.2	0.590	- 36.6
1000 K	0.549	0.581	+ 5.6	0.422	- 23.1
1200 K	0.193	0.195	+ 1.0	0.170	- 12.3

Figures

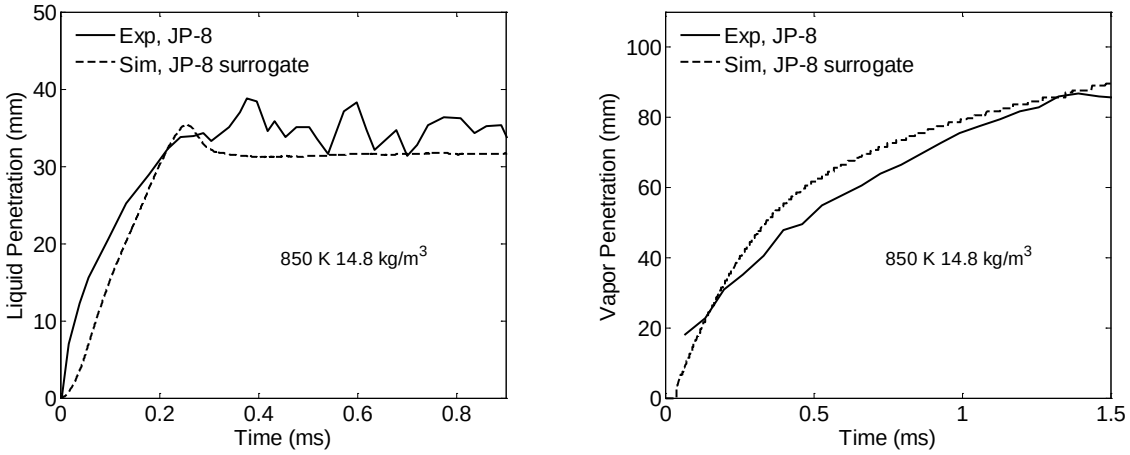

(a) (b)

Figure 5.1. Comparisons of predicted and experimental (a) liquid penetration lengths and (b) vapor penetration lengths of JP-8 spray at 850 K, 14.8 kg/m^3 [126].

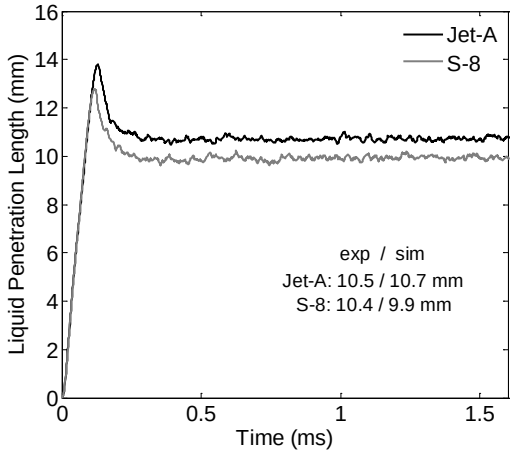

Figure 5.2. Calculated liquid penetration lengths using the Jet-A surrogate and the S-8 surrogate at 900 K 22.8 kg/m^3. Measured/calculated liquid lengths were 10.5/10.7 mm and 10.4/9.9 mm for Jet-A and S-8, respectively [55].

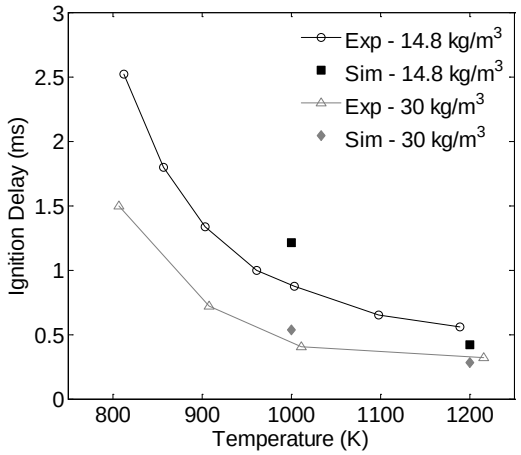

Figure 5.3. Comparisons of predicted and experimental ignition delay times for JP-8 spray over a range of temperature at two ambient densities (14.8 kg/m^3, 30 kg/m^3) [126].

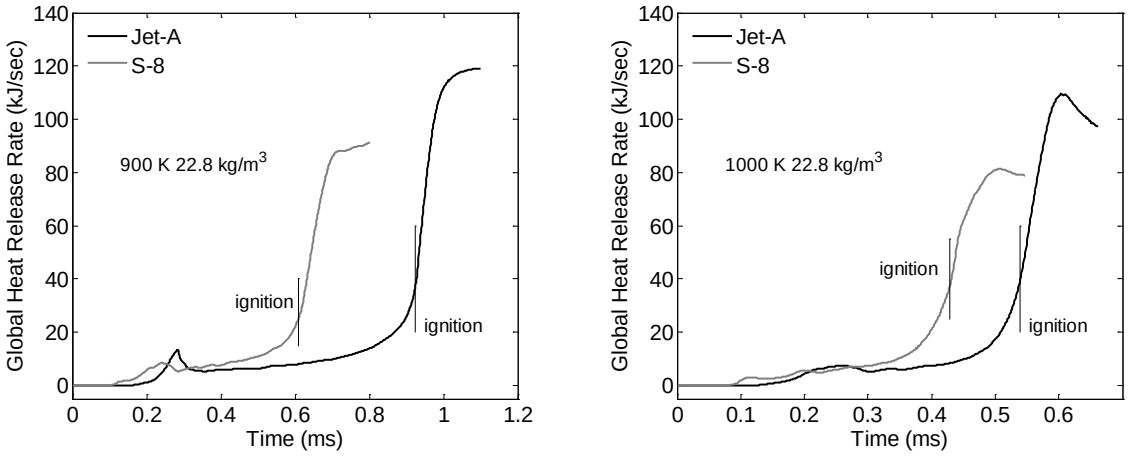

(a) (b)

Figure 5.4. Calculated global heat release rates and ignition timings of Jet-A and S-8 surrogates at (a) 900 K 22.8 kg/m^3 and (b) 1000 K 22.8 kg/m^3. Measured ignition delays were 0.70 ms for Jet-A and 0.58 ms for S-8 for the 900 K case, and 0.47 ms for Jet-A and 0.40 ms for S-8 for the 1000K case [125].

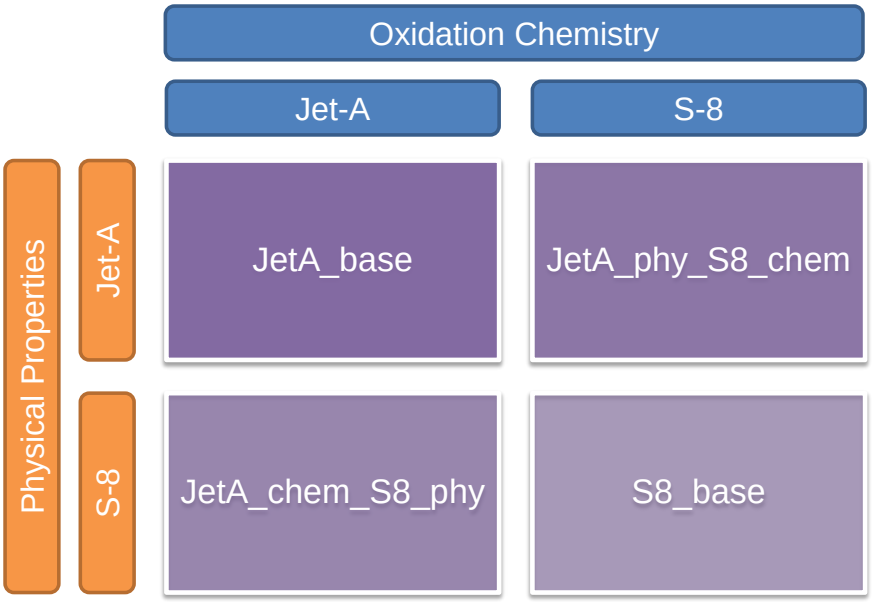

Figure 5.5. Schematics of the properties and oxidation chemistry swap study.

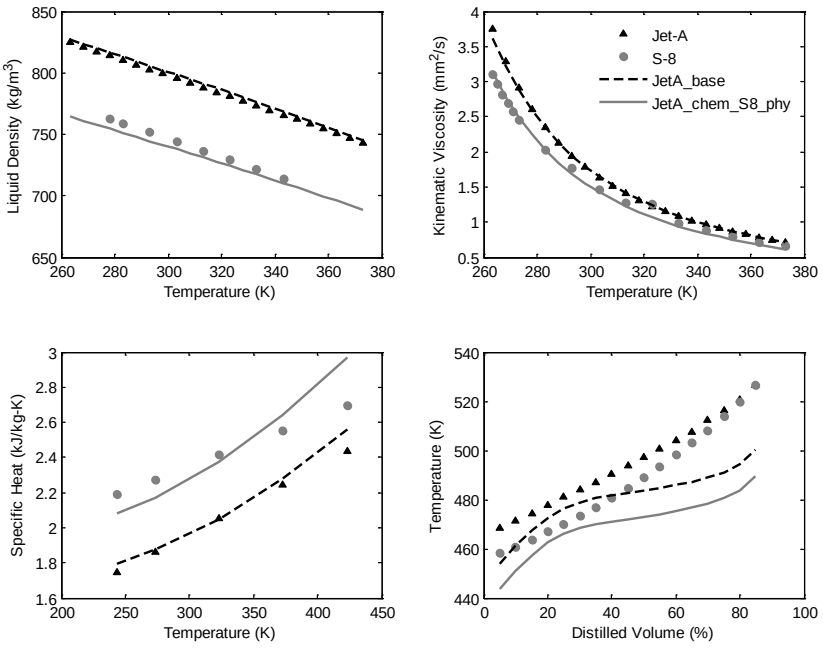

Figure 5.6. Physical property modifications to achieve a surrogate fuel of the oxidation chemistry of Jet-A with physical properties of S-8 (JetA_chem_S8_phy).

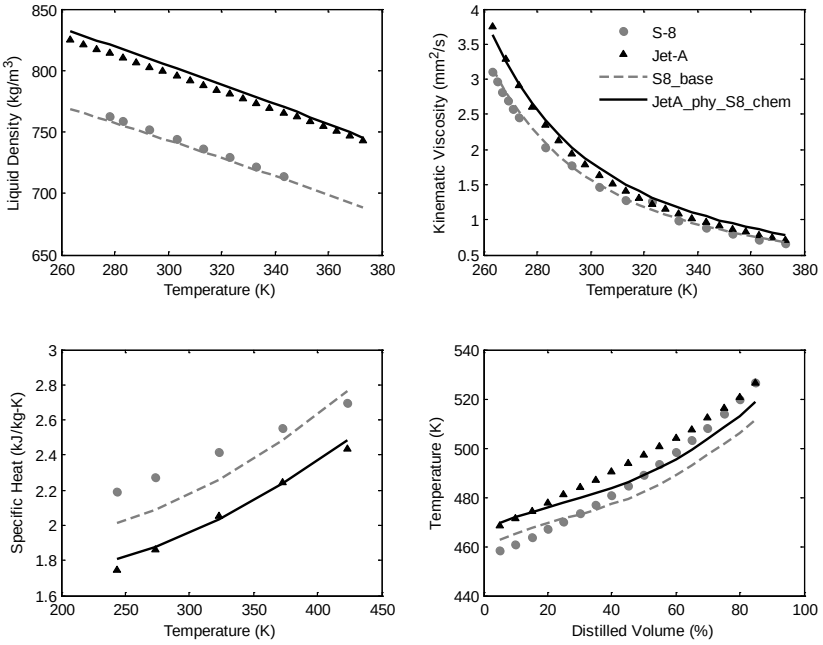

Figure 5.7. Physical property modifications to achieve a surrogate fuel of the physical properties of Jet-A with the oxidation chemistry of S-8 (JetA_phy_S8_chem).

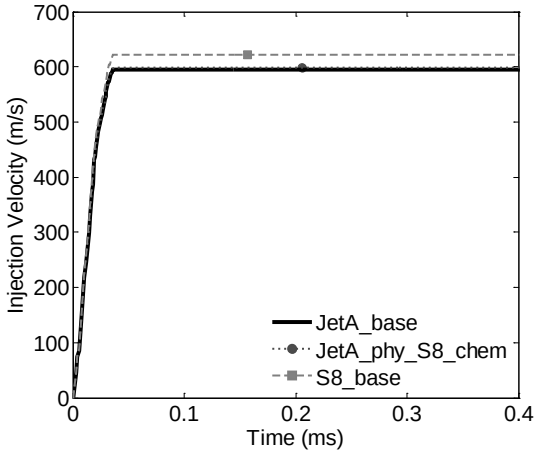

Figure 5.8. Comparisons of injection velocities of JetA_base, JetA_phy_S8_chem, and S8_base at 1000 K 22.8 kg/m^3.

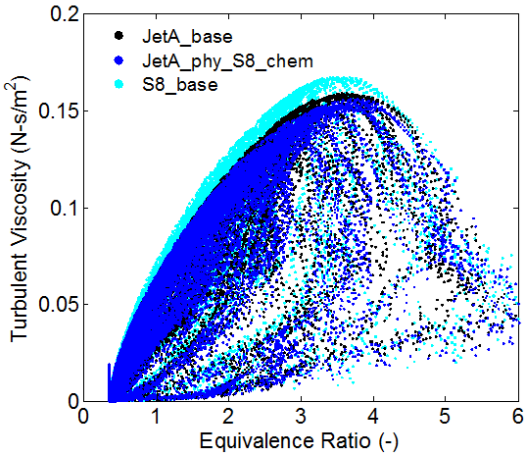

Figure 5.9. Comparisons of turbulent viscosities of JetA_base, JetA_phy_S8_chem, and S8_base at 1000 K 22.8 kg/m^3 at 0.3 ms after the start of the injection. Non-reacting simulations were performed.

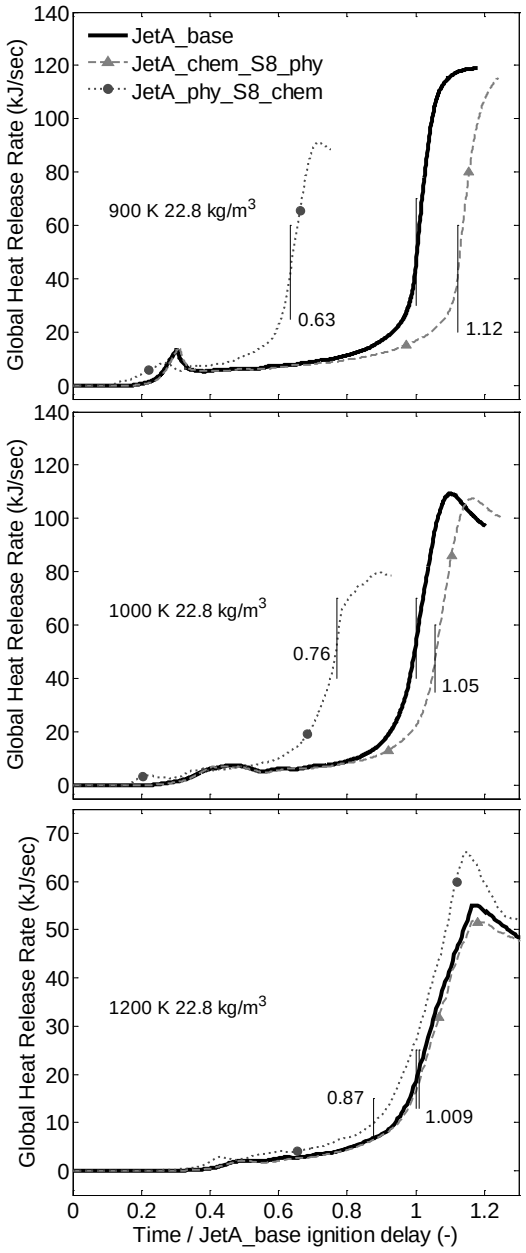

Figure 5.10. Comparisons of global heat release rates and ignition delay times for the physical property/oxidation chemistry variation studies. At each temperature condition, the time after the start of injection is normalized by the ignition delay time of the baseline Jet-A case. Determined ignition delay times of JetA_chem_S8_phy and JetA_phy_S8_chem relative to JetA_base are noted in the figures.

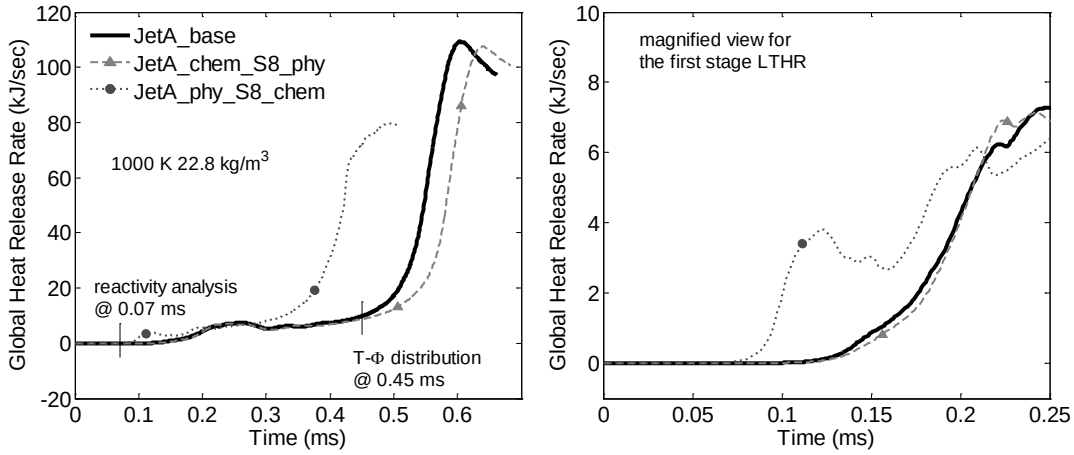

Figure 5.11. Global heat release rates for the physical property/oxidation chemistry variation studies at 1000 K 22.8 kg/m^3.

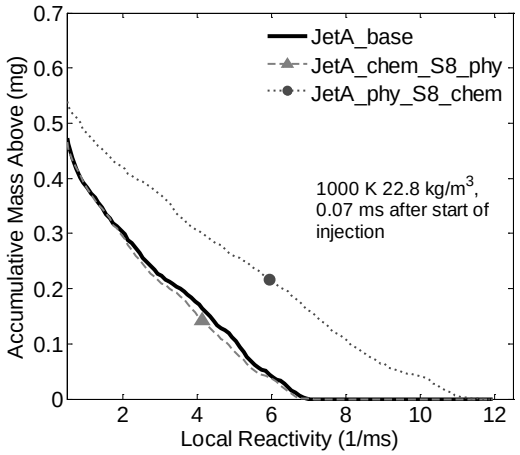

Figure 5.12. Accumulative mass distribution in the local reactivity domain just prior to the start of heat release (0.07 ms after start of the injection).

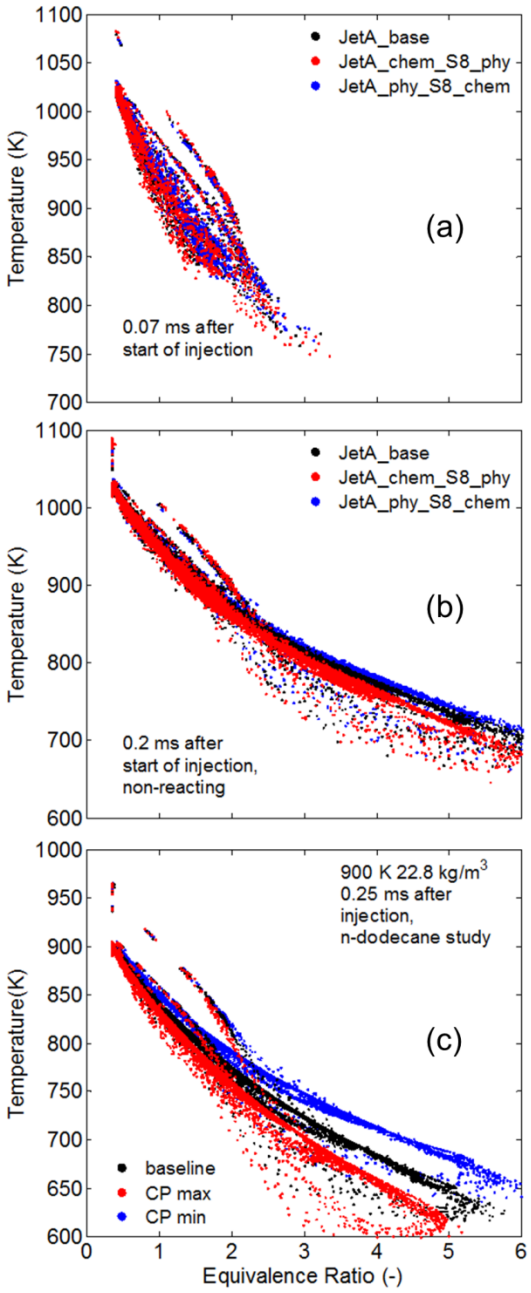

Figure 5.13. Comparisons of temperature – equivalence ratio distribution for the physical property/oxidation chemistry variation studies at 1000 K 22.8 kg/m^3. (a) is from the reacting simulations in Figure 5.12, while (b) is from non-reacting simulations. (c) is from the perturbation studies in Chapter 2 at 900 K 22.8 kg/m^3 where the local temperature change due to the specific heat perturbation is well-observed.

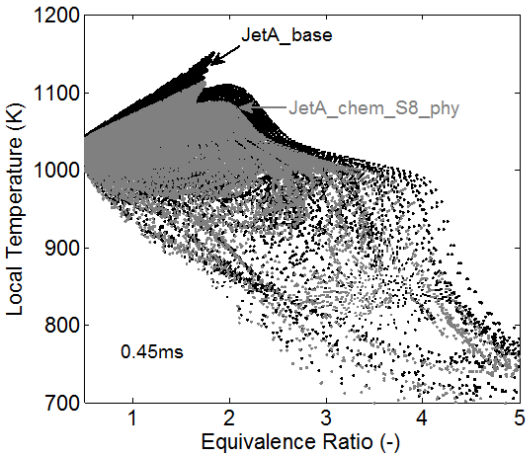

Figure 5.14. Comparisons of temperature - equivalence ratio distribution of the baseline Jet-A (JetA_base) and Jet-A surrogate with physical properties of S-8 (JetA_chem_S8_phy) for the 1000 K case at 0.45 ms after the start of the injection.

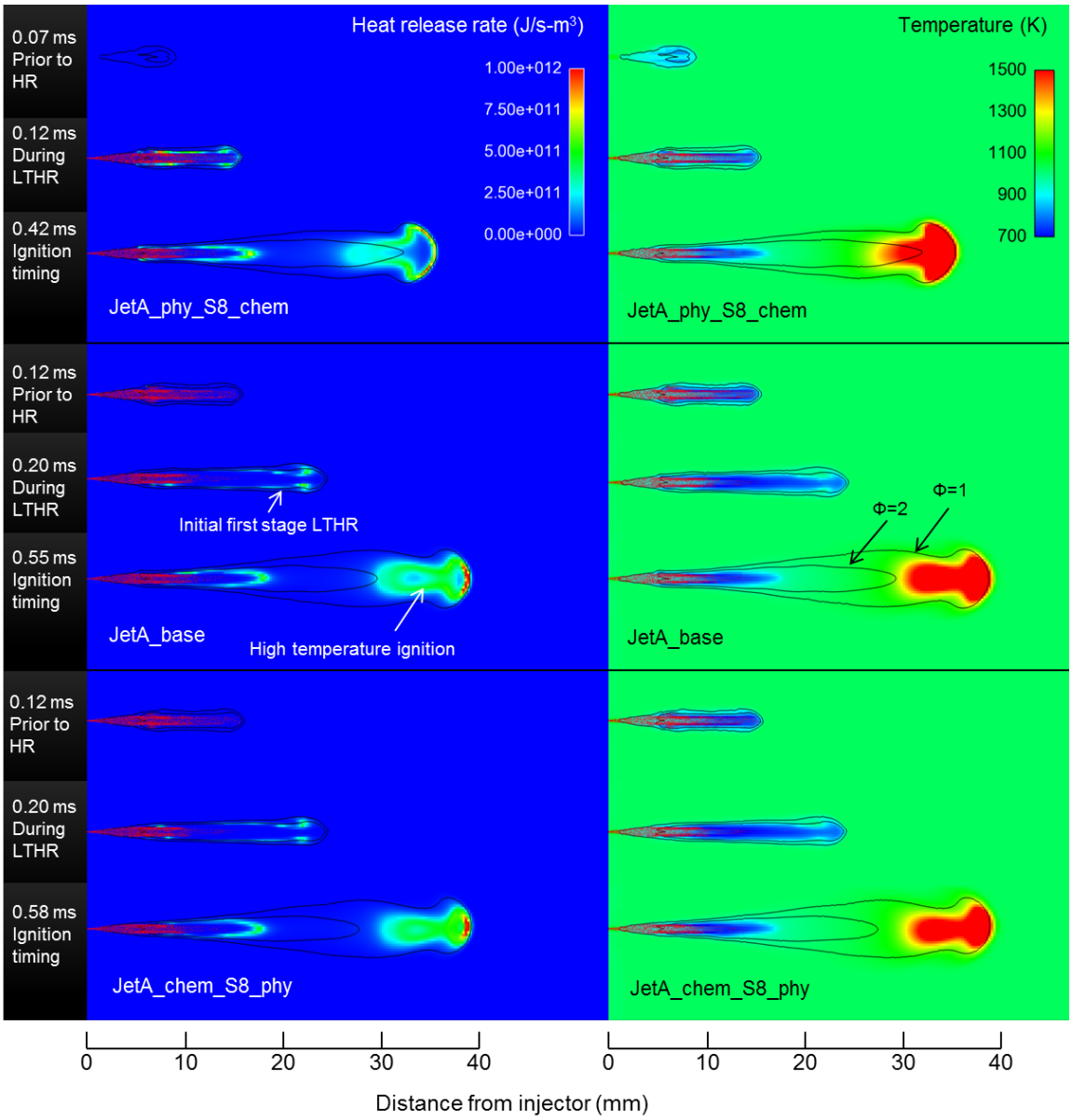

Figure 5.15. Comparisons of local heat release rates and local temperature with equivalence ratio contours for the physical property/oxidation chemistry variation studies at 1000 K 22.8 kg/m^3. The top figure of each case is during the first stage LTHR, the bottom is at the time of ignition.

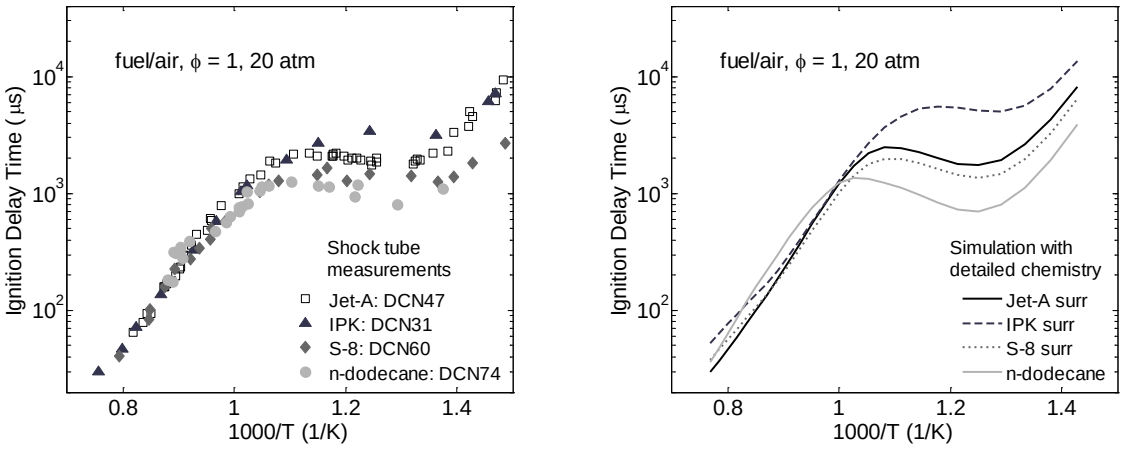

(a) (b)

Figure 5.16. Ignition delay comparisons for fuels with different autoignition qualities (DCN of 31 ~ 74). Measured ignition delay times from shock tube [107,127] is shown in (a), while calculated ignition delay times within homogeneous reactor model with a detailed chemistry is shown in (b).

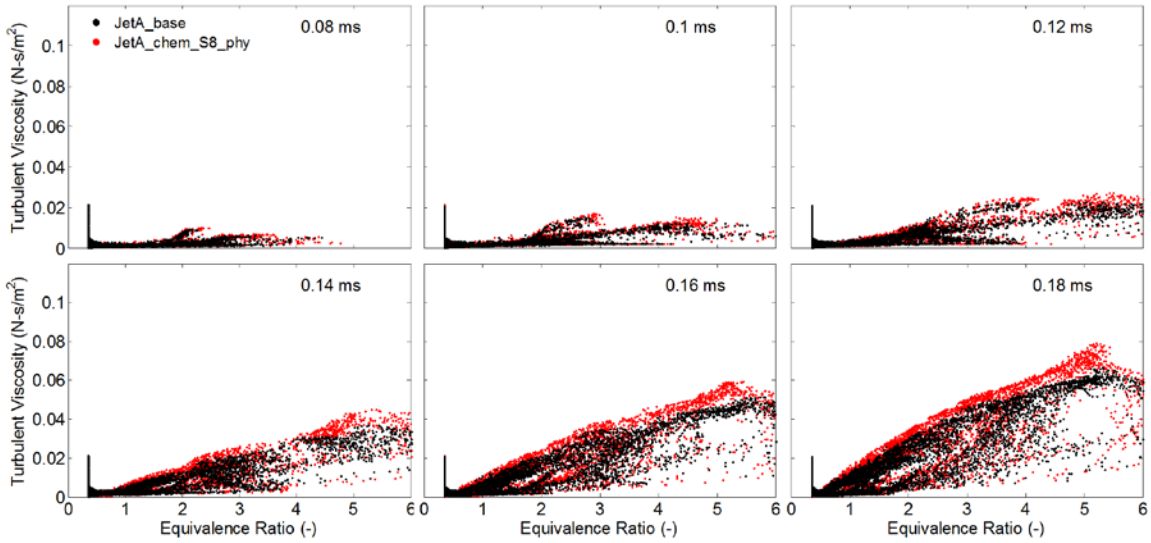

Figure 5.17. The evolution of the turbulent viscosities for JetA_base and JetA_chem_S8_phy cases at 1200 K 22.8 kg/m^3. The ignition timings for both cases were ~ 0.19 ms.

Chapter 6

Conclusions and Recommendations for Future Work

6.1 Conclusions and Contributions

The conclusions and original contributions of the dissertation are summarized as follows.

In Chapter 2, the effect of liquid physical property variations on direct injected diesel sprays and their ignition behavior was investigated with 3-dimensional CFD simulations. Six liquid physical properties were perturbed one at a time in order to isolate the effect of each property, which is not viable in experimental approaches. Rather than assigning the same relative perturbations for all properties, the range of perturbations for each property was determined to reflect the drastically different physical properties within hydrocarbon species often used in surrogate studies. Through this study, four liquid physical properties were identified that have significant impact on liquid penetration length and ignition delay time; these properties were density, viscosity, specific heat, and volatility. This study provides important insights for the development of future diesel combustion surrogates. In particular, a novelty of this work was the identification of the substantial effect of the liquid fuel's specific heat on liquid

penetration and ignition delay time, since this property has not been previously considered as a target property for emulation.

Chapter 2 also provided novel insight into the influence of liquid fuel physical properties on the ignition process. Local thermodynamic conditions, compositions, and resulting reactivity of the fuel spray were analyzed in order to understand how liquid fuel specific heat and density variations affect the ignition process. Higher liquid specific heat increases the amount of energy that should be transferred from the fresh charge to the liquid fuel for its vaporization, which results in lower charge temperatures and longer ignition delays. Liquid density influenced turbulent mixing rates, where higher density resulted in lower injection velocities hence turbulent mixing rates at constant injection pressure. Lower turbulent mixing rates caused slower progress in the first stage LTHR phase due to slower initial charge preparation. However, the lower mixing rates caused an earlier onset of high temperature oxidation chemistry by allowing higher peak temperatures during the transition from the NTC period to high temperature ignition.

In Chapter 3, a surrogate optimizer was developed that is capable of emulating various fuel properties including chemical properties and temperature-dependent liquid physical properties (DCN, LHV, H/C, MW, density, viscosity, specific heat, and volatility). The results from Chapter 2 were applied here for determining the target properties and their respective weights used within the optimizer's objective function. A surrogate palette composed of six components (n-dodecane/n-decane/iso-cetane/iso-octane/decalin/toluene) was proposed which is capable of capturing physical and chemical properties of petroleum-derived conventional jet fuels as well as non-petroleum-derived alternative jet fuels. For the optimizer, a regression equation was

developed to correlate the composition of a mixture within the surrogate palette to mixture DCN. Also, a distillation curve model was implemented within the optimizer that solves the liquid-vapor equilibrium equations with Raoult's law. Using the surrogate optimizer, surrogate mixtures were formulated targeting the physical and chemical properties of a representative petroleum-derived Jet-A POSF-4658, a coal-derived IPK POSF-5642, and a natural gas-derived S-8 POSF-4734. Of particular significance, the jet fuel surrogates developed in this work are the only surrogates targeted for chemical kinetic modeling while matching both physical and chemical properties of jet fuels. Moreover, by sharing a common palette, combustion modeling of any surrogate mixtures formulated within the surrogate development framework can be carried out with a common chemical mechanism.

In Chapter 4, a state-of-the-art detailed kinetic mechanism that includes all the surrogate components in the six component surrogate palette was used to calculate the ignition delay times of the developed surrogates. While improvements to the chemical mechanism are necessary in the future, in particular under high pressure condition, the surrogates with the kinetic mechanism successfully captured the experimental ignition delay trends with simulations in a zero dimensional homogeneous reactor model. A skeletal version of the detailed mechanism was developed using an automated mechanism reduction algorithm for the use of developed surrogates in reacting CFD simulation.

Chapter 5 demonstrated how the CFD simulation framework with comprehensive surrogates and its chemical mechanism can be utilized to improve fundamental understanding on the ignition phenomena of reacting spray. In Chapter 5, a numerical

experiment was conducted with CFD simulations using the developed surrogates to evaluate the relative importance of physical and chemical properties of the ignition process of the fuel spray for two fuels, Jet-A and S-8. Either the physical properties or the oxidation chemistry of the baseline Jet-A surrogate was replaced with those of S-8 to quantify the deviations in ignition delay time resulting from physical and chemical property variations. Based upon these results, it can be concluded that the fuel's chemical properties are much more important to the duration of the ignition delay period than the physical properties. It was also found that the effects of both physical properties and oxidation chemistry diminished as the ambient charge temperatures increase. Such a finding implies that the negative effects of variations in CN and physical properties expected from alternative jet fuels can be minimized if the engine is controlled to have higher charge temperature at the time of injection.

6.2 Recommendations for Future Work

6.2.1 Surrogate Development

Due to the maturity of the chemical mechanism and available experimental data, this work used toluene as the aromatic representative surrogate component. However, regarding the actual molecules present in real jet fuels and their mean molecular weight, other single ring aromatic compounds with a longer alkyl chain (such as n-propyl- or n-butyl-benzene) or multiple methyl groups (such as 1,2,4- or 1,3,5- trimethylbenzene) will better represent aromatics in real jet fuels. As recent kinetic studies focus on developing reliable kinetic mechanisms for aromatic compounds larger than toluene, the surrogate

palette can be refined with these aromatic species in the future. Significant improvements in MW and distillation curve emulation are expected with such a modification.

There is a need for a highly branched linear alkane molecule as a surrogate component other than currently available species such as iso-octane (C8) and iso-cetane (C16). Based upon the hydrocarbon size distributions within conventional and alternative jet fuels, the ideal molecular size for the new highly branched linear alkane is ~ C12. Any progress in experimental characterization and kinetic modeling of such a molecule will benefit future surrogates for conventional and alternative jet fuels.

In addition, further experimental validation of the proposed surrogates is necessary. While the DCNs of the surrogates were closely matched to those of the target jet fuels under the nominal IQT operating condition, the surrogates' ignition delay characteristics at different temperature, pressure, and equivalence ratio conditions are not guaranteed to match the target fuels. Thus, in addition to currently on-going experimental validation studies by companion projects (optical diesel engine at Wayne State University, the CFR engine and CID at University of Michigan), more fundamental experiments using shock tubes or rapid compression machines will be beneficial for future analysis.

6.2.2 Thermodynamic Regime for Spray Ignition Process

It is often said that the thermodynamic regime for spray/diesel ignition process is intermediate/low temperature, fuel rich, and high pressure. Identifying this regime is important for determining future directions for generating experimental ignition data, which is critical for the development of future chemical kinetic schemes. When the time evolution of the local conditions calculated by the CFD simulation are investigated

throughout the spray ignition delay period, general insights on relevant thermodynamic regime can be provided as discussed with Figure 5.15 in Chapter 5. Understanding on the thermodynamic regime responsible for diesel spray ignition can be further improved if the time history of thermodynamic conditions for the igniting fuel mass can be estimated with Lagrangian-type tracking. For such a study, the use of turbulence models that better resolve the turbulent flow structure than current RANS simulation may be necessary such as Large Eddy Simulations (LES) or Direct Numerical Simulation (DNS).

Bibliography

[1] U.S. Department of Defense. Directive 4140.25 - DoD Management Policy for Energy Commodities and Related Services. 2004.

[2] Edwards T. Liquid Fuels and Propellants for Aerospace Propulsion: 1903-2003. J Propuls Power 2003;19:1089–107. doi:10.2514/2.6946.

[3] Muzzell PA, Sattler ER, Terry A, McKay BJ, Freerks RL, Stavinoha LL. Properties of Fischer-Tropsch (FT) Blends for Use in Military Equipment. SAE 2006-01-0702 2006.

[4] Blakey S, Rye L, Wilson CW. Aviation gas turbine alternative fuels: A review. Proc Combust Inst 2011;33:2863–85. doi:10.1016/j.proci.2010.09.011.

[5] Kim D, Martz JB, Violi A. Effects of fuel physical properties on direct injection spray and ignition behavior. Submitted to Fuel 2015.

[6] Muzzell PA, Sattler ER, Terry A, McKay BJ, Freerks RL, Stavinoha LL. Properties of Fischer-Tropsch (FT) Blends for Use in Military Equipment. Warrendale, PA: SAE International; 2006.

[7] Zhu Y, Li S, Davidson DF, Hanson RK. Ignition delay times of conventional and alternative fuels behind reflected shock waves. Proc Combust Inst 2015;35:241–8. doi:10.1016/j.proci.2014.05.034.

[8] Schihl P, Hoogterp-Decker L, Gingrich E. The Ignition Behavior of a Coal to Liquid Fischer-Tropsch Jet Fuel in a Military Relevant Single Cylinder Diesel Engine. SAE Int J Fuels Lubr 2012;5:785–802. doi:10.4271/2012-01-1197.

[9] Yost DM, Montalvo DA, Frame EA. U.S. Army Investigation of Diesel Exhaust Emissions Using JP-8 Fuels with Varying Sulfur Content. SAE 961981 1996.

[10] Korres DM, Lois E, Karonis D. Use of JP-8 Aviation Fuel and Biodiesel on a Diesel Engine. SAE 2004-01-3033 2004.

[11] Papagiannakis RG, Kotsiopoulos PN, Hountalas DT, Yfantis E. Single Fuel Research Program Comparative Results of the Use of JP-8 Aviation Fuel versus Diesel Fuel on a Direct Injection and Indirect Injection Diesel Engine. SAE 2006-01-1673 2006.

[12] Kotsiopoulos P, Papagiannakis R, Tsakalou P, Gazinou I, Yfantis E. Experimental Investigation Concerning the Effect of the use of Biodiesel and F-34 (JP-8) Aviation Fuel on Performance and Emissions of a DI Diesel Engine. SAE 2007-01-1450 2007.

[13] Fernandes G, Fuschetto J, Filipi Z, Assanis D, McKee H. Impact of military JP-8 fuel on heavy-duty diesel engine performance and emissions. Proc Inst Mech Eng Part J Automob Eng 2007;221:957–70. doi:10.1243/09544070JAUTO211.
[14] Salvi AA, Assanis D, Filipi Z. Impact of Physical and Chemical Properties of Alternative Fuels on Combustion, Gaseous Emissions, and Particulate Matter during Steady and Transient Engine Operation. Energy Fuels 2012;26:4231–41. doi:10.1021/ef300531r.
[15] Murphy L, Rothamer D. Effects of Cetane Number on Jet Fuel Combustion in a Heavy-Duty Compression Ignition Engine at High Load. SAE 2011-01-0335 2011.
[16] Rothamer DA, Murphy L. Systematic study of ignition delay for jet fuels and diesel fuel in a heavy-duty diesel engine. Proc Combust Inst 2013;34:3021–9. doi:10.1016/j.proci.2012.06.085.
[17] Schihl P, Hoogterp-Decker L. On the Ignition Behavior of JP-8 in Military Relevant Diesel Engines. SAE 2011-01-0119 2011.
[18] Nargunde J, Jayakumar C, Sinha A, Acharya K, Bryzik W, Henein N. Comparison between Combustion, Performance and Emission Characteristics of JP-8 and Ultra Low Sulfur Diesel Fuel in a Single Cylinder Diesel Engine. SAE 2010-01-1123 2010.
[19] Lee J, Bae C. Application of JP-8 in a heavy duty diesel engine. Fuel 2011;90:1762–70. doi:10.1016/j.fuel.2011.01.032.
[20] Handbook of Aviation Fuel Properties - 2004 Third Edition. Air Force Research Laboratory; 2004.
[21] Dagaut P, Cathonnet M. The ignition, oxidation, and combustion of kerosene: A review of experimental and kinetic modeling. Prog Energy Combust Sci 2006;32:48–92. doi:10.1016/j.pecs.2005.10.003.
[22] Farrell JT, Cernansky NP, Dryer FL, Law CK, Friend DG, Hergart CA, et al. Development of an Experimental Database and Kinetic Models for Surrogate Diesel Fuels. SAE 2007-01-0201 2007.
[23] Pitz WJ, Cernansky NP, Dryer FL, Egolfopoulos FN, Farrell JT, Friend DG, et al. Development of an Experimental Database and Chemical Kinetic Models for Surrogate Gasoline Fuels. SAE 2007-01-0175 2007.
[24] Colket M, Edwards T, Williams S, Cernansky NP, Miller DL, Egolfopoulos F, et al. Development of an Experimental Database and Kinetic Models for Surrogate Jet Fuels. AIAA 2007-770 2007.
[25] Pitz WJ, Mueller CJ. Recent progress in the development of diesel surrogate fuels. Prog Energy Combust Sci 2011;37:330–50. doi:10.1016/j.pecs.2010.06.004.
[26] Dryer FL. Chemical kinetic and combustion characteristics of transportation fuels. Proc Combust Inst 2015;35:117–44. doi:10.1016/j.proci.2014.09.008.
[27] Kim D, Martz J, Violi A. A surrogate for emulating the physical and chemical properties of conventional jet fuel. Combust Flame 2014;161:1489–98. doi:10.1016/j.combustflame.2013.12.015.
[28] Dooley S, Won SH, Chaos M, Heyne J, Ju Y, Dryer FL, et al. A jet fuel surrogate formulated by real fuel properties. Combust Flame 2010;157:2333–9. doi:10.1016/j.combustflame.2010.07.001.
[29] Dooley S, Won SH, Heyne J, Farouk TI, Ju Y, Dryer FL, et al. The experimental evaluation of a methodology for surrogate fuel formulation to emulate gas phase

combustion kinetic phenomena. Combust Flame 2012;159:1444–66. doi:10.1016/j.combustflame.2011.11.002.
[30] Huber ML, Lemmon EW, Bruno TJ. Surrogate Mixture Models for the Thermophysical Properties of Aviation Fuel Jet-A. Energy Fuels 2010;24:3565–71. doi:10.1021/ef100208c.
[31] Naik CV, Puduppakkam KV, Modak A, Meeks E, Wang YL, Feng Q, et al. Detailed chemical kinetic mechanism for surrogates of alternative jet fuels. Combust Flame 2011;158:434–45. doi:10.1016/j.combustflame.2010.09.016.
[32] Heywood JB. Internal Combustion Engine Fundamentals. New York: McGraw-Hill; 1988.
[33] Dec JE. A Conceptual Model of DI Diesel Combustion Based on Laser-Sheet Imaging*. SAE 970873 1997. doi:10.4271/970873.
[34] Yanowitz J, Ratcliff MA, McCormick RL, Taylor JD, Murphy MJ. Compendium of Experimental Cetane Numbers. National Renewable Energy Laboratory; 2014.
[35] Wood CP, McDonell VG, Smith RA, Samuelsen GS. Development and application of a surrogate distillate fuel. J Propuls Power 1989;5:399–405. doi:10.2514/3.23168.
[36] Guéret C, Cathonnet M, Boettner J-C, Gaillard F. Experimental study and modeling of kerosene oxidation in a jet-stirred flow reactor. Symp Int Combust 1991;23:211–6. doi:10.1016/S0082-0784(06)80261-4.
[37] Patterson PM, Kyne AG, Pourkashanian M, Williams A, Wilson CW. Combustion of Kerosene in Counterflow Diffusion Flames. J Propuls Power 2001;17:453–60. doi:10.2514/2.5764.
[38] Dagaut P, El Bakali A, Ristori A. The combustion of kerosene: Experimental results and kinetic modelling using 1- to 3-component surrogate model fuels. Fuel 2006;85:944–56. doi:10.1016/j.fuel.2005.10.008.
[39] Violi A, Yan S, Eddings EG, Sarofim AF, Granata S, Faravelli T, et al. Experimental formulation and kinetic model for JP-8 surrogate mixtures. Combust Sci Technol 2002;174:399–417. doi:10.1080/00102200215080.
[40] Vasu SS, Davidson DF, Hanson RK. Jet fuel ignition delay times: Shock tube experiments over wide conditions and surrogate model predictions. Combust Flame 2008;152:125–43. doi:10.1016/j.combustflame.2007.06.019.
[41] Ranzi E, Dente M, Goldaniga A, Bozzano G, Faravelli T. Lumping procedures in detailed kinetic modeling of gasification, pyrolysis, partial oxidation and combustion of hydrocarbon mixtures. Prog Energy Combust Sci 2001;27:99–139. doi:10.1016/S0360-1285(00)00013-7.
[42] Honnet S, Seshadri K, Niemann U, Peters N. A surrogate fuel for kerosene. Proc Combust Inst 2009;32:485–92. doi:10.1016/j.proci.2008.06.218.
[43] Malewicki T, Gudiyella S, Brezinsky K. Experimental and modeling study on the oxidation of Jet A and the n-dodecane/iso-octane/n-propylbenzene/1,3,5-trimethylbenzene surrogate fuel. Combust Flame 2013;160:17–30. doi:10.1016/j.combustflame.2012.09.013.
[44] Mzé-Ahmed A, Hadj-Ali K, Diévart P, Dagaut P. Kinetics of Oxidation of a Synthetic Jet Fuel in a Jet-Stirred Reactor: Experimental and Modeling Study. Energy Fuels 2010;24:4904–11. doi:10.1021/ef100751q.
[45] Dooley S, Won SH, Jahangirian S, Ju Y, Dryer FL, Wang H, et al. The combustion kinetics of a synthetic paraffinic jet aviation fuel and a fundamentally formulated,

experimentally validated surrogate fuel. Combust Flame 2012;159:3014–20. doi:10.1016/j.combustflame.2012.04.010.
[46] Allen C, Valco D, Toulson E, Edwards T, Lee T. Ignition behavior and surrogate modeling of JP-8 and of camelina and tallow hydrotreated renewable jet fuels at low temperatures. Combust Flame 2013;160:232–9. doi:10.1016/j.combustflame.2012.10.008.
[47] Huber ML, Smith BL, Ott LS, Bruno TJ. Surrogate Mixture Model for the Thermophysical Properties of Synthetic Aviation Fuel S-8: Explicit Application of the Advanced Distillation Curve. Energy Fuels 2008;22:1104–14. doi:10.1021/ef700562c.
[48] Huber ML, Lemmon EW, Diky V, Smith BL, Bruno TJ. Chemically Authentic Surrogate Mixture Model for the Thermophysical Properties of a Coal-Derived Liquid Fuel. Energy Fuels 2008;22:3249–57. doi:10.1021/ef800314b.
[49] Stiesch G. Modeling engine spray and combustion processes. Berlin ; New York: Springer; 2003.
[50] Naber J, Siebers DL. Effects of Gas Density and Vaporization on Penetration and Dispersion of Diesel Sprays. SAE 960034 1996.
[51] Siebers DL. Liquid-Phase Fuel Penetration in Diesel Sprays. SAE 980809 1998.
[52] Siebers DL. Scaling Liquid-Phase Fuel Penetration in Diesel Sprays Based on Mixing-Limited Vaporization. SAE 1999-01-0528 1999.
[53] Higgins BS, Mueller CJ, Siebers DL. Measurements of Fuel Effects on Liquid-Phase Penetration in DI Sprays. SAE 1999-01-0519 1999.
[54] Genzale CL, Pickett LM, Kook S. Liquid Penetration of Diesel and Biodiesel Sprays at Late-Cycle Post-Injection Conditions. SAE 2010-01-0610 2010.
[55] Kook S, Pickett LM. Liquid length and vapor penetration of conventional, Fischer–Tropsch, coal-derived, and surrogate fuel sprays at high-temperature and high-pressure ambient conditions. Fuel 2012;93:539–48. doi:10.1016/j.fuel.2011.10.004.
[56] Wu Z, Zhu Z, Huang Z. An experimental study on the spray structure of oxygenated fuel using laser-based visualization and particle image velocimetry. Fuel 2006;85:1458–64. doi:10.1016/j.fuel.2005.12.024.
[57] Arcoumanis C, Bae C, Crookes R, Kinoshita E. The potential of di-methyl ether (DME) as an alternative fuel for compression-ignition engines: A review. Fuel 2008;87:1014–30. doi:10.1016/j.fuel.2007.06.007.
[58] Basha SA, Gopal KR, Jebaraj S. A review on biodiesel production, combustion, emissions and performance. Renew Sustain Energy Rev 2009;13:1628–34. doi:10.1016/j.rser.2008.09.031.
[59] Yu J, Bae C. Dimethyl ether (DME) spray characteristics in a common-rail fuel injection system. J Automob Eng 2003;217:1135–44. doi:10.1243/09544070360729473.
[60] Kim HJ, Park SH, Lee CS. A study on the macroscopic spray behavior and atomization characteristics of biodiesel and dimethyl ether sprays under increased ambient pressure. Fuel Process Technol 2010;91:354–63. doi:10.1016/j.fuproc.2009.11.007.
[61] Som S, Longman DE, Ramírez AI, Aggarwal SK. A comparison of injector flow and spray characteristics of biodiesel with petrodiesel. Fuel 2010;89:4014–24. doi:10.1016/j.fuel.2010.05.004.

[62] Pei Y, Shan R, Som S, Lu T, Longman D, Davis MJ. Global Sensitivity Analysis of a Diesel Engine Simulation with Multi-Target Functions. SAE 2014-01-1117 2014.
[63] Ra Y, Reitz RD, McFarlane J, Daw CS. Effects of Fuel Physical Properties on Diesel Engine Combustion using Diesel and Bio-diesel Fuels. SAE 2008-01-1379 2008.
[64] Richards KJ, Senecal PK, Pomraning E. CONVERGE (Version 2.1.0). Middleton, WI: Convergent Science Inc.; 2013.
[65] Reitz RD, Diwakar R. Structure of High-Pressure Fuel Sprays. SAE 870598 1987. doi:10.4271/870598.
[66] Schmidt DP, Rutland CJ. A New Droplet Collision Algorithm. J Comput Phys 2000;164:62–80. doi:10.1006/jcph.2000.6568.
[67] Post SL, Abraham J. Modeling the outcome of drop–drop collisions in Diesel sprays. Int J Multiph Flow 2002;28:997–1019. doi:10.1016/S0301-9322(02)00007-1.
[68] Liu AB, Mather D, Reitz RD. Modeling the Effects of Drop Drag and Breakup on Fuel Sprays. SAE 930072 1993.
[69] Amsden AA, O'Rourke PJ, Butler TD. KIVA-II: A Computer Program for Chemically Reactive Flows with Sprays. Los Alamos National Laboratory; 1989.
[70] Senecal PK, Pomraning E, Richards KJ, Som S. Grid-convergent spray models for internal combustion engine cfd simulation. ICEF2012-92043 2012.
[71] Design Institute for Physical Properties, Sponsored by AIChE. DIPPR Project 801 - Full Version. Design Institute for Physical Property Research/AIChE; 2012.
[72] Narayanaswamy K, Pepiot P, Pitsch H. A chemical mechanism for low to high temperature oxidation of n-dodecane as a component of transportation fuel surrogates. Combust Flame 2014;161:866–84. doi:10.1016/j.combustflame.2013.10.012.
[73] Sandia National Laboratories. Engine Combustion Network. Engine Combust Netw n.d. http://www.sandia.gov/ecn/index.php.
[74] Pickett LM, Manin J, Genzale CL, Siebers DL, Musculus MPB, Idicheria CA. Relationship Between Diesel Fuel Spray Vapor Penetration/Dispersion and Local Fuel Mixture Fraction. SAE 2011-04-12 2011.
[75] Lillo PM, Pickett LM, Persson H, Andersson O, Kook S. Diesel Spray Ignition Detection and Spatial/Temporal Correction. SAE 2012-01-1239 2012.
[76] Wilkinson PM, Van Schayk A, Spronken JPM, Van Dierendonck L.-. The influence of gas density and liquid properties on bubble breakup. Chem Eng Sci 1993;48:1213–26. doi:10.1016/0009-2509(93)81003-E.
[77] Ejim CE, Fleck BA, Amirfazli A. Analytical study for atomization of biodiesels and their blends in a typical injector: Surface tension and viscosity effects. Fuel 2007;86:1534–44. doi:10.1016/j.fuel.2006.11.006.
[78] Som S, Aggarwal SK. Effects of primary breakup modeling on spray and combustion characteristics of compression ignition engines. Combust Flame 2010;157:1179–93. doi:10.1016/j.combustflame.2010.02.018.
[79] Kodavasal J, Lavoie GA, Assanis DN, Martz JB. The effects of thermal and compositional stratification on the ignition and duration of homogeneous charge compression ignition combustion. Combust Flame 2015;162:451–61. doi:10.1016/j.combustflame.2014.07.026.

[80] Abramovich GN, Schindel L, IEEE Xplore (Online service). The theory of turbulent jets., Cambridge, Massachusetts, MIT Press, 2003.
[81] Moses CA. Comparative Evaluation of Semi-Synthetic Jet Fuels. Coordinating Research Council; 2008.
[82] Shafer LM, Striebich RC, Gomach J, Edwards T. Chemical class composition of commercial jet fuels and other specialty kerosene fuels. AIAA 2006-7972 2006.
[83] Bruno TJ, Baibourine E, Lovestead TM. Comparison of Synthetic Isoparaffinic Kerosene Turbine Fuels with the Composition-Explicit Distillation Curve Method. Energy Fuels 2010;24:3049–59. doi:10.1021/ef100067q.
[84] Grunberg L, Nissan AH. Mixture Law for Viscosity. Nature 1949;164:799–800.
[85] Poling BE, Thomson GH, Friend DG, Rowley RL, Wilding WV. Physical and Chemical Data. Perrys Chem. Eng. Handb. 8th Edition, 2007.
[86] Hugill JA, Van Welsenes AJ. Surface tension: a simple correlation for natural gas + conensate systems. Fluid Phase Equilibria 1986;29:383–90. doi:10.1016/0378-3812(86)85038-5.
[87] Perez PL, Boehman AL. Experimental Investigation of the Autoignition Behavior of Surrogate Gasoline Fuels in a Constant-Volume Combustion Bomb Apparatus and Its Relevance to HCCI Combustion. Energy Fuels 2012;26:6106–17. doi:10.1021/ef300503b.
[88] Scheffé H. Experiments With Mixtures. J R Stat Soc Ser B Methodol 1958;20:344–60.
[89] ASTM D6890. ASTM International, West Conshohocken, PA; n.d.
[90] Bruno TJ. Improvements in the Measurement of Distillation Curves. 1. A Composition-Explicit Approach†. Ind Eng Chem Res 2006;45:4371–80. doi:10.1021/ie051393j.
[91] Bruno TJ, Smith BL. Evaluation of the Physicochemical Authenticity of Aviation Kerosene Surrogate Mixtures. Part 1: Analysis of Volatility with the Advanced Distillation Curve. Energy Fuels 2010;24:4266–76. doi:10.1021/ef100496j.
[92] Bogin GE, DeFilippo A, Chen JY, Chin G, Luecke J, Ratcliff MA, et al. Numerical and Experimental Investigation of n-Heptane Autoignition in the Ignition Quality Tester (IQT). Energy Fuels 2011;25:5562–72. doi:10.1021/ef201079g.
[93] Murphy MJ, Taylor JD, McCormick RL. Compendium of Experimental Cetane Number Data. National Renewable Energy Laboratory; 2004.
[94] Santana RC, Do PT, Santikunaporn M, Alvarez WE, Taylor JD, Sughrue EL, et al. Evaluation of different reaction strategies for the improvement of cetane number in diesel fuels. Fuel 2006;85:643–56. doi:10.1016/j.fuel.2005.08.028.
[95] Heyne JS, Boehman AL, Kirby S. Autoignition studies of trans-and cis-decalin in an ignition quality tester (IQT) and the development of a high thermal stability unifuel/single battlefield fuel. Energy Fuels 2009;23:5879–85.
[96] Kim D, Martz J, Abdul-Nour A, Yu X, Jansons M, Violi A. An inclusive six-component surrogate for emulating the physical and chemical characteristics of conventional and alternative jet fuels and their blends. Submitted to 36th Int Symp Combust 2015.
[97] Bessee GB, Hutzler SA, Wilson GR. Analysis of Synthetic Aviation Fuels. Air Force Research Laboratory; 2011.

[98] Bruno TJ, Huber ML, Laesecke A, Lemmon EW, McLinden M, Outcalt SL, et al. Thermodynamic, Transport, and Chemical Properties of “Reference” JP-8. National Institute of Standards and Technology; 2010.
[99] Bruno TJ, Smith BL. Improvements in the Measurement of Distillation Curves. 2. Application to Aerospace/Aviation Fuels RP-1 and S-8†. Ind Eng Chem Res 2006;45:4381–8. doi:10.1021/ie051394b.
[100] Smith BL, Bruno TJ. Improvements in the Measurement of Distillation Curves. 4. Application to the Aviation Turbine Fuel Jet-A. Ind Eng Chem Res 2007;46:310–20. doi:10.1021/ie060938m.
[101] Hui X, Kumar K, Sung C-J, Edwards T, Gardner D. Experimental studies on the combustion characteristics of alternative jet fuels. Fuel 2012;98:176–82. doi:10.1016/j.fuel.2012.03.040.
[102] Outcalt S, Laesecke A, Freund MB. Density and Speed of Sound Measurements of Jet A and S-8 Aviation Turbine Fuels†. Energy Fuels 2009;23:1626–33. doi:10.1021/ef800888q.
[103] Bruno TJ, Huber ML, Laesecke A, Lemmon EW, Outcalt SL, Perkins R, et al. The Properties of S-8. NIST; 2006.
[104] CHEMKIN 10112. San Diego: Reaction Design; 2011.
[105] Model Fuels Consortium. Reaction Design; 2012.
[106] Curran HJ, Gaffuri P, Pitz WJ, Westbrook CK. A comprehensive modeling study of iso-octane oxidation. Combust Flame 2002;129:253–80. doi:10.1016/S0010-2180(01)00373-X.
[107] Wang H, Oehlschlaeger MA. Autoignition studies of conventional and Fischer–Tropsch jet fuels. Fuel 2012;98:249–58. doi:10.1016/j.fuel.2012.03.041.
[108] Shen H-PS, Steinberg J, Vanderover J, Oehlschlaeger MA. A Shock Tube Study of the Ignition of n-Heptane, n-Decane, n-Dodecane, and n-Tetradecane at Elevated Pressures. Energy Fuels 2009;23:2482–9. doi:10.1021/ef8011036.
[109] Oehlschlaeger MA, Steinberg J, Westbrook CK, Pitz WJ. The autoignition of iso-cetane at high to moderate temperatures and elevated pressures: Shock tube experiments and kinetic modeling. Combust Flame 2009;156:2165–72. doi:10.1016/j.combustflame.2009.05.007.
[110] Zhu Y, Davidson DF, Hanson RK. Pyrolysis and oxidation of decalin at elevated pressures: A shock-tube study. Combust Flame 2014;161:371–83. doi:10.1016/j.combustflame.2013.09.005.
[111] Shen H-PS, Vanderover J, Oehlschlaeger MA. A shock tube study of the auto-ignition of toluene/air mixtures at high pressures. Proc Combust Inst 2009;32:165–72. doi:10.1016/j.proci.2008.05.004.
[112] Niemeyer KE, Sung C-J, Raju MP. Skeletal mechanism generation for surrogate fuels using directed relation graph with error propagation and sensitivity analysis. Combust Flame 2010;157:1760–70. doi:10.1016/j.combustflame.2009.12.022.
[113] Raju M, Wang M, Senecal PK, Som S, Longman DE. A Reduced Diesel Surrogate Mechanism for Compression Ignition Engine Applications. ICEF2012-92045 2012:711–22. doi:10.1115/ICEF2012-92045.
[114] Lu T, Law CK. A directed relation graph method for mechanism reduction. Proc Combust Inst 2005;30:1333–41. doi:10.1016/j.proci.2004.08.145.

[115] Lu T, Law CK. On the applicability of directed relation graphs to the reduction of reaction mechanisms. Combust Flame 2006;146:472–83. doi:10.1016/j.combustflame.2006.04.017.
[116] Lu T, Law CK. Strategies for mechanism reduction for large hydrocarbons: n-heptane. Combust Flame 2008;154:153–63. doi:10.1016/j.combustflame.2007.11.013.
[117] Pepiot-Desjardins P, Pitsch H. An efficient error-propagation-based reduction method for large chemical kinetic mechanisms. Combust Flame 2008;154:67–81. doi:10.1016/j.combustflame.2007.10.020.
[118] Westbrook CK, Pitz WJ, Herbinet O, Curran HJ, Silke EJ. A comprehensive detailed chemical kinetic reaction mechanism for combustion of n-alkane hydrocarbons from n-octane to n-hexadecane. Combust Flame 2009;156:181–99. doi:10.1016/j.combustflame.2008.07.014.
[119] Ryan TW. Correlation of Physical and Chemical Ignition Delay to Cetane Number. SAE 852103 1985.
[120] Zheng Z, Badawy T, Henein N, Sattler E. Investigation of Physical and Chemical Delay Periods of Different Fuels in the Ignition Quality Tester. J Eng Gas Turbines Power 2013;135:061501–061501. doi:10.1115/1.4023607.
[121] Mayo MP, Boehman AL. Ignition Behavior of Biodiesel and Diesel under Reduced Oxygen Atmospheres. Energy Fuels 2015;29:6793–803. doi:10.1021/acs.energyfuels.5b01439.
[122] Heyne JS, Boehman AL, Kirby S. Autoignition Studies of trans- and cis-Decalin in an Ignition Quality Tester (IQT) and the Development of a High Thermal Stability Unifuel/Single Battlefield Fuel. Energy Fuels 2009;23:5879–85. doi:10.1021/ef900715m.
[123] Haas FM, Ramcharan A, Dryer FL. Relative reactivities of the isomeric butanols and ethanol in an ignition quality tester. Energy Fuels 2011;25:3909–16.
[124] Richards KJ, Senecal PK, Pomraning E. CONVERGE (v2.2.0). Madison, WI: Convergent Science Inc.; 2014.
[125] Kook S, Pickett LM. Soot Volume Fraction and Morphology of Conventional, Fischer-Tropsch, Coal-Derived, and Surrogate Fuel at Diesel Conditions. SAE Int J Fuels Lubr 2012;5:647–64. doi:10.4271/2012-01-0678.
[126] Pickett LM, Hoogterp L. Fundamental Spray and Combustion Measurements of JP-8 at Diesel Conditions. SAE 2008-01-1083 2008.
[127] Vasu SS, Davidson DF, Hong Z, Vasudevan V, Hanson RK. n-Dodecane oxidation at high-pressures: Measurements of ignition delay times and OH concentration time-histories. Proc Combust Inst 2009;32:173–80. doi:10.1016/j.proci.2008.05.006.